Efficient Models for the Evaluation and Estimation of the Gravity Field

by

Brandon A. Jones

B.S., Mathematics, The University of Texas at Austin, 2000

B.A., Physics, The University of Texas at Austin, 2000

M.S., Aerospace Engineering Sciences, University of Colorado at Boulder,

2006

A thesis submitted to the

Faculty of the Graduate School of the

University of Colorado in partial fulfillment

of the requirements for the degree of

Doctor of Philosophy

Department of Aerospace Engineering Sciences

2010

This thesis entitled:
Efficient Models for the Evaluation and Estimation of the Gravity Field
written by Brandon A. Jones
has been approved for the Department of Aerospace Engineering Sciences

_____

George H. Born

_____

Gregory Beylkin

Date _____

The final copy of this thesis has been examined by the signatories, and we find that both the
content and the form meet acceptable presentation standards of scholarly work in the above
mentioned discipline.

Jones, Brandon A. (Ph.D., Aerospace Engineering Sciences)

Efficient Models for the Evaluation and Estimation of the Gravity Field

Thesis directed by Prof. George H. Born

Current astrodynamics applications require a rapid evaluation of the gravity field and an efficient approach to gravity estimation. The commonly used spherical harmonic model does not meet either of these needs. To address these issues, this research considers two new gravity representations: the cubed-sphere and the MRQSphere models. Offering a means for rapid evaluation, the cubed-sphere model yields an effectively constant computation time for any degree of the modeled gravity field. Analyzing the model's performance in a series of Monte-Carlo-like tests characterizes its effects on both orbit propagation and determination. When compared to the spherical harmonic gravity model, the cubed-sphere model improves computational efficiency without causing any significant deviation in resulting trajectories. Using this new model in sequential orbit determination improves the computational efficiency of the time update. As a result, the measurement update now dominates the filter execution time for near real-time applications. Since cubed-sphere models of higher degree require only a slight change in computation time, orbit propagation and determination systems may now use this model to improve fidelity without any significant change in cost. To address the gravity estimation problem, combining a new multiresolution technique with nearly optimal quadratures (for the sphere) invariant under the icosahedral group defines the MRQSphere model. This new multiresolution representation allows for gravity estimation via a naturally staged approach to a celestial body with an unknown gravity field, which aids in the design of missions to small bodies. To test the new model's capabilities, this research simulates a mission to an asteroid. Tests include the characterization of a MRQSphere model derived from the asteroid's spherical harmonic model, and the estimation of a model via observations of the gravity potential. For such a simplified scenario, the results indicate that the MRQSphere model meets the estimation accuracy requirements; future work is recommended to fully explore its capabilities.

Dedication

For Celia, my brother Noel, and my mother Marian.

I especially dedicate this to my father, Allan. You provided me with the opportunities to explore my passions. After undergrad, when I was tempted by the higher wages of the computer industry, you reminded me of what I wanted to do since I was a kid. I would not have completed this without the help and guidance you offered throughout the years. Words cannot express my thanks.

Acknowledgements

First, I would like to thank the members of my dissertation committee for generously providing guidance and direction throughout this research. First, I thank my principle research advisor, Dr. George H. Born, for his support and advice. I would also like to thank Dr. Gregory Beylkin for creating the gravity models characterized in this research, and for helping me to fully understand the mathematics required. Finally, I thank the other members of my committee: Dr. Daniel Scheeres, Dr. Steve Nerem, and Dr. Rodney Anderson. Thank you for all of your help.

Several sources of funding enabled this research. A majority of this work was funded by a NASA Graduate Student Researcher Program (GSRP) fellowship through the Johnson Space Center. As a GSRP summer intern, civil servants and contractors at NASA/JSC provided advice and assistance. I would especially like to thank Tom Manning, Kevin Key, Tim Runkle, Blair Thompson, and, especially, my NASA technical mentor Steve Provence. A portion of this work was also funded by an AIAA Foundation Orville and Wilbur Wright Graduate Award. I would also like to thank the Aerospace Engineering Sciences Department, which graciously provided several teaching assistant positions before I acquired research funding.

This research leverages off of the TurboProp integration package, which was originally developed by Keric Hill. He made this software available to the research group, and even added capabilities that enabled this work. I thank him for providing what became the software workhorse of this research.

Fellow graduate students provided guidance, constructive criticism, answered silly questions, and helped throughout the course of my graduate work. They have been colleagues, friends,

teammates, students, and mentors. I would especially like to thank those that, in some way, provided incite, suggestions, or background information: Jeffrey Parker, David Wiese, Bryant Loomis, Christopher Lane, Ryan Woolley, Jill Tombasco, and Aurore Sibois.

Contents

Chapter

Tables

Table

Figures

Figure

Chapter 1

Introduction

1.1   Motivation

Although it is commonly used for modeling the gravity field, the spherical harmonic model fails to adapt to modern demands. For this reason, there are a variety of new methods for representing the gravity field that allow for faster evaluation, efficient estimation, and improved reliability. These new models come in a variety of forms, from interpolation between discrete points, to representations based on surface integrals over a given body. This research focuses on profiling two of these new models for modern astrodynamics and geodesy applications.

The astrodynamics community now requires efficient and accurate evaluation of the gravity field for rapid orbit propagation. Reasons for these requirements include, but are not limited to: the increasing number of objects tracked by satellite surveillance networks, the need for near real-time precise orbit determination, and increasing fidelity requirements for Monte-Carlo simulations. Increasing the degree (which increases accuracy) of the gravity representation in the spherical harmonic model quadratically increases the computation requirement for evaluating the gravity field. Thus, highly-accurate gravity evaluation with this model requires a reduction in computational efficiency. Although modern computing resources help to mitigate this issue, such improvements fail to match increasing demands. Additionally, hardware based solutions may not yield robust implementations and lack universal portability.

When using satellite-based observations of gravity, current models fail to meet estimation demands. For example, scientists now require localized gravity models to observe temporal vari-

ations in the gravity field in a specific region. However, the spherical harmonic model does not, directly, yield a localized representation. One may derive a local gravity model using the higher-degree terms in the spherical harmonic model, but this becomes increasingly difficult when using measurements gathered at orbit altitudes. Traditionally, geodesists seek improved measurement accuracy to resolve these high-degree terms, but numerical issues start to create problems.

The international space community currently considers asteroid missions a high priority, but the spherical harmonic model is poorly suited for such applications. It is poorly suited to representing the gravity field for aspherical bodies, which includes many asteroids and comets. Additionally, the gravity field is mostly unknown before arrival. Thus, we require a staged approach to the small body before any low-altitude operations or precise landing may occur. The spherical harmonic model provides no such natural approach for the gravity estimation problem.

Developing new gravity representations requires a balance of several factors, including those mentioned briefly above. To achieve such a balance, we study two new models: the cubed-sphere and the MRQSphere model. These models may be converted between one another, allowing for the selection of the proper model for a given application. This research profiles these models for the problems of rapid gravity evaluation and efficient estimation of the gravity field.

1.2   Background

1.2.1   Representing the Gravity Field

Developing a full understanding of gravity has occupied the minds of scientists for almost 500 years. In 1586, Simon Stevin conducted the first falling ball experiments to demonstrate that objects of unequal mass accelerate at the same rate. Galileo Galilei followed these experiments, albeit more scientifically, by using an inclined plane (Galilei, 1638). The next major advance in defining the gravitational field came with Newton's Law of Universal Gravitation (Newton, 1687), which defines the gravitational force exerted by one body on another. Newton's Law of Universal Gravitation is commonly applied to point masses, but still holds for spheres of uniform density

(see, e.g., Laplace, 1798). However, all known planetary bodies deviate from these assumptions.

The next major advance in modeling the gravity field was developed by Pierre-Simon Laplace. Laplace (1798) derived (expressed in notation later developed by Thomson and Tait (1879)) the differential equation

$$\nabla^2 U = 0, \tag{1.1}$$

where U is the gravity potential. Thus, we refer to this equation as Laplace's Equation. Using the Legendre polynomials, Laplace (1798) developed the first solution of this equation with boundary values on the sphere. This early model only included the zero-order terms, i.e. variations in the gravity field invariant with longitude. Thomson and Tait (1879) later generated a solution that includes nonzero order terms via the associated Legendre functions. For astrodynamics applications, we refer to this latter form as the spherical harmonic model of the gravity field.

Einstein's Theory of General Relativity, which generalizes special relativity and Newton's Law of Universal Gravitation, leads to the need of higher order perturbations of the gravity field described by the bending of both space and time by mass (Einstein, 1916). This theory accounts for some inconsistencies between observations and Newtonian gravity, such as the error in the Newtonian estimate of the precession of Mercury's perihelion. In this research, we only consider the Newtonian case.

Gravity representations may be split into the four categories discussed by Tscherning (1986): (1) a series expansion of orthogonal functions, (2) a linear combination of potential functions, (3) linear combinations of functions defined via splines, kernels, or finite elements, and (4) collocation methods using minimum norm or least squares. In this dissertation, we use models of the forms (1)-(3). Representations of the form of (4) prove to most accurately represent local variations in the gravity field, but the model is not optimal for global variations (Tscherning, 1986). Since local variations attenuate with altitude (as implied by Newton's Law of Universal Gravitation for a finite mass), global variations dominate satellite dynamics. Thus, we do not discuss collocation methods in this document. We now turn our attention to the first three representations.

1.2.1.1   Series Expansions of Orthogonal Functions

The spherical harmonic model represents the gravity field as a linear combination of an infinite number of orthogonal functions on the sphere. These functions, often called spherical harmonics, use the associated Legendre functions of the first kind for a given degree and order. The frequency of each function increases with degree, which implies a smaller wavelength. These shorter wavelengths correspond to smaller areas on the sphere. Thus, high-degree models imply increased spatial resolution of the model. Contributions to the gravity field are often described by these terms, i.e. long-wavelength variations correspond to low degree functions, etc. Detailed treatments of this model may be found in Hofmann-Wellenhof and Moritz (2006), Kaula (1966), Montenbruck and Gill (2005), and many others.

As the degree of available gravity models increases, so does the difficulty of accurately evaluating the associated Legendre functions. Most methods utilize recursive formulations (for example Rapp, 1982; Tscherning et al., 1983; Clenshaw, 1955). However, one must be careful to select a numerically stable formulation (see, e.g., Lundberg and Schutz, 1988). Other methods compute the functions in the frequency domain via Fourier transforms (Colombo, 1981; Dilts, 1985). With current models available up to degree 2,160 (Pavlis et al., 2008) and ultra-high degree models in development, research is ongoing. Jekeli et al. (2007) proposed a method that demonstrates stability up to degree 10,800 by isolating stable oscillations based on a desired accuracy.

Use of the spherical harmonic model has extended beyond simple orbit propagation. Semi-analytic theories for time varying orbit elements and relative satellite motion utilize expansions of the spherical harmonic model. For example, sun-synchronous and critically inclined orbits are often formulated in terms of the spherical harmonic model. Hofmann-Wellenhof and Moritz (2006), Seeber (2003), Vallado and McClain (2007), and Kaula (1966) provide details on these semi-analytic orbit propagation techniques. Early methods of satellite geodesy used these theories for gravity field estimation via observed perturbations from the expected elliptical orbits (see, e.g., Heiskanen and Moritz, 1967).

The traditional form of the spherical harmonic model has a singularity at the poles (see, e.g., Pines, 1973). Given finite precision representations of numbers in modern computers, this is actually a small region in the vicinity of the polar axis at which this model becomes undefined. Although the probability of a satellite passing directly over a pole is low, and usually known in advance, this remains a concern for real-time satellite state estimation. Alternate representations of the gravity potential have been proposed, particularly those in Pines (1973) and Gottlieb (1993), which remove the singularity. As reformulations of the classical spherical harmonic model, these alternatives also combine an infinite number of orthogonal functions on the sphere.

Like the spherical harmonic model, the ellipsoidal harmonic model represents one solution to Laplace's equation, albeit with boundary values on the surface of an ellipsoid. Use of this model for astrodynamics applications has increased with recent interest in asteroids, with one such model estimated for 433 Eros (Garmier et al., 2002). Instead of Legendre functions, the ellipsoidal harmonic model uses Lamé functions of the second kind. Full descriptions of the ellipsoidal harmonics may be found in Hobson (1931), Kaula (1966), and Garmier and Barriot (2001).

1.2.1.2 Linear Combination of Potentials

Models using a linear combination of potentials usually assume a collection of point masses, i.e. the sum of individual gravity potentials yields the total potential of a system. However, other forms exist.

Past applications of point-mass models include studies of the lunar gravity field. Muller and Sjogren (1968) identified the presence of mass concentrations, dubbed mascons, in the moon. Based on the locations of these mascons, Gottlieb (1970) estimated a gravity model using subsurface point masses to account for gravity anomalies. Wong et al. (1971) took this process one step further, and considered a collection of subsurface disks, each with uniform density. Both studies found improved orbit determination accuracy when using such models.

Werner and Scheeres (1997) presents a model for evaluating the gravity field of any general polyhedron. An irregularly shaped body, such as an asteroid, may be represented by a polyhedron

to some precision. Formulating the gravity potential as a volume integral of differential masses, the gravity field may be represented by a linear combination of surface integrals on each face and edge of the polyhedron. This model satisfies Laplace's equation at any point outside of the body, with accuracy limited by an assumption of constant density and the accuracy of the shape representation (Werner and Scheeres, 1997). Instead of a single polyhedron, Scheeres et al. (2000) defined the body as a collection of polyhedra, allowing for each polyhedron to have a different, but individually uniform, density. Unfortunately, the polyhedron model is computational intensive (Werner and Scheeres, 1997; Colombi et al., 2008).

Instead of the polyhedron model, some applications reduce computation time by considering an irregularly shaped object as a collection of point masses. Geissler et al. (1996) defined the asteroid 243 Ida by a collection of uniformly distributed point masses to study reaccretion patterns of ejecta from the Azzurra crater. Ashenberg (2005) attempted to simplify the computational burden of the full-body problem using a collection of point masses to represent the primary body. Werner and Scheeres (1997) demonstrates this improved efficiency, unfortunately, comes at the cost of accuracy.

1.2.1.3   Linear Combination of Nodes

Some gravity models define the gravity field, or some derived quantity, as a collection of nodes with interpolation performed between them for evaluation of the gravity field. Typically, these models provide fast evaluation or estimation capabilities.

The earliest (known) gravity model based on a collection of discrete nodes was proposed in Junkins (1976), and further studied in Junkins (1977), Junkins and Saunders (1977) and Engels and Junkins (1980). This model used finite element techniques to represent the gravity field. Based on latitude and longitude, values were stored at discrete points up to an altitude of 1.2 Earth radii, with evaluation between nodes accomplished via interpolating polynomials. With the second degree terms represented using the spherical harmonic model, Junkins (1976) represented terms up to degree 23 using the finite element model. Orbit propagation demonstrated over an order of

magnitude improvement in computation speed with peak errors of 25 m. The authors concluded that their model was not the optimal solution and further research would allow for refinements and accuracy improvements. We are not aware of any published research using this model after Engels and Junkins (1980).

Colombi et al. (2008) established a similar finite element scheme for irregularly shaped primary bodies. In Junkins (1976), the ellipsoidal shape of the Earth allowed for an easy, albeit nonuniform, definition of the finite element mesh. However, irregularly shaped objects, such as asteroids, require a more adaptive grid. Colombi et al. (2008) uses octrees for data storage and rapid recall of the coefficients used for polynomial interpolation. Most orbit propagation errors, when compared to a polyhedron model, were within 4 m with peak errors of 20 m. In Colombi et al. (2009), the authors refine this model to allow variable density nodes, based on gravity variations, and switched to B-spline interpolation. Orbit propagation results were similar to those of the cubetree model.

Beylkin and Cramer (2002) proposed three new models: (1) B-splines defined on the surface of a sphere, (2) polynomials on subdivisions of the surface of the cube, and (3) B-splines on the surface of a cube. The third model is the cubed-sphere model, which combines the benefits of the first two. A major goal in the development of these models was to improve computational efficiency when using geopotential models. Effectively, it is a trade of speed for memory, i.e. file size. Modern computers have more than sufficient memory for this purpose. In (1), defining B-splines on the surface of the sphere maintains the stretching and the resulting oversampling near the poles. In (2), using piecewise polynomials on the face of the cube requires a higher sampling rate than using splines. In (3), using splines on the faces of the cube does not have stretching near the poles associated with the first model, and uses the lower sampling rate associated with splines. Hence, option (3) is more efficient. Beylkin and Cramer (2002) proposed this new cubed-sphere model, but, as of the start of this research, it had not yet been profiled for astrodynamics applications.

As opposed to fast evaluation, similar models were designed for optimizing the gravity estimation problem. For the previous models of this section, values at the nodes are computed using

another base model, i.e. the spherical harmonic model. Meissl (1981) designed and generated the first finite element model for the estimation problem by solving for the gravity field at a collection of nodes when given inhomogenous terrestrial measurements. Results demonstrated that the computational requirement for such an estimation process was superior to other methods at the time. Svensson (1984) independently developed a similar method. More recently, Fašková et al. (2010) extended such a finite element representation to three dimensions to approximate the gravity field above the Earth's surface in a small region. Although not yet defined, the tools presented in Beylkin and Monzón (2010) and Ahrens and Beylkin (2009) combine to generate another discretized model for optimal estimation. We explore this model further in this research.

1.2.2   Towards Efficient Evaluation of the Gravity Field

Demands for gravity model accuracy and computational efficiency are increasing. Satellite missions requiring autonomy must generate a navigation solution in real-time, but onboard computational resources are limited. Missions like COSMIC (Rocken et al., 2000) require reduced orbit determination evaluation times to provide near real-time observations of space and terrestrial weather (Hwang et al., 2008). The Jet Propulsion Laboratory also generates near real-time orbit determination solutions for the Jason-2 satellite (Desai et al., 2010) and the full GPS constellation (Weiss et al., 2010). In the case of Jason-2, the orbit determination system requires a 200×200 model (Bertiger et al., 2010). Some systems observe and generate orbit determination solutions of multiple satellites. The US Air Force maintains a catalog of all known space objects, and propagates the state of each forward in time, along with the state-error covariance matrix, to continue tracking and predict any collisions. In 2004, the Air Force tracked approximately 10,000 space objects (Tirpak, 2004). In just five years, that estimate almost doubled to 19,000 objects (James, 2009). As the catalog continues to expand, so does the the computational burden of these surveillance operations. Thus, such systems require rapid orbit propagation for both catalog estimation and propagation. Gravity models also limit simulation capabilities, especially for real-time and Monte Carlo studies for requirements definition, trade studies, and flight software verification and

validation. Tasks such as these require computationally efficient models of the satellite dynamics.

When using the common spherical harmonic model of the gravity potential, model computation time increases quadratically with degree (Beylkin and Cramer, 2002). In other words, increasing the degree and order of the gravity model by a factor of 10 results in a factor of 100 increase in operations required for evaluation. Thus, increasing the fidelity of models used in orbit propagation requires a considerable increase in computation time. Figure 1.1 illustrates this quadratic increase.
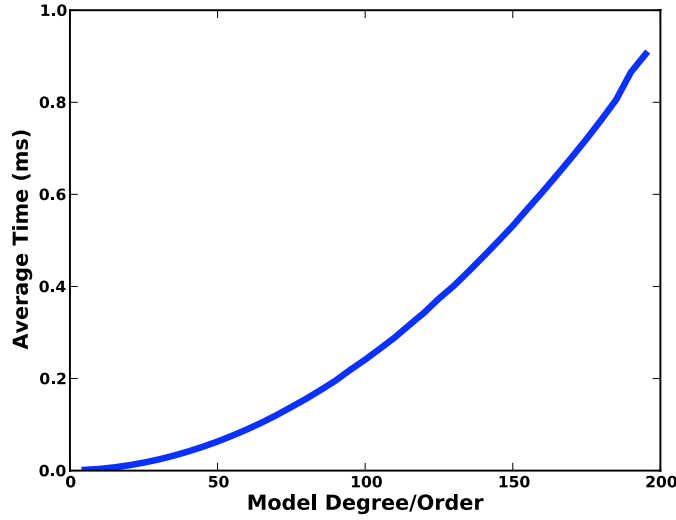
Figure 1.1: Average execution time (over 10,000 evaluations) for the spherical harmonic model of a given degree and order.

The spherical harmonic model may be made faster through a careful implementation. The most common approach reduces the number of operations required to compute the associated Legendre functions (Bettadpur et al., 1992; Gottlieb, 1993). Another approach seeks to reduce the model to the subset of orthonormal functions that dominate the solution (Hujsak, 1996). Other techniques demonstrate improved speed by reformulating the model entirely.

In the early days of gravity model development, available memory partially limited computing capabilities. This led to the development of gravity estimation and modeling techniques that

minimize memory requirements (see, e.g., Deprit, 1979). Since modern computers have memory limitations on the order of gigabytes, this is no longer a concern. For this reason, new methods for improving the efficiency of gravity field evaluation use these changes in modern computers to swap computation time for larger memory requirements.

Junkins (1976) first identified the need for fast evaluation of the gravity field, which motivated the development of the previously described finite elements model. This reformulation of the gravity field yielded an order of magnitude reduction in computation time (Junkins, 1976), but the model went largely unused. Ryan Russell of the Georgia Tech Institute of Technology recently began using this model for space situational awareness (SSA) applications.[1] However, that work has yet to be published.

Gravity acceleration approximation functions (GAAF) also reduce the computational burden of evaluation (Hujsak, 1996). Using a pseudocenter unique to the point of evaluation, the two-body equation is evaluated. Least squares techniques are used to determine these pseudocenters at node points based on a given gravity model and a required accuracy. Interpolation is then used to evaluate the gravity field at points between nodes. Results demonstrate a GAAF model equivalent to a 70×70 spherical harmonic model requires the same computation time as a 5×5 model. However, the GAAF models tested in Hujsak (1996) were optimized for efficient evaluation at the expense of precision with the spherical harmonic model from which it was derived.

1.2.3 Towards Efficient Estimation of the Gravity Field

1.2.3.1 Earth-Based Estimation

Estimation of the gravity field began with pendulum experiments conducted at or near the Earth's surface during the time of Newton. Inconsistencies between these measurements identified the nonuniformity of the gravity field over the Earth's surface. Heiskanen (1938) provided the first estimate of the second-degree zonal and tesseral harmonics using such terrestrial observations. The launch of Sputnik signaled the start of satellite geodesy, with the tracking of the Vanguard mission

---

[1] http://www.dodsbir.net/selections/sttr1_09B.htm

yielding the first measurement of the third-degree zonal term (O'Keefe et al., 1959). Modern geodesy combines both these terrestrial and satellite-based observations to estimate the gravity field. A comprehensive history of gravity estimation, up to the time of publication, may be found in Nerem et al. (1995). These first efforts laid the foundations for the gravity field estimation techniques employed today, and were efficient and well suited to the capabilities of the time. However, modern computers, which provide more memory and parallel processing capabilities, provide opportunities for improved gravity estimation.

Accuracy and resolution of gravity models improved considerably with the emergence of satellite geodesy. A lack of terrestrial-based gravity measurements over large bodies of water limited estimation of the global gravity field (Nerem et al., 1995). Satellite geodesy offers a solution to this problem by measuring perturbations in the satellite's orbit over these areas. Early altimetry missions yielded more data through the 1990's, culminating in the development of the 70×70 Joint Gravity Model 3 (JGM-3), which combined terrestrial observations with those of the TOPEX/Poseidon satellite (Tapley et al., 1996). Using highly-accurate range measurements between two satellites, the GRACE mission provides a means for estimating a 200×200 spherical harmonic model (Tapley et al., 2005). Such satellite-based observations, which offer higher temporal resolution, also provide information on the time-varying gravity field, i.e. changes in the gravity field caused by mass flow. Lemoine et al. (2010) consider these temporal changes to be one of the largest sources of error in modern precise orbit determination.

Estimating higher-resolution spherical harmonic models via satellite measurements fails to meet accuracy requirements for observing local gravity fluctuations. Observations of changes in the gravity field over a given area provide information on the change in mass over time, i.e. ice melt, rainfall, etc. Terrestrial methods for generating such observations require measurements covering large distances with adequate temporal resolution, and for extended periods of time. Such methods are inefficient and costly. Satellite geodesy offers an alternative method for monitoring such changes in the gravity field. Increased accuracy in space-based measurements of gravity provides information on the shorter-wavelength contributions, which allows for better spatial resolution of the estimated

model. Thus, localized models may be derived from the spherical harmonic model. However, these high-degree terms are highly dependent on the estimation algorithm and assumptions. For example, Sørensen and Forsberg (2010) demonstrate that different approximation techniques yield estimates in the change in mass of Greenland that differ by as much as 100 gigatons per year. Such discrepancies must be resolved before making quantitative conclusions based on the satellite determined temporal variations in the local gravity field.

1.2.3.2 Asteroid-Based Estimation

Interest in missions to small bodies, such as asteroids and comets, has grown considerably in recent years. One of the options proposed in the 2009 Review of the U. S. Human Spaceflight Plans Committee calls for the consideration of robotic and human missions to asteroids (Augustine et al., 2009). Beginning in 2000, the NEAR Shoemaker spacecraft (Cheng et al., 1997) inserted into orbit about the asteroid 433 Eros, and studied it for a year before landing. The Hayabusa satellite (Fujiwara et al., 2000) journeyed to 25143 Itokawa, and operated in a proximity of the asteroid for several months before landing, collecting a sample, and returning in June of 2010. Additionally, the DAWN satellite (Russell et al., 2004), which was launched in 2007, will explore the dwarf-planet Ceres and the asteroid 4 Vesta in the next three years. The ESA Rosetta (Glassmeier et al., 2007) mission, the joint Russia and China mission Phobos-Grunt (Marov et al., 2004), NASA Goddard's proposed OSIRIS-REx, and the potential JAXA Hayabusa-2 are just a few of the planned missions to small bodies currently in development.

The planning and execution of these asteroid missions has identified new gravity estimation problems. Very little may be known about the gravity field of a target asteroid before arrival, thereby adding complications to initial mission design. The irregular shapes of these asteroids imply large gravity perturbations, requiring a staged approach. Unfortunately, the spherical harmonic model provides no natural description of such a mission design. Finally, for precision landing and operations close to the primary body, the likelihood of needing to evaluate a gravity model within the spherical harmonic model's circumscribing sphere increases.

Although we have little information on the gravity field of the asteroid before orbital operations, some methods exists for generating an initial approximation. We may observe interactions with other bodies to estimate the asteroid's mass, and thus its gravitational parameter. Additionally, radar derived models of the shape may be generated (Scheeres et al., 1996, 1998). With these initial estimates of the total mass and shape, we can estimate the gravity perturbations using a polyhedron representation with uniform density (Werner and Scheeres, 1997). However, there is no a priori knowledge of the gravity field error with this assumption. Takahashi and Scheeres (2010) demonstrate that a series of high-altitude flybys may be performed to estimate the low-degree terms. Although these methods may reduce the orbital mission time by providing a low-accuracy estimate of the gravity field, higher accuracy models, which are required for low-altitude operations or precise landing, must be made in situ.

When estimating the gravity field of a relatively unknown primary body, it is important to stage the estimation in a natural manner. In such a procedure, one would like to first obtain the low spatial frequencies of the model and, then, gradually higher spatial frequencies as we approach the body. The spherical harmonic model is ill-suited for such an approach since its components do not decay fast enough. For this reason, estimation within that model is done typically all at once using all available data, and after fixing the degree of the approximation.

(a) 25143 Itokawa   (b) 433 Eros
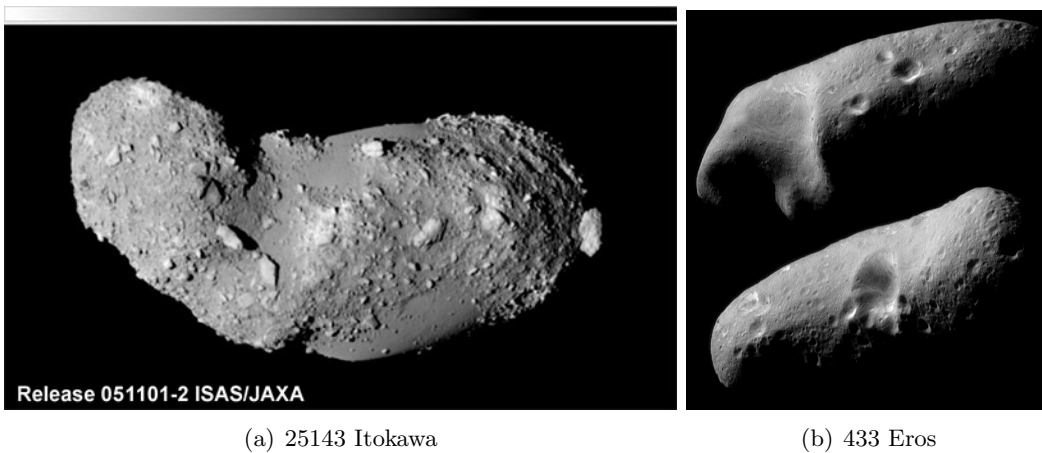
Figure 1.2: Asteroids 25143 Itokawa and 433 Eros, as seen from opposite sides

The primary concern for small-body gravity representations is the shape of the primary body. Irregularly shaped bodies pose problems for using the spherical harmonic models. As seen in Figure 1.2, the asteroids 433 Eros and 25143 Itokawa are roughly elliptical in shape. For this reason, the elliptical harmonics model is more appropriate than the spherical one. Results indeed demonstrate the advantages of the elliptical harmonics gravity model (Garmier et al., 2002). For both the spherical and elliptical harmonic models, the partial sum diverges for points within the circumscribing sphere (or ellipsoid), thus limiting the minimum valid altitude. Unfortunately, not all asteroids are ellipsoidal and, thus, other gravity representations suited for a more-or-less arbitrary shape are desired.

Several models have attempted to solve the issue of shape. Werner and Scheeres (1997) models the asteroid as a constant density polyhedron that converges on a solution for all points outside of the object. Gravity estimation methods have been suggested (Scheeres et al., 2000), but such a model is computationally expensive (Werner and Scheeres, 1997). The pubtree model, the interpolation model based on the polyhedron, improves computational efficiency but is poorly suited for estimation (Colombi et al., 2009). Park et al. (2010) considers an alternate approach, representing the body as a collection of spheres (or cubes) with fixed locations, and estimating the mass of each element. However, this model may become computationally expensive and the estimation problem ill-conditioned if the number of masses is large. Additionally, these models do not yield a staged approach.

1.3   Dissertation Overview

In this research, we apply the cubed-sphere model and a new multiresolution model (MRQ-Sphere) to fast orbit propagation and gravity estimation, respectively. For the cubed-sphere model, we assess improvements in computational efficiency, while also characterizing any changes in propagated trajectories. Given this characterization, we then integrate the model with the orbit determination process, thus allowing for high-fidelity satellite state estimation with little or no sacrifice in computation cost. The MRQSphere model uses quadratures (for the sphere) invariant under the

icosahedral group, which we apply to the estimation problem for a simplified mission to 433 Eros. In this study, we do not address the issues of shape of the primary body and leave this issue for the future. This study proves the model may be used for estimation, and justifies future work.

In Chapter 2, we present the gravity models used throughout this document. The reader will find detailed descriptions of the cubed-sphere and the MRQSphere models. We also present pertinent mathematical tools used in formulating these representations. In Chapter 3, we briefly present the orbit determination tools used in this research. We do not provide detailed derivations, but present the algorithms and principle equations for future discussion. In Chapter 4, we discuss the methods used to configure the cubed-sphere and MRQSphere models. This includes a presentation of the trade-offs, i.e. speed for memory, that must be considered by the user before generating the model. We establish a framework for model configuration, which we use in the remainder of the document. Chapter 5 characterizes orbit propagation errors and computation improvements when using the cubed-sphere model. We integrate the cubed-sphere model with the orbit determination process and present results in Chapter 6. This includes an expansion in the number of models represented, when compared to Chapter 5, and their impacts on the orbit determination process. Chapter 7 characterizes the use of the MRQSphere model for gravity estimation. Specifically, this chapter applies the model to an asteroid, and, using a simplified simulation, verifies the model may be used for gravity estimation. Finally, Chapter 8 presents a summary of research contributions, conclusions, and describes future work to characterize these new gravity models.

Chapter 2

Modeling the Gravity Field

As a satellite orbits a primary body, gravity perturbations cause deviations from a Keplerian orbit. As mentioned in Chapter 1, there are several methods for mathematically describing these perturbations. This chapter provides an overview of the gravity models used throughout this document. We begin with a presentation of the different forms of the spherical harmonic model, which includes the classical, Pines, and the Cartesian models. Next, we present a simple point-mass model. The last two sections describe the new models profiled in the document. Section 2.3 describes the cubed-sphere gravity model. This description includes a brief overview of the mathematical tool employed, and finally a description of the full model. Finally, Section 2.4 presents the MRQSphere model, including a mathematical overview and a model description.

2.1   Spherical Harmonic Models

Newton's Universal Law of Gravitation states the attraction between two particles may be written as

$$\mathbf{F} = M_2\ddot{\mathbf{r}} = G\frac{M_1 M_2}{r^2}\hat{\mathbf{r}} \tag{2.1}$$

where G is the gravitational constant, M_1 and M_2 are the masses of the primary and secondary bodies, respectively, and r is the distance between them in direction $\hat{\mathbf{r}}$. When combined with Newton's Second Law, we have

$$\ddot{\mathbf{r}} = \frac{\mu}{r^2}\hat{\mathbf{r}} \tag{2.2}$$

where the gravitation parameter μ is simply GM_1. This acceleration vector may also be derived by evaluating the gradient of the potential function

$$U = \frac{\mu}{r},$$

(2.3)

which satisfies Laplace's equation

$$\nabla^2 U = \frac{\partial^2 U}{\partial x^2} + \frac{\partial^2 U}{\partial y^2} + \frac{\partial^2 U}{\partial z^2} = 0.$$

(2.4)

The above equations treat the primary body with mass M_1 as a point mass. It is trivial to demonstrate the same equation holds true for the potential at a point outside of a sphere with uniform mass. Equation 2.4 remains valid for the gravity potential of any differential mass $\rho\, dx\, dy\, dz$, or the sum of any such masses (Kaula, 1966). Thus, any representation of the gravity potential must satisfy Laplace's Equation.

One solution to Laplace's Equation, with boundary values on the surface of the sphere, is found via the spherical harmonics. This spherical harmonic model represents variations in the gravity field as a sum of orthogonal functions on the sphere. In one of its most common forms, we write the spherical harmonic gravity model

$$U(r, \phi, \lambda) = \frac{\mu}{r} \sum_{n=2}^{\infty} \left(\frac{R}{r}\right)^n \sum_{m=0}^{n} \bar{P}_{n,m}\left[\sin(\phi)\right] \left\{\bar{C}_{n,m} \cos(m\lambda) + \bar{S}_{n,m} \sin(m\lambda)\right\}$$

(2.5)

where R is the primary body reference radius, the spherical coordinates r, ϕ, and λ correspond to the radius, geocentric latitude, and longitude, respectively, $\bar{P}_{n,m}[x]$ are the associated Legendre functions of degree n and order m, and the Stokes coefficients $\bar{C}_{n,m}$ and $\bar{S}_{n,m}$ describe the specific model. We note that the bar above a given variable refers to the normalized form of the given variable. Kaula normalization (Kaula, 1966) is of the form

$$S_{n,m} = \frac{\bar{S}_{n,m}}{\Pi_{n,m}} \qquad C_{n,m} = \frac{\bar{C}_{n,m}}{\Pi_{n,m}} \qquad P_{n,m} = \Pi_{n,m} \bar{P}_{n,m}.$$

(2.6)

where

$$\Pi_{n,m} = \sqrt{\frac{(n+m)!}{(n-m)!(2-\delta_{0m})(2n+1)}}.$$

(2.7)

δ_{0m} is the Kronecker delta, i.e. $\delta_{0m} = 1$ for $m = 0$ and $\delta_{0m} = 0$ for $m \neq 0$. For unit $C_{n,m}$ and $S_{n,m}$, this normalization yields a value of 4π when integrating the inner sum of Equation 2.5 over the sphere. The amplitude and phase of these functions are determined by the model specific Stokes coefficients, while frequency results from the degree and order of the specific term. The following sections discuss the Legendre functions and the different forms of the spherical harmonics model used in this document.

2.1.1   Associated and Derived Legendre Functions

Before discussing the full model, it is prudent to describe the functions used to model the variations in the gravity field on the sphere. Specifically, we discuss the variations as a function of the geocentric latitude ϕ for different degree n and order m. In the spherical harmonic model, these variations are often represented by the associated Legendre functions (ALFs) $P_{n,m}[x]$. For large degree models, specifically those greater than degree 150, we require a fully normalized form of the ALFs to prevent overloading of the double precision floating point values. We use the method of Rapp (1982) to generate the fully normalized ALFs, or

$$
\begin{aligned}
\bar{P}_{0,0}[x] &= 1 \\
\bar{P}_{1,0}[x] &= \sqrt{3}x \\
\bar{P}_{1,1}[x] &= \sqrt{3}(1-x^2)^{1/2} \\
\bar{P}_{n,n}[x] &= \sqrt{\frac{2n+1}{2n}}(1-x^2)^{1/2}\bar{P}_{n-1,n-1}[x] \qquad n > 1 \\
\bar{P}_{n,m}[x] &= B_{n,m}x\bar{P}_{n-1,m}[x] - \frac{B_{n,m}}{B_{n-1,m}}\bar{P}_{n-2,m}[x] \qquad m < n
\end{aligned}
\tag{2.8}
$$

where

$$
B_{n,m} = \sqrt{\frac{(2n+1)(2n-1)}{(n+m)(n-m)}}.
\tag{2.9}
$$

Since the $B_{n,m}$ coefficients are not a function of x, they may be precomputed at software initialization and stored in memory for future use. The functions $P_{n,0}$ are also known as the Legendre polynomials. Several forms of the ALFs exist, most notably those provided in Hofmann-Wellenhof

and Moritz (2006), Kaula (1966), the Tscherning (1976) reformulation of Clenshaw (1955), and Colombo (1981). Although Tscherning (1976) indicates the method of Rapp (1982) is not the most computationally efficient, Lundberg and Schutz (1988) demonstrated it is the most numerically stable of the fully normalized methods for large degree n.

Both the Pines and Cartesian models (described below) require a reformulation of the ALFs, called the derived Legendre functions $A_{n,m}[x]$ (DLFs). The ALFs are related to the DLFs by

$$P_{n,m}[x] = (1 - x^2)^{m/2} A_{n,m}[x].$$
(2.10)

Lundberg and Schutz (1988) recommend the DLF formulation

$$
\begin{aligned}
\bar{A}_{0,0}[\alpha] &= 1 \\
\bar{A}_{1,0}[\alpha] &= \alpha\sqrt{3} \\
\bar{A}_{1,1}[\alpha] &= \sqrt{3} \\
\bar{A}_{n,n}[\alpha] &= \sqrt{\frac{2n+1}{2n}}\,\bar{A}_{n-1,n-1}[\alpha] \qquad n > 1 \\
\bar{A}_{n,m}[\alpha] &= \alpha B_{n,m}\bar{A}_{n-1,m}[\alpha] - \frac{B_{n,m}}{B_{n-1,m}}\bar{A}_{n-2,m}[\alpha] \qquad m < n
\end{aligned}
$$
(2.11)

where we provided $B_{n,m}$ in Equation 2.9. The method of Equation 2.11 is the DLF form of the ALF formulation of Rapp (1982).

2.1.2   The Classic Formulation

The *classic model* refers to the model presented in Equation 2.5, and discussed in many basic astrodynamics texts (e.g. Kaula, 1966; Vallado and McClain, 2007; Bate et al., 1971; Tapley et al., 2004b). This model has been studied extensively in the literature (e.g. Deprit, 1979; Cunningham, 1970; Tscherning et al., 1983; Melvin, 1985), and is characterized by the method used to solve for the ALFs. The acceleration vector, in Cartesian coordinates, at a given point is found using

$$\ddot{\mathbf{r}} = \left(\frac{\partial r}{\partial \mathbf{r}}\right)^T \frac{\partial U}{\partial r} + \left(\frac{\partial \phi}{\partial \mathbf{r}}\right)^T \frac{\partial U}{\partial \phi} + \left(\frac{\partial \lambda}{\partial \mathbf{r}}\right)^T \frac{\partial U}{\partial \lambda},$$
(2.12)

where

$$\frac{\partial r}{\partial \mathbf{r}} = \begin{bmatrix} \dfrac{x}{r} & \dfrac{y}{r} & \dfrac{z}{r} \end{bmatrix}^T$$

$$\frac{\partial \phi}{\partial \mathbf{r}} = \frac{1}{\sqrt{x^2+y^2}} \begin{bmatrix} -\dfrac{xz}{r^2} & -\dfrac{yz}{r^2} & 1-\dfrac{z^2}{r^2} \end{bmatrix}^T \qquad (2.13)$$

$$\frac{\partial \lambda}{\partial \mathbf{r}} = \frac{1}{x^2+y^2} \begin{bmatrix} -y & x & 0 \end{bmatrix}^T.$$

Upon differentiating Equation 2.5, the partials required for Equation 2.12 are

$$\frac{\partial U}{\partial r} = -\frac{\mu}{r^2} \sum_{n=2}^{\infty} \sum_{m=0}^{n} \left(\frac{R}{r}\right)^n (n+1)\bar{P}_{n,m}\left[\sin(\phi)\right]\{\bar{C}_{n,m}\cos(m\lambda)+\bar{S}_{n,m}\sin(m\lambda)\}$$

$$\frac{\partial U}{\partial \phi} = \frac{\mu}{r} \sum_{n=2}^{\infty} \sum_{m=0}^{n} \left(\frac{R}{r}\right)^n \{\bar{P}_{n,m+1}[\sin(\phi)]\Pi'_{n,m} - m\tan(\phi)\bar{P}_{n,m}[\sin(\phi)]\}$$
$$\times \{\bar{C}_{n,m}\cos(m\lambda)+\bar{S}_{n,m}\sin(m\lambda)\} \qquad (2.14)$$

$$\frac{\partial U}{\partial \lambda} = \frac{\mu}{r} \sum_{n=2}^{\infty} \sum_{m=0}^{n} \left(\frac{R}{r}\right)^n m\bar{P}_{n,m}[\sin(\phi)]\{\bar{S}_{n,m}\cos(m\lambda)-\bar{C}_{n,m}\sin(m\lambda)\}$$

where

$$\Pi'_{n,m} = \sqrt{\frac{(n+m+1)(n-m)(2-\delta_{0m})}{2}}. \qquad (2.15)$$

As seen in the result for $\partial\phi/\partial\mathbf{r}$, there is a singularity at the poles for this model. We must include the scale factor $\Pi_{n,m+1}/\Pi_{n,m}$ in $\partial U/\partial\phi$ to ensure proper cancellation of the normalization factors. We compute the values of $\Pi'_{n,m}$ at initialization and store them in memory to reduce computation time.

2.1.3   The Pines Formulation

A second formulation represents the gravity field without the presence of a singularity at the poles. This *Pines model* (Pines, 1973) operates on the direction cosines of the coordinates, i.e. the satellite position is represented by

$$\mathbf{r} = r \begin{bmatrix} s \\ t \\ u \end{bmatrix} \qquad (2.16)$$

where

$$s = \frac{x}{r}, \quad t = \frac{y}{r}, \quad u = \frac{z}{r}. \tag{2.17}$$

The addition of a fourth term, r, adds a fourth partial sum. We use the implementation of the Pines model presented by Spencer (1976) with minor variations to improve computational efficiency. Specifically, we reorganize terms and use the normalized form of the DLFs previously described.

The Pines formulation of the gravity potential is

$$U(r, s, t, u) = \frac{\mu}{r} \sum_{n=0}^{\infty} \left(\frac{R}{r} \right)^n \sum_{m=0}^{n} \bar{A}_{n,m}[u] \bar{D}_{n,m}, \tag{2.18}$$

where $\bar{D}_{n,m}$ will be defined shortly. When removing the singularity at the poles, a $1/\cos^m(\phi)$ factor was introduced (Lundberg and Schutz, 1988). This factor was then incorporated into the recursion relation for the ALFs, resulting in the creation of the DLFs. Variations in the longitudinal direction are represented by

$$p_0 = 1 \tag{2.19}$$

$$q_0 = 0 \tag{2.20}$$

$$p_m = s p_{m-1} - t q_{m-1} \tag{2.21}$$

$$q_m = s q_{m-1} + t p_{m-1} \tag{2.22}$$

and

$$\bar{D}_{n,m} = \bar{C}_{n,m} p_m + \bar{S}_{n,m} q_m \tag{2.23}$$

$$\bar{E}_{n,m} = \bar{C}_{n,m} p_{m-1} + \bar{S}_{n,m} q_{m-1} \tag{2.24}$$

$$\bar{F}_{n,m} = \bar{S}_{n,m} p_{m-1} - \bar{C}_{n,m} q_{m-1}. \tag{2.25}$$

The acceleration is found by evaluating

$$\ddot{\mathbf{r}} = \begin{bmatrix} a_1 \\ a_2 \\ a_3 \end{bmatrix} + a_4 \begin{bmatrix} s \\ t \\ u \end{bmatrix} \tag{2.26}$$

where

$$a_1 = \frac{\mu}{Rr} \sum_{n=0}^{\infty} \left(\frac{R}{r}\right)^{n+1} \sum_{m=0}^{n} m \bar{A}_{n,m}[u] \bar{E}_{n,m} \tag{2.27}$$

$$a_2 = \frac{\mu}{Rr} \sum_{n=0}^{\infty} \left(\frac{R}{r}\right)^{n+1} \sum_{m=0}^{n} m \bar{A}_{n,m}[u] \bar{F}_{n,m} \tag{2.28}$$

$$a_3 = \frac{\mu}{Rr} \sum_{n=0}^{\infty} \left(\frac{R}{r}\right)^{n+1} \sum_{m=0}^{n} \bar{A}_{n,m+1}[u] \bar{D}_{n,m} \frac{\Pi'_{n,m+1}}{\Pi'_{n,m}} \tag{2.29}$$

$$a_4 = -\frac{\mu}{Rr} \sum_{n=0}^{\infty} \left(\frac{R}{r}\right)^{n+1} \sum_{m=0}^{n} \bar{A}_{n+1,m+1}[u] \bar{D}_{n,m} \frac{\Pi'_{n+1,m+1}}{\Pi'_{n,m}}. \tag{2.30}$$

When evaluating the Pines model of degree n, the derived Legendre functions of degree $n+1$ are required, which reduces the computational performance. The Pines model has since been improved by Fantino and Casotto (2009), but this new implementation was not considered for this research.

2.1.4   The Cartesian Formulation

The *Cartesian model* (Gottlieb, 1993) (sometimes referred to as the Gottlieb model) is a reformulation of the Pines model to operate directly on the planet-centered, planet-fixed Cartesian coordinates. Like the Pines model, the Cartesian model introduces a fourth term to prevent ambiguity at the poles. Thus, several similarities will be immediately evident. However, only the derived Legendre functions up to degree n are required.

The Cartesian formulation of the gravity potential is

$$U = \frac{\mu}{r} + \frac{\mu}{r} \sum_{n=2}^{\infty} \left(\frac{R}{r}\right)^{n} \sum_{m=0}^{n} \bar{A}_{n,m} \left[\frac{z}{r}\right] \bar{D}_{n,m} \tag{2.31}$$

with the acceleration vector found by evaluating

$$\ddot{\mathbf{r}} = -\frac{\mu}{r^3} \mathbf{r} + \frac{\mu}{r^2} \left[\begin{bmatrix} a_1 \\ a_2 \\ a_3 \end{bmatrix} - \left(\frac{z a_3}{r} + a_4\right) \frac{\mathbf{r}}{r} \right]. \tag{2.32}$$

The variations in the longitudinal direction are also described by

$$\bar{p}_0 \;=\; 1 \tag{2.33}$$

$$\bar{q}_0 \;=\; 0 \tag{2.34}$$

$$\bar{p}_1 \;=\; \frac{x}{r} \tag{2.35}$$

$$\bar{q}_1 \;=\; \frac{y}{r} \tag{2.36}$$

$$\bar{p}_m \;=\; \bar{p}_1\bar{p}_{m-1} - \bar{q}_1\bar{p}_{m-1} \tag{2.37}$$

$$\bar{q}_m \;=\; \bar{q}_1\bar{q}_{m-1} + \bar{p}_1\bar{q}_{m-1} \tag{2.38}$$

and

$$\bar{D}_{n,m} \;=\; \bar{C}_{n,m}\bar{p}_m + \bar{S}_{n,m}\bar{q}_m \tag{2.39}$$

$$\bar{E}_{n,m} \;=\; \bar{C}_{n,m}\bar{p}_{m-1} + \bar{S}_{n,m}\bar{q}_{m-1} \tag{2.40}$$

$$\bar{F}_{n,m} \;=\; \bar{S}_{n,m}\bar{p}_{m-1} - \bar{C}_{n,m}\bar{q}_{m-1} \tag{2.41}$$

The a_i coefficients are then

$$a_1 \;=\; \sum_{n=2}^{\infty}\left(\frac{R}{r}\right)^n \sum_{m=1}^{n} m\bar{A}_{n,m}\left[\frac{z}{r}\right]\bar{E}_{n,m} \tag{2.42}$$

$$a_2 \;=\; \sum_{n=2}^{\infty}\left(\frac{R}{r}\right)^n \sum_{m=1}^{n} m\bar{A}_{n,m}\left[\frac{z}{r}\right]\bar{F}_{n,m} \tag{2.43}$$

$$a_3 \;=\; \sum_{n=2}^{\infty}\left(\frac{R}{r}\right)^n \sum_{m=0}^{n} \bar{A}_{n,m+1}\left[\frac{z}{r}\right]\bar{D}_{n,m}\frac{\Pi'_{n,m+1}}{\Pi'_{n,m}} \tag{2.44}$$

$$a_4 \;=\; \sum_{n=2}^{\infty}\left(\frac{R}{r}\right)^n \sum_{m=0}^{n} (n+m+1)\bar{A}_{n,m}\left[\frac{z}{r}\right]\bar{D}_{n,m}. \tag{2.45}$$

2.2   Point-Mass Model

The *point-mass model* refers to a gravity field resulting from a collection of N point masses within a given spherical volume with radius R_p. Each point mass is described by the values η_i and $\mathbf{R}_i$, which represent the mass and position of mass i, respectively. The total gravitation acceleration ($\ddot{\mathbf{r}}_p$) is

$$\ddot{\mathbf{r}}_p = -G\sum_{i=1}^{N}\frac{\eta_i\,(\mathbf{r}-\mathbf{R}_i)}{\left|\mathbf{r}-\mathbf{R}_i\right|^3} \tag{2.46}$$

and the gravity potential is

$$U(\mathbf{r}) = -G \sum_{i=1}^{N} \frac{\eta_i}{|\mathbf{r} - \mathbf{R}_i|}. \tag{2.47}$$

We use

$$G = 6.67428 \times 10^{-20} \quad \text{km}^3/(\text{kg} \cdot \text{sec}^2) \tag{2.48}$$

for the gravity constant (Mohr et al., 2007).

We may represent a point-mass model using a spherical harmonic expansion. For a given set of point masses,

$$\bar{C}'_{n,m} = \frac{1}{M(2n+1)} \sum_{i=1}^{N} \left(\frac{r_i}{R_p}\right)^n \bar{P}_{n,m}[\sin(\phi_i)] \cos(m\lambda_i)\eta_i \tag{2.49}$$

$$\bar{S}'_{n,m} = \frac{1}{M(2n+1)} \sum_{i=1}^{N} \left(\frac{r_i}{R_p}\right)^n \bar{P}_{n,m}[\sin(\phi_i)] \sin(m\lambda_i)\eta_i, \tag{2.50}$$

where (R_i, ϕ_i, λ_i) is the location of the i-th point mass in spherical coordinates, and

$$M = \sum_{i=1}^{N} \eta_i. \tag{2.51}$$

Equations 2.49 and 2.50 are presented in Thompson et al. (2008), with alterations to yield the normalized Stokes coefficients.

2.3   Cubed-Sphere Gravity Model

Originally proposed in Beylkin and Cramer (2002), the cubed-sphere model defines a new method to compute geopotential and acceleration. Essentially, the sphere is mapped to a cube with a new coordinate system defined on each face. Each face is segmented by an uniform grid and interpolation is performed to find the acceleration. Multiple spheres, each mapped to a cube, are nested within each other and interpolation is performed between adjacent shells to account for the acceleration variation in the radial direction. The mapping of a sphere to a cube is illustrated in Figure 2.1. A grid spacing scheme is established with values for acceleration precomputed at intersections of the grid lines. Basis splines, or B-splines, were selected to represent functions on each face of the cube. The following sections describe the cubed-sphere model in detail.
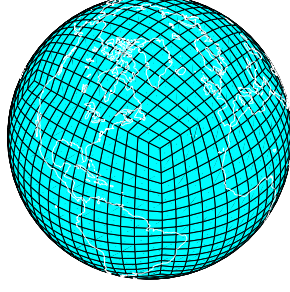
Figure 2.1: Illustration of the mapping from a sphere to a cube.

A major goal of the cubed-sphere model development is to improve computational efficiency in using geopotential models. Effectively, it is a trade of speed for memory, i.e. file size. However, a modern computer has more than the sufficient memory for this purpose.

2.3.1 Basis Spline Interpolation

Future sections of this chapter assume a fundamental understanding of basis splines, or B-splines. Thus, we include a basic description here. This includes a general discussion of B-splines, B-spline interpolation, and a fast Fourier transform (FFT) algorithm for generating interpolation coefficients.

After selecting a set of n nodes $\mathbb{T} = t_0, \ldots, t_{n-1}$, called knots, a B-spline may be defined by

$$B_{jm}(x) = \omega_{jm}B_{j,m-1}(x) + (1 - \omega_{j+1,m})B_{j+1,m-1}(x) \tag{2.52}$$

where m is the degree of the spline, j is an index,

$$\omega_{jm} = \frac{x - t_j}{t_{j+m} - t_j}, \tag{2.53}$$

and

$$B_{j0}(x) = \begin{cases} 1, & t_j \le x < t_{j+1} \\ 0, & otherwise. \end{cases} \tag{2.54}$$

For $\mathbb{T}$ and B-splines of degree m, there are $n - m - 1$ piecewise polynomials defined by Equation 2.52 that are nonzero in the range $[t_0, t_{n-1})$.

As indicated by Equations 2.53 and 2.54, nodes govern the shape and range of a given B-spline. Several of these polynomials are illustrated in Figure 2.2 using the knots and degree indicated. We note the increase in sharpness of the peaks corresponding to locations of repeated roots and lower degree. Repeated roots may create a discontinuity, which has been illustrated for completeness. The cubed sphere does not include any repeated roots, thus this discontinuity is not an issue. A thorough discussion of the node and degree relationship may be found in deBoor (2001).

We commonly use B-splines to approximate a function $g(x)$ by

$$g(x) \approx \tilde{g}(x) = \sum_{j=0}^{n-m-2} \alpha_j B_{jm}(x) \tag{2.55}$$

for x in the range defined by $\mathbb{T}$. After a selection of $\mathbb{T}$ and m, we may determine the weights α_j to best approximate $g(x)$ when given $\gamma_i = g(x_i)$ at a sequence of data sites x_i. Knots and data sites may not necessarily coincide. Like any interpolation scheme, we may control accuracy by the knot density and the degree of the basis functions.
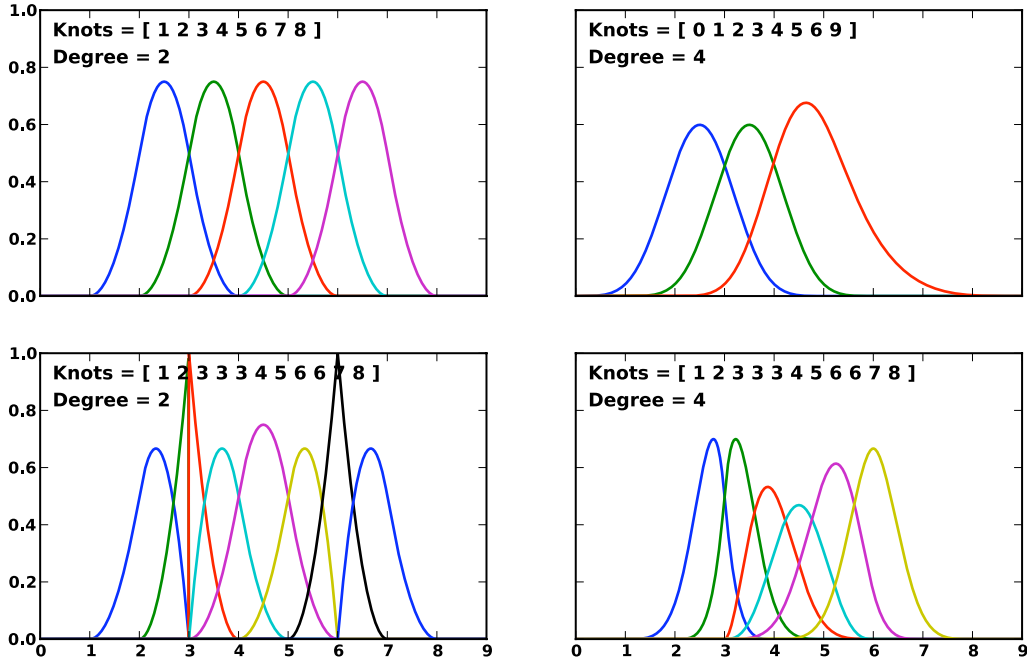
Figure 2.2: Example B-splines for various degree m and knots $\mathbb{T}$.

We now derive an algorithm to solve for the weights α_j in the frequency domain using Cardinal

B-splines. A Cardinal B-spline is centered at one of a set of equally spaced knots t_j. We may define such a B-spline as the convolution

$$B_m(x) = (B_{m-1} * B_0)(x), \tag{2.56}$$

where

$$B_0(x) = \begin{cases} 1, & |x| \leq \frac{1}{2} \\ 0, & \text{otherwise.} \end{cases} \tag{2.57}$$

For our purposes, we only consider B-splines of odd degree m, thus B_m, being centered at t_j, is an even function and nonzero only in the interval $[t_j - (m+1)/2, t_j + (m+1)/2]$. We dropped the index term j since Cardinal B-splines are simply an integer translation of each other, and may be accounted for in the independent variable x. On taking the Fourier transform of B_0,

$$\int_{-\infty}^{+\infty} B_0(x)e^{-2\pi i x \xi}dx = \frac{\sin \pi \xi}{\pi \xi}, \tag{2.58}$$

we obtain

$$\int_{-\infty}^{+\infty} B_m(x)e^{-2\pi i x \xi}dx = \left(\frac{\sin \pi \xi}{\pi \xi}\right)^{m+1}. \tag{2.59}$$

For our purposes, we use a periodized version of B-splines on the interval $[0, 1]$. Subdividing $[0, 1]$ into $N = 2^k$ subintervals, where $N \geq m + 1$ (in practice $N \gg m + 1$), we consider the basis of B-splines on this subdivision,

$$\{B_m(Nx - j)\}_{j=0,1,\ldots,2^k-1}. \tag{2.60}$$

Let us consider a function $g(x)$ that may be written as

$$g(x) = \sum_{j=0}^{N-1} \alpha_j B_m(Nx - j). \tag{2.61}$$

Instead of using the basis of B-splines, we may also write the same function as

$$g(x) = \sum_{j=0}^{N-1} \gamma_j L_m(Nx - j) \tag{2.62}$$

where L_m are interpolating splines of a given degree m, i.e.

$$L_m(l) = \delta_{l,0}, \tag{2.63}$$

where l is an integer and $\delta_{i,j}$ is the Kronecker delta function. The definition of interpolating splines implies that the coefficients in Equation 2.62 are, in fact, the values of the function $g(x)$ on the lattice,

$$\gamma_l = g(l/N). \tag{2.64}$$

In our problem, we are given the values $\gamma_l = g(l/N)$ and need to find the coefficients α_j in Equation 2.61. We have

$$\int_0^1 B_m(Nx - j)e^{-2\pi ixn}dx = \frac{1}{N}\hat{B}_m\left(\frac{n}{N}\right)e^{-2\pi ijn/N}, \tag{2.65}$$

and computing the Fourier coefficients of g in Equation 2.61, we obtain

$$\hat{g}_n = \left(\frac{1}{N}\sum_{j=0}^{N-1}\alpha_j e^{-2\pi ijn/N}\right)\hat{B}_m\left(\frac{n}{N}\right) = \hat{\alpha}_n\hat{B}_m\left(\frac{n}{N}\right). \tag{2.66}$$

Similarly, we compute the Fourier coefficients of g in terms of interpolating splines,

$$\hat{g}_n = \left(\frac{1}{N}\sum_{j=0}^{N-1}\gamma_j e^{-2\pi ijn/N}\right)\hat{L}_m\left(\frac{n}{N}\right) = \hat{\gamma}_n\hat{L}_m\left(\frac{n}{N}\right). \tag{2.67}$$

The B-splines and the interpolating splines are related by (see, e.g., Chui (1992))

$$\hat{L}_m\left(\frac{n}{N}\right) = \frac{\hat{B}_m\left(\frac{n}{N}\right)}{a\left(\frac{n}{N}\right)} \tag{2.68}$$

where

$$a(\omega) = \sum_{j\in\mathbb{Z}}\left|\hat{B}_m(\omega + j)\right|^2. \tag{2.69}$$

It may be shown that $a(\omega)$ is a trigonometric polynomial (see, e.g., Chui (1992))

$$\sum_{j\in\mathbb{Z}}\left|\hat{B}_m(\omega + j)\right|^2 = \sum_{l=-m}^{m}B_{2m+1}(l)e^{-2\pi il\omega}, \tag{2.70}$$

thus simplifying the evaluation of $a(\omega)$. Finally, substituting Equation 2.68 into Equation 2.67, we get

$$\hat{g}_n = \hat{\gamma}_n\frac{\hat{B}_m\left(\frac{n}{N}\right)}{a\left(\frac{n}{N}\right)}, \tag{2.71}$$

which implies

$$\hat{\alpha}_n = \frac{\hat{\gamma}_n}{a\left(\frac{n}{N}\right)}. \tag{2.72}$$

In other words, applying the discrete Fourier transform to the data values $\gamma_l = g(l/N)$, scaling by the factor $1/a\left(\frac{n}{N}\right)$ and applying the inverse discrete Fourier transform, we obtain the coefficients α_j in Equation 2.61. The two dimensional case is a straightforward extension, where

$$\hat{\alpha}_{k,l} = \frac{\hat{\gamma}_{k,l}}{a\left(\frac{k}{N}\right) a\left(\frac{l}{N}\right)}. \tag{2.73}$$

2.3.2 Model Description

The cubed-sphere model may be used to approximate any number of elements defined on a primary body. For example, it can approximate each component of acceleration, or the gravity potential. The accelerations are not directly derived from the potential, but are stored separately (in a submodel). Thus, in order for a model to provide both potential and three components of acceleration, values of all four parameters are stored at each point for future interpolation. In the following sections, any reference to modeling the gravity potential may also be applied to modeling acceleration (with the appropriate adjustments). This description of the cubed-sphere model follows that of Jones et al. (2010b).

The cubed-sphere model is currently derived from an existing gravity model, hereafter called the base model. Although other models such as a polyhedron or mascon may serve this role, we currently use the spherical harmonic model as the base model. In the cubed-sphere model, the first four nonzero terms of the spherical harmonic expansion, i.e. the two-body term, J_2, the $(*)_{2,1}$, and $(*)_{2,2}$ terms are used directly. The cubed-sphere model does not include the lower order terms to reduce the range of approximated values, thereby decreasing the cost of maintaining accuracy in the local model. The geopotential values computed by the remaining terms in the base model are then represented by the basis functions on the surface of the cube.

Temporal variations, such as solid or liquid tides, influence the geopotential. These variations mostly affect lower degree terms of the potential. The cubed sphere only models terms of degree greater than or equal to a chosen minimum degree and order, in this case 3. This parameter may be adjusted to allow for perturbations in the lower degree terms while higher degree terms are expressed in the cubed-sphere formulation. Of course, this may slightly affect computation time.

A key parameter of the cubed-sphere model is the grid size, N. Similar to the degree and order of the spherical harmonic model, the grid size defines the density of the grid on each cube face and is a measure of model fidelity. For a given altitude, the values of latitude and longitude are segmented such that

$$\lambda = 2\pi x, \quad \phi = 2\pi y \tag{2.74}$$

where x and y are discrete values in the range $[0,1)$. In order to have a fast algorithm to compute coefficients of the B-splines from the values of the spherical harmonic model, the values of the latitude, ϕ, are extended to the interval $[0,2\pi)$. It may not be readily apparent how this is done, but this will be explained in a moment.

Latitude and longitude are mapped to a two dimensional grid, with spacing N^{-1}, specified by x and y to solve for the B-spline coefficients. As described in Section 2.3.1, the interpolation coefficients are easily computed in the Fourier domain. Since the grid variables x and y are 1-periodic, we may use the two-dimensional FFT algorithm to provide a fast method for finding the B-spline coefficients.

If ϕ only varies from $-\pi/2$ to $\pi/2$, or 0 to π, then y is not 1-periodic and the FFT algorithm cannot be used directly. To periodically extend the Earth's geopotential, we duplicate it to complete the period. The mathematical formulation of the new geopotential, U_p, is then

$$U_p(r, \phi, \lambda) = \begin{cases} U(r, \phi, \lambda) & \text{if } 0 \leq \phi < \pi, \\ U(r, 2\pi - \phi, \lambda + \pi) & \text{if } \pi \leq \phi < 2\pi, \end{cases} \tag{2.75}$$

and ϕ is now a value in the range $[0, 2\pi)$. Thus, U_p is 2π-periodic. The offset of the longitude by π in the second case of Equation 2.75 assures that all spherical harmonics are extended smoothly (with all derivatives) to the interval $[0,2\pi)$. One can see this by the fact that one period of ϕ circumscribes the primary body. Thus, U_p is infinitely differentiable in both variables so that the trapezoidal rule can be used to discretize the Fourier integrals. The FFT algorithm may be used directly to compute the B-spline coefficients. Note that the doubling of the geopotential model is only used to generate these coefficients.

To prevent grid distortion given the ambiguity of longitude at the poles, the coordinate system is rotated so that the poles lie along the equator, which is equivalent to using the transverse mercator map projection. A second x-y plane is generated after this rotation, with the FFT algorithm applied and a second set of B-spline coefficients determined. B-spline coefficients are defined over the surface of the two x-y grids, which are then broken into appropriate segments to generate the faces of a cube. Each cube face has a new x-y grid with axes defined over the range $[-1, 1]$. Four segments along the middle latitudes are selected from the first set of coefficients, with each segment corresponding to a cube face. The two remaining faces at the poles are selected from the second set. We illustrate this process in Figure 2.3.

Although grid spacing is preserved along the face of the cube, we note that the grid size on each face is $N/4$ by $N/4$. This parameter is used in the naming convention for a given model. A CS-X model is a cubed-sphere model where X corresponds to the grid size on a cube face, or $N/4$. To summarize, we have described the geopotential model at a given altitude on the surface of a cube.
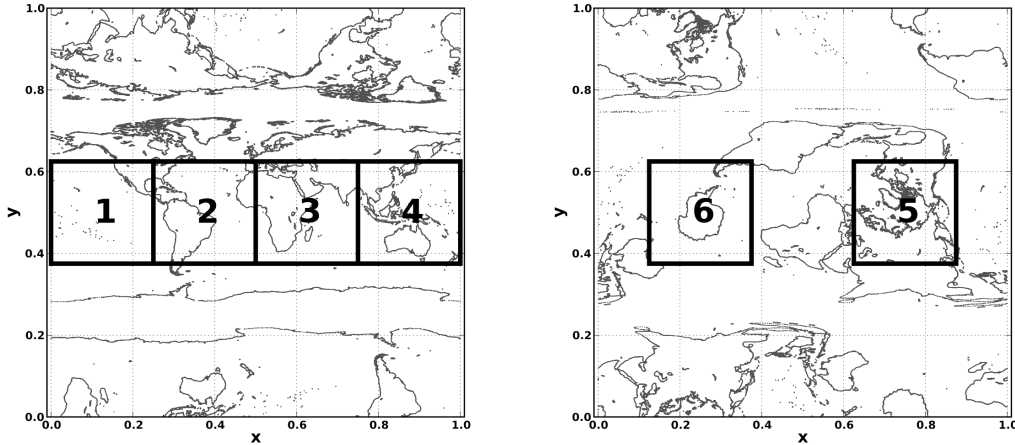
Figure 2.3: Illustration of the mapping of the Earth surface to a x-y plane to make U_p 2π-periodic. Selected portions form the cubed sphere. The second plot illustrates the process for the rotated coordinate system.

Since the spherical harmonics is a global model, an uniform grid density is forced over the complete surface to model the high frequency variations. Of course, a true Earth model will have relatively large variations in the gravity field as location changes. This is especially true along coastal and mountain regions. As discussed in Beylkin and Cramer (2002), the cubed sphere was originally developed with multiresolution techniques in mind. However, adjusting the grid density to these levels reveals noise in the original spherical harmonics terms. The noise could be removed, which effectively modifies some higher degree terms. Thus, the cubed sphere would no longer agree with the spherical harmonic model, which may currently cause resistance to its use. Additionally, early tests of the model for Beylkin and Cramer (2002) demonstrated only small gains in speed as a result of such change, and only a marginal decrease in memory required.
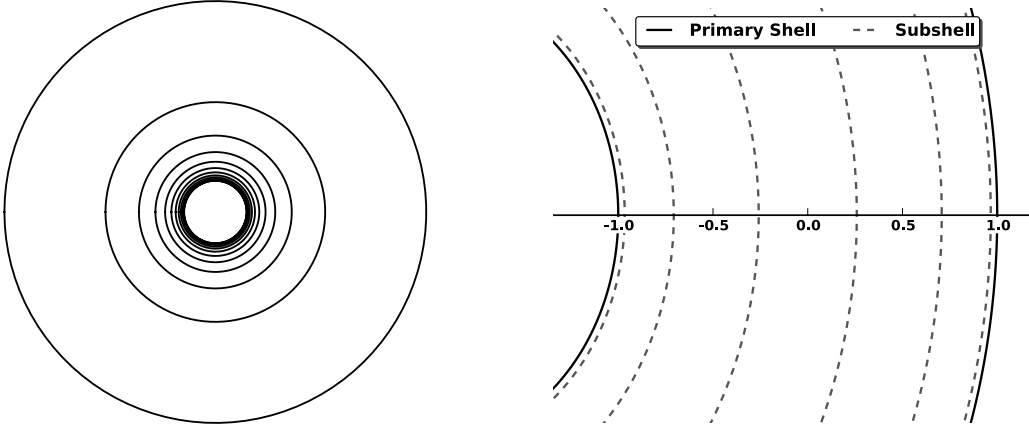
Figure 2.4: Illustration of the increased density of primary shells with closer proximity to the primary body (left figure), and an example of the subshell spacing between primary shells (right) for the cubed-sphere model.

A user specified number of nested, concentric shells is required for interpolation in the radial direction. Shell spacing is determined by defining a set number of points (h_j) equally spaced in the interval $[0, 1]$. Shell locations are then

$$\frac{R}{r_j} = 1 - h_j^2, \tag{2.76}$$

where r_j is the radial distance of the spherical shell. We note that as the shell radius, r_j, approaches infinity, R/r_j tends to 0. Shell density increases for lower altitudes, corresponding to the inverse

square relationship between geopotential and radius. This is illustrated in Figure 2.4. The final shell at infinity is used only as a boundary for determination of the subshells.

The primary shells each consist of subshells for interpolation in the radial direction. The cubed sphere approximates the potential using Chebyshev polynomial interpolation of degree l,

$$U(x) = \sum_{i=0}^{l} a_i T_i(x), \tag{2.77}$$

where a_i are (spatially dependent) coefficients and T_i are Chebyshev polynomials, values of which are computed via the three term recurrence,

$$T_0(x) = 1 \tag{2.78a}$$

$$T_1(x) = x \tag{2.78b}$$

$$T_i(x) = 2xT_{i-1}(x) - T_{i-2}(x). \tag{2.78c}$$

The space between subshells is mapped to the range $[-1, 1]$ where zero corresponds to the midpoint between primary shells. The subshells are then positioned at the roots of the $l+1$ degree Chebyshev polynomial (the so-called Gaussian nodes). This is illustrated in Figure 2.4 for a 5th degree Chebyshev scheme with six subshells. The Gaussian nodes are selected in order to minimize interpolation error (see, e.g., deBoor (2001)).

In generation of the cubed-sphere model, each subshell is independent of all others. B-spline coefficients for each subshell are generated as previously described using the applicable altitude for the evaluation of Equation 2.75. A total of $(l + 1) \times (M - 1)$ subshells are computed, where M is the number of primary shells. It is important to note that the mapping to the cube is simply used for data storage, finding the spline coefficients, and preventing a concentration of points at the poles. All values described by the model, more specifically components of acceleration, are still represented in the spherical coordinate system.

Grid density is kept constant for all subshells at all altitudes. Since the high-frequency variations in the spherical harmonics attenuate quickly with altitude, the required grid density for higher altitudes is less than those required closer to the planet. This has not been currently

integrated with the cubed sphere, but multiresolution techniques such as the one presented in Section 2.4 may be employed.

Continuity of the model determined values may be a concern for some applications. Primary shells may be generated to overlap. This has not yet been explored, but the multiresolution technique of Section 2.4 would eliminate this need. Given the lack of overlap in the primary shells, model discontinuities may exist at the primary shell boundary. However, proper configuration reduces these discontinuities to within the model noise. Specifically, the discontinuities are less than the machine precision for the given acceleration values. Discontinuities do not exist between faces of the cube since the FFT algorithm used to solve for the interpolation coefficients utilizes the entire gravity field at the given altitude.

Evaluation of the cubed-sphere model is fairly straightforward. Lower degree components of geopotential are computed directly using the spherical harmonic coefficients stored in the model. For higher degree terms, the point of interest is mapped to the cube. The value is obtained by the interpolation on the $l+1$ subshells within the primary shell containing the point of interest. The coefficients required for Equation 2.77 are then

$$a_i = \frac{2 - \delta_{i0}}{l+1} \sum_{j=0}^{l} U_j T_i(x_j), \tag{2.79}$$

where U_j is the potential on the j-th subshell at x_j, and δ_{ij} is the Kronecker delta function.

The conversion from spherical (ϕ, λ) to cube coordinates (x, y, n) is summarized in Table 2.1, and was adapted from Beylkin and Cramer (2002) with some simplifications and corrections of misprints. For the cube coordinates, n refers to the face of the cube. The first four faces represent the sphere at the middle latitudes between $-\pi/4$ and $\pi/4$, while faces 5 and 6 correspond to the polar regions. For faces 1-4, the conversion to the x-y coordinate system is simply a map from the appropriate angle range (e.g. $[-\pi, \pi/2)$) to [-1,1). The mappings for faces 5 and 6 result from rotating the sphere so that the poles lie on the equator. The original ϕ and λ values are converted to Cartesian coordinates, and then rotated about the x-axis by $-\pi/2$. The new Cartesian coordinates are converted to a new ϕ' and λ' and mapped to the range [-1,1) in a manner similar to faces 1-4.

The equations for faces 5 and 6 in Table 2.1 are derived from this procedure.

Table 2.1: Spherical to cube face coordinates conversion. Note $\gamma = -\cos\phi\sin\lambda$, $\omega = \tan\phi/\cos\lambda$, and $\alpha = 4/\pi$.

Face	Angle Ranges	X-coordinate	Y-coordinate
1	$-\pi \leq \lambda < -\pi/2, \quad -\pi/4 \leq \phi \leq \pi/4$	$\alpha\lambda + 3$	$\alpha\phi$
2	$-\pi/2 \leq \lambda < 0, \quad -\pi/4 \leq \phi \leq \pi/4$	$\alpha\lambda + 1$	$\alpha\phi$
3	$0 \leq \lambda < \pi/2, \quad -\pi/4 \leq \phi \leq \pi/4$	$\alpha\lambda - 1$	$\alpha\phi$
4	$\pi/2 \leq \lambda < \pi, \quad -\pi/4 \leq \phi \leq \pi/4$	$\alpha\lambda - 3$	$\alpha\phi$
5	$\phi > \pi/4$	$\alpha\tan^{-1}(\omega) - 2$	$\alpha\sin^{-1}(\gamma)$
6	$\phi < -\pi/4$	$\alpha\tan^{-1}(\omega) + 2$	$\alpha\sin^{-1}(\gamma)$

The number of elements that must be stored in the model may be found using

$$Number\ of\ elements = 6P(l+1)(M-1)\left(\frac{N}{4} + m\right)^2, \qquad (2.80)$$

where P is the number of submodels (i.e. three submodels for acceleration and one for potential), m is the degree of the B-spline interpolation scheme, and other values were defined previously. For a cubed-sphere model intended to represent the acceleration terms for a 20×20 spherical harmonic model using a fifth-degree Chebyshev interpolation, eleventh degree B-spline interpolation, 14 primary shells, and 20 grid lines per face ($N = 80$), the model requires 1,349,244 B-spline coefficients. Obviously, estimation of the model from satellite observations is intractable, thus we do not consider the problem of estimating terms of the cubed-sphere model using satellite geodesy techniques. The MRQSphere model, which we present in Section 2.4, describes a model optimized for the gravity estimation problem.

2.4   MRQSphere Model

In this section, we describe the mathematical tools employed to create the Multiresolution Representation using Quadratures for the Sphere model (MRQSphere). This includes a description of the quadratures for the sphere, and the approximation by Gaussians that allows for the multiresolution expression of the gravity field. We combine these tools to define the new model, and

provide the equations for evaluating the gravity potential, acceleration, and the Jacobian of the acceleration.

2.4.1   Quadratures for the Sphere

The standard model representing variations in the gravity field in the latitudinal and longitudinal directions uses the spherical harmonics, which are global functions on the sphere. An approach to replace them with better localized functions has been developed (Ahrens and Beylkin, 2009) and uses quadratures on the sphere invariant under the icosahedral group. Due to the invariance of the positions of the nodes under this discrete group, the nodes do not concentrate and have a near uniform distribution on the sphere. These quadratures are also near optimal, as far as the number of nodes required to integrate all spherical harmonics of a fixed degree and order. This combination of properties yields an analogue of the Lagrange-type interpolation on the sphere. As a result, we replace the spherical harmonics by a set of functions concentrated at the nodes of the quadrature and generated by a single function. Instead of estimating the coefficients of the spherical harmonics, the new quadratures allow direct estimation of the gravity field at the quadrature nodes. This section provides a brief introduction to the techniques introduced by Ahrens and Beylkin (2009).

Starting with Equation 2.5, and after representing the radial distance in units of primary body radius $\rho\ (= r/R)$, we write

$$U(\rho, \phi, \lambda) = \frac{\mu}{R} \sum_{n=0}^{\infty} \rho^{-(n+1)} V_n(\phi, \lambda) \tag{2.81}$$

where

$$V_n(\phi, \lambda) = \sum_{m=0}^{n} P_{n,m}[\sin \phi] \left(C_{n,m} \cos m\lambda + S_{n,m} \sin m\lambda \right). \tag{2.82}$$

Let $\mathcal{P}_N$ be the space of spherical harmonics of maximum degree and order N. Using the reproducing kernel,

$$K_N(\boldsymbol{\alpha} \cdot \boldsymbol{\alpha}') \equiv \sum_{n=0}^{N} \frac{2n+1}{4\pi} P_{n,0}(\boldsymbol{\alpha} \cdot \boldsymbol{\alpha}'), \tag{2.83}$$

for any function f in $\mathcal{P}_N$, we have

$$f(\boldsymbol{\alpha}) = \int_{\mathbb{S}^2} K_N(\boldsymbol{\alpha} \cdot \boldsymbol{\alpha}')f(\boldsymbol{\alpha}')d\boldsymbol{\alpha}', \qquad (2.84)$$

where $\boldsymbol{\alpha}$ and $\boldsymbol{\alpha}'$ denote unit vectors on the sphere $\mathbb{S}^2$. A more detailed discussion of the reproducing kernel may be found in Ahrens and Beylkin (2009).

Discretizing Equation 2.84 using quadratures with M nodes to integrate all functions in the subspace $\mathcal{P}_{2N}$, we obtain an analogue of Lagrange interpolation on the sphere. In Ahrens and Beylkin (2009), the location of the nodes $(\boldsymbol{\alpha}_i)$ have been chosen to be invariant under the rotations of the discrete icosahedral group, thus preventing them from concentrating at any particular location. As a result, we have

$$f(\boldsymbol{\alpha}) = \sum_{j=1}^{M} K_N(\boldsymbol{\alpha} \cdot \boldsymbol{\alpha}_j)w_j f(\boldsymbol{\alpha}_j) \qquad (2.85)$$

where w_j are the weights of the quadratures and $f(\boldsymbol{\alpha}_j)$ are the values of the function at the nodes. The number of nodes M is chosen to integrate exactly the product of the two functions K_N and f, whose degree and order does not exceed $2N$. As an example, for approximating the gravity field of degree 7, we use the number of nodes necessary to integrate the subspace $\mathcal{P}_{14}$. In Figure 2.5, we provide examples where N refers to the maximum degree of the function in the Lagrange-type interpolation.

(a) 2N=14, 72 Points   (b) 2N=30, 372 Points
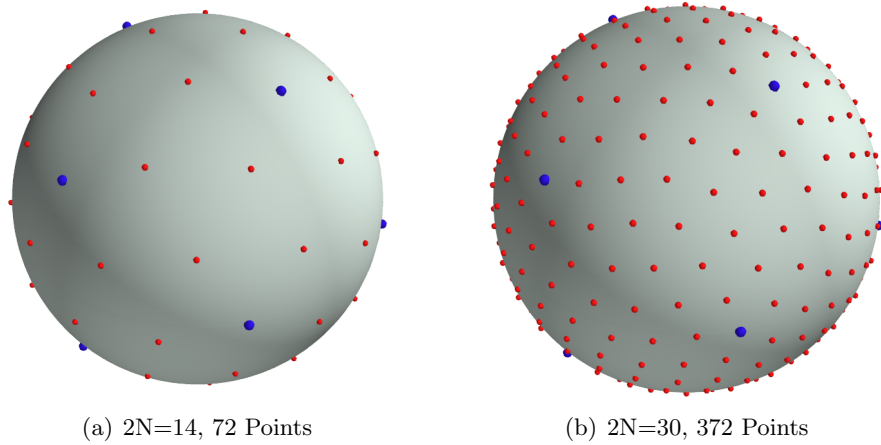
Figure 2.5: Sample quadratures for the sphere for different degree models. The blue points indicate vertices of the icosahedron, and the red points are all other quadrature nodes.

We illustrate the reproducing kernel K_N in Figure 2.6. As the degree N increases, the function tends toward the delta function on the sphere. Thus, special care must be taken when evaluating Equation 2.83 to prevent numerical error due to cancellation. Interpreting Equation 2.83 as the Christoffel-Darboux formula (see Chapter 3 of Szegö (1975)), we obtain

$$K_N(\gamma) = \frac{N+1}{4\pi} \frac{P_{N,0}(\gamma) - P_{N+1,0}(\gamma)}{1 - \gamma}, \tag{2.86}$$

and using Equation 4.5.4 of Szegö (1975), we then arrive at

$$K_N(\gamma) = \frac{N+1}{4\pi} P_N^{(1,0)}(\gamma), \tag{2.87}$$

where $P_N^{(1,0)}$ is the Jacobi polynomial with $\alpha=1$ and $\beta=0$. To simplify notation and prevent confusion of $P_N^{(1,0)}$ with the Legendre polynomials P_N, we denote

$$\bar{K}_N(\gamma) = P_N^{(1,0)}(\gamma) = \frac{4\pi}{N+1} K_N(\gamma). \tag{2.88}$$

Using the three term recurrence for Jacobi polynomials (see Equation 8.961.2 of Gradshteyn and Ryzhik (2007)), we write

$$\bar{K}_n(\gamma) = (c_1 \gamma + 1/c_0)\bar{K}_{n-1}(\gamma) - c_2 \bar{K}_{n-2}(\gamma) \tag{2.89}$$

with

$$\bar{K}_0(\gamma) = 1 \tag{2.90}$$

$$\bar{K}_1(\gamma) = \frac{3}{2}\gamma + \frac{1}{2}. \tag{2.91}$$

and

$$c_0 = (n+2)(2n+1)$$

$$c_1 = (2n+1)(2n+3)/c_0 \tag{2.92}$$

$$c_2 = n(2n+3)/c_0. \tag{2.93}$$

We use Equations 2.89 and 2.88 to compute values of the kernel $K_N(\gamma)$.
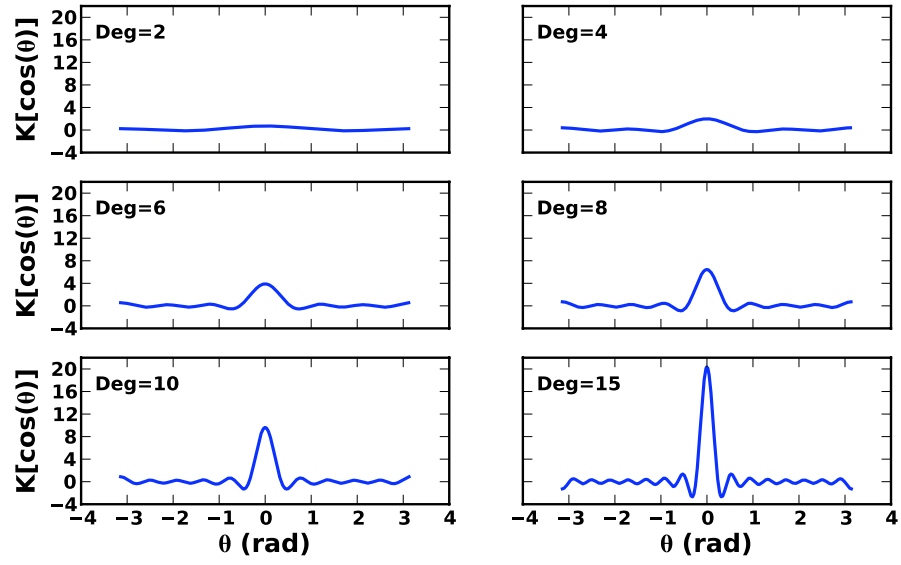
Figure 2.6: Sample plots of the reproducing kernel K_N as a function of the angle between the vectors $\boldsymbol{\alpha}$ and $\boldsymbol{\alpha}'$ for various degrees N.

2.4.2   Approximation by Gaussians

To obtain a multiresolution representation instead of Equation 2.81, following Beylkin and Monzón (2010) we replace $\rho^{-(n+1)}$ for all n by an approximation using Gaussians. Specifically, for any required precision $\epsilon > 0$, there exists a step size h and a positive M such that

$$\left| e^{-xy} - G_{\epsilon,M}(x,y) \right| \leq \epsilon \tag{2.94}$$

where

$$G_{\epsilon,M}(x,y) = \frac{hx}{\sqrt{4\pi}} \sum_{j=0}^{M} e^{-\frac{x^2}{4}e^{s_j} - y^2 e^{-s_j} + \frac{1}{2}s_j} \tag{2.95}$$

and

$$s_j = s_{start} + jh. \tag{2.96}$$

For details, we refer to Beylkin and Monzón (2010).

Since the $\rho^{-(n+1)}$ term in Equation 2.81 may be rewritten as $e^{-(n+1)\ln\rho}$, applying Equation 2.95 yields

$$
\begin{aligned}
\rho^{-(n+1)} \approx G_{\epsilon,\mathbb{Z}}(\ln\rho, n+1) &= \frac{h(n+1)}{\sqrt{4\pi}} \sum_{j\in\mathbb{Z}} e^{-(n+1)^2 e^{-jh}/4 - (\ln\rho)^2 e^{jh} - jh/2} \\
&= \frac{h(n+1)}{\sqrt{2\pi}} \sum_{j\in\mathbb{Z}} \sigma_j^{-1} e^{-(n+1)^2/(2\sigma_j^2)} e^{-(\ln\rho)^2 \sigma_j^2/2} \tag{2.97}
\end{aligned}
$$

where

$$\sigma^2 = 2e^{jh}. \tag{2.98}$$

Substituting Equation 2.97 into Equation 2.81 and reorganizing, we have

$$\tilde{U}(\rho,\phi,\theta) = \frac{\mu}{R} \sum_{j\in\mathbb{Z}} e^{-(\ln\rho)^2 \sigma_j^2/2} Z_j(\phi,\theta) \tag{2.99}$$

where

$$Z_j(\phi,\theta) = \frac{h}{\sigma_j\sqrt{2\pi}} \sum_{n=0}^{\infty} (n+1) e^{-(n+1)^2/(2\sigma_j^2)} V_n(\phi,\theta). \tag{2.100}$$

The sum in Equation 2.99 extends over all integers $\mathbb{Z}$. However, most terms are negligible, and we designate a subset $\mathbb{J}$ of $\mathbb{Z}$ as the range of indices corresponding to the terms with significant contribution. We denote the truncated version of Equation 2.99 as $\tilde{U}(\rho,\phi,\theta;\mathbb{J})$.

In Figure 2.7, we provide the error for a sample set of parameters used with the function $G_{\epsilon,\mathbb{J}}$ described by Equation 2.97. When generating $G_{\epsilon,\mathbb{J}}$, the specified accuracy ϵ determines the value h. The subset $\mathbb{J}$ is then found to meet these requirements for the given ρ. The error is uniform for all applicable n and will decrease for $\rho^{-n} < 4 \times 10^{-13}$ with n sufficiently large.
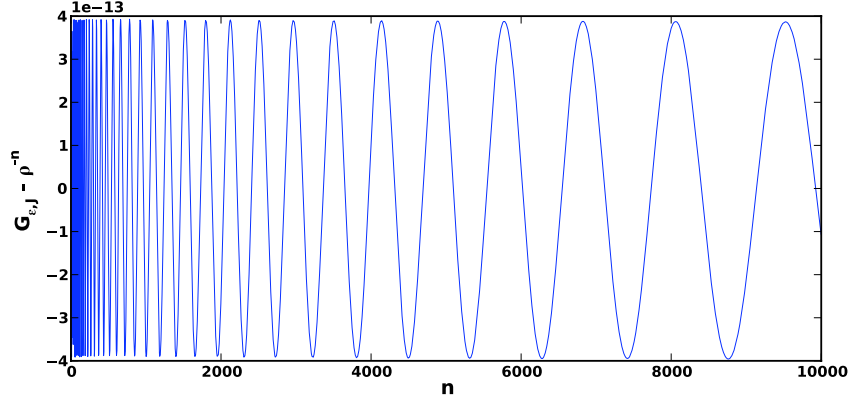
Figure 2.7: Error in $G_{\epsilon,\infty}(\approx \rho^{-n})$ up to degree n for $\rho = 1 + \frac{0.25}{6378}$, $h=1/3$, and $\mathbb{J} = \{-30, \dots, 70\}$. This figure is reproduced from Beylkin and Monzón (2010).

2.4.3 Model Description

We now combine these mathematical tools to create the MRQSphere model of the gravity potential. Substituting the coordinates ϕ and λ with the unit vector $\boldsymbol{\alpha}$, we use $\tilde{U}(\rho, \boldsymbol{\alpha}; \mathbb{J})$, and represent the terms $Z_j(\boldsymbol{\alpha})$ in Equation 2.100 using the analogue of Lagrange interpolation on the sphere, i.e. Equation 2.85. Thus, we write the MRQSphere model as

$$\tilde{U}(\rho, \boldsymbol{\alpha}; \mathbb{J}) = \frac{\mu}{R} \sum_{j \in \mathbb{J}} e^{-(\ln \rho)^2 \sigma_j^2 / 2} Z_j(\boldsymbol{\alpha}) \tag{2.101}$$

$$Z_j(\boldsymbol{\alpha}) = \sum_{i=1}^{M} K_N(\boldsymbol{\alpha} \cdot \boldsymbol{\alpha}_i) w_i Z_j(\boldsymbol{\alpha}_i) \tag{2.102}$$

In our approach we estimate functions $Z_j(\boldsymbol{\alpha})$ directly, thus avoiding any use of the spherical harmonics when evaluating the model. This Cartesian representation also eliminates any singularity at the poles when evaluating the acceleration. We note that, for a given accuracy, the exponential

cutoff in Equation 2.100 allows us to predict the degree of the subspace of spherical harmonics for the functions Z_j and, thus, choose the appropriate number of quadrature nodes for estimation. We also note that, as described in Beylkin and Monzón (2010), the number of terms in Equation (2.99) depends only weakly on the required resolution and is relatively small. For a fixed ρ, only a few terms in Equation (2.99) contribute to the potential.

Unlike the cubed-sphere gravity model, whose primary purpose is a fast evaluation of the gravity field, the MRQSphere model is intended for estimation as it attempts to minimize the number of unknown parameters. We note that the radial part of this new model may be applied to the problem of fast evaluation as well. Once estimated, the model may be converted to the cubed-sphere model, but we do not address such a conversion in this research.

Since the MRQSphere model is semi-analytic, we take the derivatives of Equations 2.85 and 2.99 to solve for the gradient, and thus the acceleration vector. We express the coordinates of the system in Cartesian coordinates where

$$\mathbf{r} = [\ x, \ y, \ z\ ]^T \tag{2.103}$$

and the angles ϕ and λ are represented by the unit vector $\hat{\mathbf{r}}$. Starting with Equation 2.99,

$$\frac{\partial \tilde{U}}{\partial \mathbf{r}} = \frac{\mu}{R} \sum_{j \in \mathbb{Z}} \left[Z_j(\hat{\mathbf{r}}) \frac{\partial}{\partial \mathbf{r}} \left(e^{-(\ln \rho)^2 \sigma_j^2 / 2} \right) + e^{-(\ln \rho)^2 \sigma_j^2 / 2} \frac{\partial Z_j(\hat{\mathbf{r}})}{\partial \mathbf{r}} \right]. \tag{2.104}$$

Solving for the first partial derivative in the right hand side with $\rho = r/R$,

$$\begin{aligned}
\frac{\partial}{\partial \mathbf{r}} \left(e^{-(\ln \rho)^2 \sigma_j^2 / 2} \right) &= -e^{-(\ln \rho)^2 \sigma_j^2 / 2} \frac{\sigma_j^2}{2} \frac{\partial (\ln \rho)^2}{\partial \mathbf{r}} \\
&= -e^{-(\ln \rho)^2 \sigma_j^2 / 2} \left(\frac{\sigma_j^2 \ln \rho}{r^2} \right) \mathbf{r}.
\end{aligned} \tag{2.105}$$

Upon differentiating $Z_j(\hat{\mathbf{r}})$ in Equation 2.102,

$$\begin{aligned}
\frac{\partial Z_j(\hat{\mathbf{r}})}{\partial \mathbf{r}} &= \frac{\partial}{\partial \mathbf{r}} \left(\sum_{l=1}^{M} K_N(\hat{\mathbf{r}} \cdot \boldsymbol{\alpha}_l) w_l f(\boldsymbol{\alpha}_l) \right) \\
&= \sum_{l=1}^{M} w_l f(\boldsymbol{\alpha}_l) \frac{\partial K_N(\hat{\mathbf{r}} \cdot \boldsymbol{\alpha}_l)}{\partial (\hat{\mathbf{r}} \cdot \boldsymbol{\alpha}_l)} \frac{\partial (\hat{\mathbf{r}}^T \boldsymbol{\alpha}_l)}{\partial \mathbf{r}} \\
&= \sum_{l=1}^{M} w_l f(\boldsymbol{\alpha}_l) \frac{\partial K_N(\gamma)}{\partial \gamma} \left(\left[\frac{\partial \hat{\mathbf{r}}}{\partial \mathbf{r}} \right]^T \boldsymbol{\alpha}_l \right)
\end{aligned} \tag{2.106}$$

where $\gamma = \hat{\mathbf{r}} \cdot \boldsymbol{\alpha}_l$. Finally, differentiating Equations 2.86, 2.89, 2.90, and 2.91 yields

$$\frac{\partial K_n(\gamma)}{\partial \gamma} = \frac{N+1}{4\pi} \frac{\partial \bar{K}_n(\gamma)}{\partial \gamma} \tag{2.107}$$

where

$$\frac{\partial \bar{K}_n(\gamma)}{\partial \gamma} = c_1 \bar{K}_{n-1}(\gamma) + \left(c_1 \gamma + \frac{1}{c_0} \right) \frac{\partial \bar{K}_{n-1}(\gamma)}{\partial \gamma} - c_2 \frac{\partial \bar{K}_{n-2}(\gamma)}{\partial \gamma} \tag{2.108}$$

with

$$\frac{\partial \bar{K}_0(\gamma)}{\partial \gamma} = 0 \tag{2.109}$$

$$\frac{\partial \bar{K}_1(\gamma)}{\partial \gamma} = \frac{3}{2}. \tag{2.110}$$

The resulting acceleration vector, with terms expressed using matrix operations, is

$$\ddot{\mathbf{r}} = \nabla \tilde{U} = \frac{\mu}{R} \sum_{j \in \mathbb{J}} e^{-(\ln \rho)^2 \sigma_j^2 / 2} \left[\left(-\frac{\sigma_j^2}{r^2} (\ln \rho) Z_j(\hat{\mathbf{r}}) \right) \mathbf{r} + \left(\frac{\partial \hat{\mathbf{r}}}{\partial \mathbf{r}} \right) \left(\sum_{l=1}^{M} w_l Z_j(\boldsymbol{\alpha}_l) \frac{\partial K_n(\gamma)}{\partial \gamma} \boldsymbol{\alpha}_l \right) \right] \tag{2.111}$$

where

$$\frac{\partial \hat{\mathbf{r}}}{\partial \mathbf{r}} = \left(\frac{\partial \hat{\mathbf{r}}}{\partial \mathbf{r}} \right)^T = \frac{1}{r} \mathbb{I}_{3 \times 3} - \frac{\mathbf{r} \mathbf{r}^T}{r^3}. \tag{2.112}$$

To facilitate future integration of the MRQSphere model with the orbit determination process, and to evaluate the Laplacian ($\nabla^2 \tilde{U}$), we solve for the Jacobian of the acceleration vector with respect to the state. This Jacobian is also the second derivative of $\tilde{U}$ with respect to the satellite position. These are often referred to as the variational equations.

We begin by solving for the second partial derivative of Equation 2.99,

$$\frac{\partial^2 \tilde{U}}{\partial \mathbf{r}^2} = \frac{\mu}{R} \sum_{j \in \mathbb{Z}} \left[Z_j(\hat{\mathbf{r}}) \frac{\partial^2}{\partial \mathbf{r}^2} \left(e^{-(\ln \rho)^2 \sigma_j^2 / 2} \right) \right.$$
$$+ 2 \frac{\partial}{\partial \mathbf{r}} \left(e^{-(\ln \rho)^2 \sigma_j^2 / 2} \right) \left(\frac{\partial Z_j(\hat{\mathbf{r}})}{\partial \mathbf{r}} \right)^T$$
$$\left. + e^{-(\ln \rho)^2 \sigma_j^2 / 2} \frac{\partial^2 Z_j(\hat{\mathbf{r}})}{\partial \mathbf{r}^2} \right]. \tag{2.113}$$

The first derivatives were previously provided in Equations 2.105 and 2.106. After taking the second derivative of the exponential,

$$\frac{\partial^2}{\partial \mathbf{r}^2} e^{-(\ln \rho)^2 \sigma_j^2 / 2} = \frac{\sigma_j^2}{r^2} e^{-(\ln \rho)^2 \sigma_j^2 / 2} \left(\frac{2 \ln \rho + \sigma_j^2 (\ln \rho)^2 - 1}{r^2} \mathbf{r} \mathbf{r}^T - (\ln \rho) \mathbb{I}_{3 \times 3} \right). \tag{2.114}$$

The derivative of Equation 2.106 is then

$$\frac{\partial^2 Z_j(\hat{\mathbf{r}})}{\partial \mathbf{r}^2} = \sum_{l=1}^{M} w_l Z_j(\boldsymbol{\alpha}_l) \left(\frac{\partial K_n(\gamma)}{\partial \gamma} \begin{bmatrix} \boldsymbol{\alpha}_l^T \frac{\partial}{\partial \mathbf{r}} \left(\frac{\partial \hat{\mathbf{r}}}{\partial x} \right) \\ \boldsymbol{\alpha}_l^T \frac{\partial}{\partial \mathbf{r}} \left(\frac{\partial \hat{\mathbf{r}}}{\partial y} \right) \\ \boldsymbol{\alpha}_l^T \frac{\partial}{\partial \mathbf{r}} \left(\frac{\partial \hat{\mathbf{r}}}{\partial z} \right) \end{bmatrix} + \frac{\partial^2 K_n(\gamma)}{\partial \gamma^2} \left[\frac{\partial \hat{\mathbf{r}}}{\partial \mathbf{r}} \boldsymbol{\alpha}_l \right] \left[\frac{\partial \hat{\mathbf{r}}}{\partial \mathbf{r}} \boldsymbol{\alpha}_l \right]^T \right) \quad (2.115)$$

where

$$\frac{\partial^2 K_n(\gamma)}{\partial \gamma^2} = \frac{N+1}{4\pi} \frac{\partial^2 \bar{K}_n(\gamma)}{\partial \gamma^2}, \quad (2.116)$$

$$\frac{\partial^2 \bar{K}_n(\gamma)}{\partial \gamma^2} = 2c_1 \frac{\partial \bar{K}_{n-1}(\gamma)}{\partial \gamma} + \left(c_1 \gamma + \frac{1}{c_0} \right) \frac{\partial^2 \bar{K}_{n-1}(\gamma)}{\partial \gamma^2} - c_2 \frac{\partial^2 \bar{K}_{n-2}(\gamma)}{\partial \gamma^2}, \quad (2.117)$$

and

$$\frac{\partial^2 \bar{K}_0(\gamma)}{\partial \gamma^2} = \frac{\partial^2 \bar{K}_1(\gamma)}{\partial \gamma^2} = 0. \quad (2.118)$$

The $\partial \hat{\mathbf{r}}/\partial x$, $\partial \hat{\mathbf{r}}/\partial y$, and $\partial \hat{\mathbf{r}}/\partial z$ terms refer to the first, second, and third column, respectively, of the matrix provided by Equation 2.112. Thus, we have the variational equations, expressed in a slightly more compact form,

$$\frac{\partial^2 \tilde{U}}{\partial \mathbf{r}^2} = \frac{\mu}{R} \sum_{j \in \mathbb{Z}} e^{-(\ln \rho)^2 \sigma_j^2 / 2} \left\{ \frac{\sigma_j^2}{r^2} \left(\frac{2 \ln \rho + \sigma_j^2 (\ln \rho)^2 - 1}{r^2} \mathbf{r} \mathbf{r}^T - (\ln \rho) \mathbb{I}_{3 \times 3} \right) \right.$$
$$\left. - \left(\frac{2\sigma_j^2 \ln \rho}{r^2} \right) \mathbf{r} \left(\frac{\partial Z_j(\hat{\mathbf{r}})}{\partial \mathbf{r}} \right)^T + \frac{\partial^2 Z_j(\hat{\mathbf{r}})}{\partial \mathbf{r}^2} \right\}. \quad (2.119)$$

The sum of the diagonal elements of this matrix yields the Laplacian $\nabla^2 \tilde{U}$ of the model. Since $\tilde{U}$ is an approximation, $\nabla^2 \tilde{U} = 0$ for the MRQSphere model is not identically zero. However, since we control the precision, the error may be made arbitrarily small. We compute the Laplacian for the MRQSphere model in Section 7.1.1 and show that the error is small and corresponds to the original choice of ϵ, the required precision, in the construction of the model.

Chapter 3

Estimation Methods

In this chapter, we present several estimation techniques with applications to the orbit determination problem. We do not provide a full derivation of these tools, or a detailed explanation of their uses or implementation. We only provide the details required for future discussion. More detailed descriptions of the orbit determination process may be found in Tapley et al. (2004b) and Crassidis and Junkins (2004). The first section discusses some preliminary mathematics, most notably the linearization of the observation and satellite dynamics models. The second section presents the basics of least squares estimation. Finally, we provide a brief treatment of two nonlinear estimation techniques.

3.1   Preliminaries

The orbit determination process seeks to provide an accurate estimate of a satellite's state, any other set of parameters that may affect the motion of the satellite, or any variables affecting the observation of said motion. These parameters comprise the estimated state vector $\mathbf{X}$. We use the notation $\bar{\mathbf{X}}$ and $\hat{\mathbf{X}}$ to indicate a priori knowledge and the filter estimated state, respectively. The orbit determination process is usually performed using observations to estimate: (1) a state at a single point in time or (2) estimate the state when observations are available. The selection of each technique varies with the specific application.

We wish to estimate the vector $\mathbf{X}$, of length n, based on a collection of p observations $\mathbf{Y}_i$ at time t_i. Observations may be gathered over l epochs, yielding $m = l \times p$ total observations. We

assume the system dynamics may be described by

$$\dot{\mathbf{X}} = F(\mathbf{X}, t) \tag{3.1}$$

$$\mathbf{X}(t_\circ) \equiv \mathbf{X}_\circ \tag{3.2}$$

and the observations at time t_i are related to the estimated state by

$$\mathbf{Y}_i = G(\mathbf{X}_i, t_i) + \boldsymbol{\epsilon}_i, \qquad i = 1, 2, \dots, l. \tag{3.3}$$

The $\boldsymbol{\epsilon}_i$ describe the observation modeling errors at t_i.

When using many estimation techniques, the nonlinear orbital dynamics require a lineariza-tion about a reference solution $\mathbf{X}^*$. We may propagate the reference solution to any point in time based on an initial condition $\bar{\mathbf{X}}_\circ^*$ and the system dynamics, i.e. Equation 3.1. In linearizing the problem, we derive a deviation from the reference trajectory

$$\mathbf{x} = \mathbf{X} - \mathbf{X}^*, \tag{3.4}$$

i.e. the difference between the true solution and the reference trajectory. We note that a lower-case letter signifies a deviation vector. The variations in time of the deviation vector, to first order, are then

$$\dot{\mathbf{x}} = A(t)\mathbf{x} \tag{3.5}$$

where

$$A(t) = \left[\frac{\partial F(t_i)}{\partial \mathbf{X}(t_i)} \right]^* . \tag{3.6}$$

The notation $[]^*$ indicates evaluation using the reference trajectory at the appropriate time. The solution to Equation 3.5 may be expressed as

$$\mathbf{x}_k = \Phi(t_k, t_i)\mathbf{x}_i \tag{3.7}$$

where

$$\dot{\Phi}(t_k, t_i) = A(t_k)\Phi(t_k, t_i) \tag{3.8}$$

$$\dot{\Phi}(t_i, t_i) = I_{n \times n}. \tag{3.9}$$

We refer to $\Phi(t_k, t_i)$ as the state transition matrix, which maps a deviation vector from t_i to t_k. Similarly, we use deviations in the observations

$$\mathbf{y}_i = \mathbf{Y}_i - G(\mathbf{X}_i^*, t_i), \tag{3.10}$$

with $\mathbf{x}$ related to $\mathbf{y}$ by

$$\mathbf{y}_i = \tilde{H}(t_i)\mathbf{x}_i + \epsilon_i \tag{3.11}$$

and

$$\tilde{H}(t_i) = \left[\frac{\partial G(t_i)}{\partial \mathbf{X}(t_i)}\right]^*. \tag{3.12}$$

We may also relate $\mathbf{x}_\circ$, the deviation vector at time $t_\circ$, to all observations at all times by

$$\mathbf{y} = \begin{bmatrix} \mathbf{y}_1 \\ \mathbf{y}_2 \\ \vdots \\ \mathbf{y}_l \end{bmatrix} = H\mathbf{x}_\circ + \epsilon \tag{3.13}$$

where

$$H = \begin{bmatrix} \tilde{H}(t_1)\Phi(t_1, t_0) \\ \tilde{H}(t_2)\Phi(t_2, t_0) \\ \vdots \\ \tilde{H}(t_l)\Phi(t_l, t_0) \end{bmatrix}, \qquad \epsilon = \begin{bmatrix} \epsilon_1 \\ \epsilon_2 \\ \vdots \\ \epsilon_l \end{bmatrix}. \tag{3.14}$$

Most orbit determination techniques seek to estimate the deviation vector $\mathbf{x}$ using the deviations in the observations $\mathbf{y}$ based on a reference trajectory $\mathbf{X}^*$. We may then add this deviation vector to the reference trajectory to generate an updated estimated state vector.

3.2   Least Squares Estimation

For an unknown vector $\mathbf{x}$ with n elements, we may relate them to a vector of m observations $\mathbf{y}$ by

$$\mathbf{y} = H\mathbf{x} + \epsilon. \tag{3.15}$$

The least squares estimator selects the value of $\mathbf{x}$ that minimizes the sum of the squares of the terms in $\boldsymbol{\epsilon}$, i.e. it minimizes

$$J(\mathbf{x}) = \frac{\boldsymbol{\epsilon}^T \boldsymbol{\epsilon}}{2}. \tag{3.16}$$

The 1/2 scale factor simplifies derivations of the various solutions of least squares estimation. In the following sections, we describe two solutions of the least squares problem. For a comprehensive discussion of least squares estimation, see Lawson and Hanson (1974).

3.2.1   Solution via Normal Equations

In the case of an overdetermined problem $(m > n)$, we cannot simply solve the linear system $H\mathbf{x} = \mathbf{y}$. Writing the normal equation solution to the least squares problem

$$\left(H^T H\right) \hat{\mathbf{x}} = H^T \mathbf{y}, \tag{3.17}$$

we note that we have a new linear system with a mapping matrix $H^T H$ and observations $H^T \mathbf{y}$. This solution assumes H is of rank n and $E[\boldsymbol{\epsilon}\boldsymbol{\epsilon}^T] = I_{m \times m}$. The product $H^T H$ effectively squares the condition number of the matrix H. For any linear system $A\mathbf{x} = \mathbf{y}$, the condition number of A describes the size of changes to the solution $\mathbf{x}$ with changes in observations $\mathbf{y}$. If the observations are highly correlated, H has a large condition number, and, thus, Equation 3.17 may yield an inaccurate solution. Additionally, if H is not of rank n, then $H^T H$ is non-singular and we cannot evaluate $(H^T H)^{-1}$ to solve for $\hat{\mathbf{x}}$.

If a priori information is available, i.e. an initial estimate $\bar{\mathbf{x}}_\circ$ with an associated state-error covariance matrix $P_\circ$, and a measurement-error covariance matrix $R = E[\boldsymbol{\epsilon}\boldsymbol{\epsilon}^T]$, we may use the weighted-least-squares normal equation

$$\left(H^T R^{-1} H + \bar{P}_\circ^{-1}\right) \hat{\mathbf{x}}_\circ = \left(H^T R^{-1} \mathbf{y} + \bar{P}_\circ^{-1} \bar{\mathbf{x}}_\circ\right). \tag{3.18}$$

The state-error covariance matrix $P = E[(\hat{\mathbf{x}} - \mathbf{x})(\hat{\mathbf{x}} - \mathbf{x})^T]$ provides an estimate of the statistical error in the estimate $\hat{\mathbf{x}}$. For the solution of Equation 3.18, we solve for the state-error covariance matrix via

$$P_\circ = \left(H^T R^{-1} H + \bar{P}_\circ^{-1}\right)^{-1}. \tag{3.19}$$

If the condition number of H is large, the condition number for $H^T R^{-1} H + \bar{P}_\circ^{-1}$ may also be large.

Practical applications of these least squares solvers, especially systems requiring linearization, use iteration to converge on an estimated state. In theory, each iteration reduces $|\hat{\mathbf{x}}|$, thereby bringing the estimated state closer to the true state. More details on this process may be found in Tapley et al. (2004b).

3.2.2   Singular Value Decomposition Methods

If the rank of H is less than n, or the condition number is sufficiently large, then Equations 3.17 and 3.18 may not provide an adequate estimate for $\mathbf{x}$. In these cases, we use the singular value decomposition (SVD), writing

$$H = USV^T \tag{3.20}$$

where both U and V are unitary matrices (i.e. $V^T V = I$), and S is a diagonal matrix with singular values. Explicitly indicating zero singular values, we write

$$S = \begin{bmatrix} S' & 0 \\ 0 & 0 \end{bmatrix} \tag{3.21}$$

where the $r \times r$ matrix S' contains the non-zero singular values and r is the numeric rank of H. We assume that singular values below a certain threshold are set equal to zero. The pseudoinverse of H is calculated using the SVD, and solutions of Equation 3.15 may be expressed as

$$\hat{\mathbf{x}} = V \begin{bmatrix} S'^{-1} & 0 \\ 0 & 0 \end{bmatrix} U^T \mathbf{y}. \tag{3.22}$$

For the weighted least squares using SVD, the solution is written as

$$\hat{\mathbf{x}} = V \begin{bmatrix} S'^{-1} & 0 \\ 0 & 0 \end{bmatrix} U^T B \mathbf{y}, \tag{3.23}$$

where

$$BH = V^T S U \tag{3.24}$$

and

$$R^{-1} = BB. \tag{3.25}$$

We note that using the SVD solution of least squares estimation is not commonplace in orbit determination, but some applications exist (Boikov et al., 2007; Marshall, 1999; Ahn, 1996; Hinga, 2004).

The state-error covariance matrix, $P = E[(\hat{\mathbf{x}} - \mathbf{x})(\hat{\mathbf{x}} - \mathbf{x})^T]$, where $\mathbf{x}$ is the true value, provides some statistical information on the quality of the solution $\hat{\mathbf{x}}$. In the case of least squares estimation with SVD,

$$
\begin{aligned}
E[(\hat{\mathbf{x}} - \mathbf{x})(\hat{\mathbf{x}} - \mathbf{x})^T] &= E\left[\left(V \begin{bmatrix} S'^{-1} & 0 \\ 0 & 0 \end{bmatrix} U^T B\mathbf{y} - \mathbf{x}\right)\left(V \begin{bmatrix} S'^{-1} & 0 \\ 0 & 0 \end{bmatrix} U^T B\mathbf{y} - \mathbf{x}\right)^T\right] \\
&= E\left[V \begin{bmatrix} S'^{-1} & 0 \\ 0 & 0 \end{bmatrix} UB\left(\mathbf{y} - H\mathbf{x}\right)\left(\mathbf{y} - H\mathbf{x}\right)^T B^T U^T \begin{bmatrix} S'^{-1} & 0 \\ 0 & 0 \end{bmatrix} V^T\right] \\
&= V \begin{bmatrix} S'^{-1} & 0 \\ 0 & 0 \end{bmatrix} UBE\left[\epsilon\epsilon^T\right] B^T U^T \begin{bmatrix} S'^{-1} & 0 \\ 0 & 0 \end{bmatrix} V^T \\
&= V \begin{bmatrix} S'^{-2} & 0 \\ 0 & 0 \end{bmatrix} V^T \tag{3.26}
\end{aligned}
$$

3.3 Non-Linear Filters

The least squares estimator presented in the previous section uses a linearized approximation of the system to provide an estimate of $\mathbf{X}$. In this section, we discuss methods that include some higher-order effects: the extended and unscented Kalman filters.

3.3.1 Extended Kalman Filter

The extended Kalman filter (EKF) is a slight modification of the conventional Kalman filter (CKF). The CKF is a sequential filter; a class of filters that generate an estimated state as each

observation becomes available. Hence, the CKF, or some variant thereof, may provide a real-time estimate of the satellite state. In the CKF, we propagate the reference trajectory $\mathbf{X}^*$ without any updates between observations. The EKF algorithm updates the reference trajectory after each measurement update. We will only discuss the EKF, and refer the reader to Tapley et al. (2004b) for more information on the CKF.

The first step in the EKF is to perform a time update of the state-error covariance matrix. Given an estimate of the state $\hat{\mathbf{X}}_\circ$ at time $t_\circ$, we propagate the state forward in time using $F(\mathbf{X}, t)$ to time t_i. We designate this newly updated state as $\bar{\mathbf{X}}_i$. The time t_i corresponds to the time of the next observation $\mathbf{Y}_i$. We then map $P_\circ$ forward in time using

$$\bar{P}_i = \Phi(t_i, t_\circ) P_\circ \Phi^T(t_i, t_\circ) + Q \tag{3.27}$$

where Q is a process noise matrix to account for errors in the state dynamics model. Upon evaluating the state-to-observation mapping matrix in Equation 3.12 with $\bar{\mathbf{X}}_i$ at t_i, we solve for the Kalman gain

$$K = \bar{P}_i \tilde{H}^T \left(\tilde{H} \bar{P}_i \tilde{H}^T + R \right)^{-1}. \tag{3.28}$$

Using the observation deviation vector

$$\mathbf{y} = \mathbf{Y}_i - G(\bar{\mathbf{X}}_i, t_i), \tag{3.29}$$

we generate the estimated state and state-error covariance matrix

$$\hat{\mathbf{X}}_i = \bar{\mathbf{X}}_i + K\mathbf{y} \tag{3.30}$$

$$P_i = \left(I_{n \times n} - K\tilde{H} \right) \bar{P}_i. \tag{3.31}$$

This procedure continues for each observation $\mathbf{Y}_i$ at time t_i.

Although considered a nonlinear filter, the EKF relies on a linearized formulation of the system dynamics and observation-state relationships. This is most notable in the method used to map the state-error covariance matrix forward in time, thus only providing a first order propagation.

3.3.2   Unscented Kalman Filter

Instead of propagating P via the state-transition matrix, the unscented Kalman filter (UKF) uses the unscented transformation. Based on the covariance matrix and the estimated state, the unscented transformation generates a collection of σ-points $\mathcal{X}_j$ where the j signifies one of the $2n+1$ points. Each of these points are propagated forward in time using $F(\mathcal{X}_j, t)$, and recombined to create a time updated $\bar{\mathbf{X}}_{i+1}$ and $\bar{P}_{i+1}$. This filter does not require a linearized system, thus it approximates the state instead of a deviation vector. In this section, we describe the UKF algorithm. Further details may be found in Julier and Uhlmann (1997) and Julier (2002). The formulation presented here uses that of Van der Merwe and Wan (2001).

We start with a priori knowledge of the filter state $\hat{\mathbf{X}}_i$ and covariance matrix P_i with n estimated parameters, as well as the measurement-error covariance matrix R. After selecting a value for the parameter α such that $10^{-4} \le \alpha \le 1$, we generate the weights

$$W_{\circ}^m \;=\; \lambda/(n+\lambda) \tag{3.32}$$

$$W_{\circ}^c \;=\; W_{\circ}^m + (3 - \alpha^2) \tag{3.33}$$

$$W_i^m = W_i^c \;=\; 1/(2(n+\lambda)), \qquad i = 1, \ldots, 2n \tag{3.34}$$

where

$$\lambda = 3\alpha^2 - n. \tag{3.35}$$

The scale factor α determines the distance from the mean of the σ-points. We use $\alpha = 1.0$, which yields 3σ distances from the estimated state. Additionally, we define the unscented transformation scale factor by

$$\gamma = \sqrt{n+\lambda}. \tag{3.36}$$

The UKF time update uses the unscented transformation to generate a propagated state-covariance matrix $\bar{P}_{i+1}$. Starting with $\hat{\mathbf{X}}_i$ and P_i at t_i, we generate the σ-points

$$\mathcal{X}_{\circ,i} = \hat{\mathbf{X}}_i, \qquad \mathcal{X}_{j,i} = \hat{\mathbf{X}}_i + \gamma A_j, \qquad \mathcal{X}_{j+n,i} = \hat{\mathbf{X}}_i - \gamma A_j, \qquad j = 1 \ldots, n, \tag{3.37}$$

where A_j is the j-th column of the Cholesky decomposition A of P, i.e. $P = AA^T$. We then propagate each point forward using $F(\mathcal{X}_{j,i}, t_i)$ for $j = 0, \ldots, 2n$ to generate the σ-points $\mathcal{X}_{j,i+1}$ at t_{i+1}. Finally, we combine the propagated σ-points to generate the time updated state and covariance matrix

$$\bar{\mathbf{X}}_{i+1} = \sum_{j=0}^{2n} W_j^m \mathcal{X}_{j,i+1} \tag{3.38}$$

$$\bar{P}_{i+1} = Q + \sum_{j=0}^{2n} W_j^c \left(\mathcal{X}_{j,i+1} - \bar{\mathbf{X}}_{i+1} \right) \left(\mathcal{X}_{j,i+1} - \bar{\mathbf{X}}_{i+1} \right)^T \tag{3.39}$$

where Q is a process noise matrix.

The measurement update uses time-updated σ-points to generate a mean observation, and corrects the a priori state based on differences between the mean and observed observation. First, we compute new σ-points $\bar{\mathcal{X}}_{j,i+1}$ using Equation 3.37 with $\bar{\mathbf{X}}_{i+1}$ and $\bar{P}_{i+1}$. Unlike the propagated σ-points, these new points incorporate Q. For each σ-point vector, we compute an observation

$$\mathcal{Y}_j = G \left(\bar{\mathcal{X}}_{j,i+1}, t_{i+1} \right) \tag{3.40}$$

with a mean observation

$$\bar{\mathbf{Y}} = \sum_{j=0}^{2n} W_j^m \mathcal{Y}_j. \tag{3.41}$$

After solving for the innovation and cross-correlation covariance matrices

$$P_{yy} = R + \sum_{j=0}^{2n} W_j^c \left(\mathcal{Y}_j - \bar{\mathbf{Y}} \right) \left(\mathcal{Y}_j - \bar{\mathbf{Y}} \right)^T \tag{3.42}$$

$$P_{xy} = \sum_{j=0}^{2n} W_j^c \left(\mathcal{X}_{j,i+1} - \bar{\mathbf{X}}_{i+1} \right) \left(\mathcal{Y}_j - \bar{\mathbf{Y}} \right)^T, \tag{3.43}$$

we perform the measurement update

$$K = P_{xy} P_{yy}^{-1} \tag{3.44}$$

$$\hat{\mathbf{X}}_{i+1} = \bar{\mathbf{X}}_{i+1} + K \left(\mathbf{Y} - \bar{\mathbf{Y}} \right) \tag{3.45}$$

$$P_{i+1} = \bar{P}_{i+1} - K P_{yy} K^T \tag{3.46}$$

where $\mathbf{Y}$ is the vector of observations. Beginning with Equation 3.37, we then repeat this process for observations at t_{i+2} with initial estimates $\hat{\mathbf{X}}_{i+1}$ and P_{i+1}.

As illustrated in the algorithm, the UKF does not require the evaluation of the Jacobian of the state dynamics, i.e. the $A(t)$ matrix. No state-transition matrix is generated, thus we do not depend on a linear approximation of the state dynamics to propagate the state-error covariance matrix. The unscented transformation includes second order effects, and third order effects for Gaussian distributions (Van der Merwe and Wan, 2001). With no linearization of the system required, this classifies as a nonlinear filter.

Chapter 4

Configuring the Cubed-Sphere and MRQSphere Models

This chapter describes the techniques employed to configure the cubed-sphere and MRQ-Sphere gravity models. As described in Chapter 2, both of these models require an approximation scheme determined by the target accuracy (or precision). The user must select a model configuration, i.e. approximation scheme, to meet a specific accuracy, measurement, and/or speed requirement. This chapter discusses the trades one must consider when designing these models, and describes the methods employed in this research. This chapter begins with a description of the elements considered when configuring the cubed-sphere model, along with methods used for recent studies. A similar discussion of the MRQSphere model then follows.

4.1   Cubed-Sphere Model Configuration

The principal configuration parameters for the cubed-sphere model include: the base gravity model, the degree of the B-spline interpolation, the Chebyshev interpolation degree, the grid size, and the number of primary shells. Selection of these parameters is driven by the required evaluation speed, model precision (when compared to the base model), and file size. In principle, any two of these properties may be optimized, which causes a reduction in the third element.

The file size, specifically the number of B-spline interpolation coefficients stored in the model, is determined by

$$\textit{Number of coefficients} = 6P(l+1)(M-1)\left(\frac{N}{4}+m\right)^2, \qquad (4.1)$$

where P is the number of parameters in the model, l is the degree of the Chebyshev interpolation, M is the number of primary shells, N is the number of grid points per $360°$, and m is the degree of the B-spline interpolation. Upon inspection, the number of elements increases quadratically with N and m, thus the grid size and B-spline degree are the largest factors in file size. An increase in the density of the Chebyshev or B-spline interpolation nodes increases M or N, respectively. Small changes in l and M yield relatively large changes in the file size, and, thus, cannot be ignored.

The degree of the B-spline and Chebyshev interpolants determine the speed of the model. Although evaluation time may be lowered through implementation, there is a limit to such improvements. A reduction in degree always yields a decrease in the number of and computation time for the interpolation basis function evaluation. Unfortunately, lower degree interpolation schemes also increase error, thus improved evaluation time adversely impacts accuracy. Interpolation data node density may be increased to maintain accuracy, which results in increased memory requirements.

An increase in the density of interpolation nodes or the degree of interpolation improves accuracy, which reduces either the execution or memory efficiency of the model. Conversely, reducing the density of the nodes or the interpolation degree reduces accuracy. Thus, all three elements are inversely related and have opposite effects on the model.

4.1.1   Spherical Harmonic Base Model Selection

As discussed in Chapter 2, we derive the cubed-sphere model from a given base model. Previous versions of the cubed-sphere model, specifically those of Beylkin and Cramer (2002), used the classic formulation of the spherical harmonics, which contains a singularity at the poles. These singularities pervade to the cubed-sphere model. The core formulation of the cubed-sphere model yields no such singularities, except when present in the base model. To remove the polar singularity, we now consider the Pines and the Cartesian models as potential base models. In this section, we compare the three formulations of the spherical harmonics to assess their potential use in the cubed-sphere model.

Although the classical and the Pines model have been compared (Casotto and Fantino, 2007;

Fantino and Casotto, 2009), no comprehensive comparisons with the Cartesian model have been found. Casotto and Fantino (2007) and Fantino and Casotto (2009) demonstrate that the computational efficiency of the Pines model is less than the classical model, mainly due to the addition of the fourth partial sum associated with the radial distance. To characterize accuracy, they developed and compared two versions of each formulation: one version used double precision, while the second employed quadruple precision. In theory, numerical stability improves with quadruple precision, and a comparison between the two versions provides an approximation of the numerical stability of the double precision version of the software. The numerical performance between the formulations, using the EGM96 360×360 model (Lemoine et al., 1998), was statistically equal with roughly 14.5 digits of accuracy in acceleration. We note that double precision values are only accurate to approximately 15 digits. Unfortunately, Gottlieb (1993) only verified the Cartesian model using a small selection of low-degree analytic solutions and compared the computation times to those of the Pines model. Thompson et al. (2008) verified the accuracy of the Cartesian model using a 5×5 spherical harmonic model generated from 10 point masses. Since models become increasingly unstable with higher degrees (see, e.g., Lundberg and Schutz, 1988), these methods of verification are insufficient. In this section, we use an amalgam of the two methods to verify the Cartesian model and characterize its relative execution time.

Deprit (1979) states the formulation of the Pines model presented in Pines (1973) includes an error for computations at the poles. Additionally, it is unclear if this statement only applies to the variational equations presented in the paper. This error was possibly corrected in the presentation by Spencer (1976), but this has not been confirmed. Thus, this study of the formulations of the spherical harmonic model was further required to clarify model accuracy.

Using the point masses derived from the technique outlined in Appendix A, we define a true gravity field using a point-mass model that approximates the Earth GGM02C spherical harmonic model (Tapley et al., 2005) to degree 7. Stokes coefficients higher than degree 7 are used, but deviate from the Earth's GGM02C values. The 50 points listed in Tables A.1 and A.2 are illustrated in Figure 4.1, with larger masses represented by bigger points. The total mass of the system was

selected to yield a gravitation parameter equal to the Earth GGM02C value. From these points, we derive a 200×200 gravity model using Equations 2.49 and 2.50.
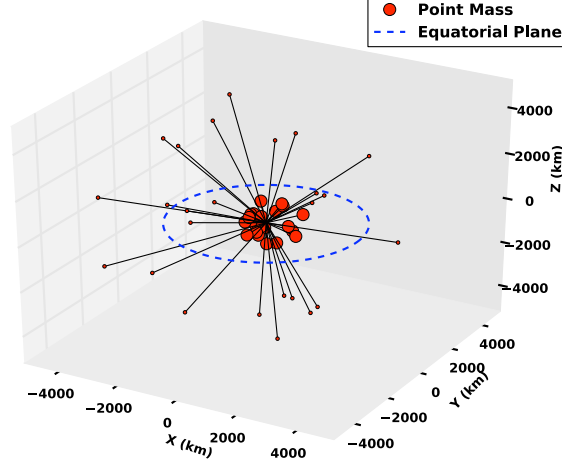
Figure 4.1: Point masses used to define a true gravity model.

We distribute test points in a $1° \times 1°$ grid at a radius of 6378.1363 km and evaluate each formulation to generate potential and acceleration vectors at each location. We then compare the true values, based on the point-mass model, to the spherical harmonic model values to assess accuracy. We define accuracy by the number of common digits (CD),

$$CD = \log_{10} \left| \frac{\alpha_t}{\alpha_e - \alpha_t} \right|, \tag{4.2}$$

where α_t is the true value and α_e is the test value.

Figure 4.2 illustrates the accuracy of the models when using a 200×200 model. The figure implies that all models are accurate to only 3-7 digits. However, since this is true for all formulations, we deem this a result of model truncation. Increasing the degree of evaluation supports this hypothesis. The agreement of the classical model at the poles is 0 (since the resulting accelerations are not a valid floating point number). The z-component accuracy of all models drops noticeably at the equator, but this component of the acceleration is relatively small. Thus, the absolute error in the Z acceleration remains small. Other than the singularities, results indicate no noticeable differences between the models. Although somewhat expected, this proves the mathematical formulations do

not result in numerical computation issues.
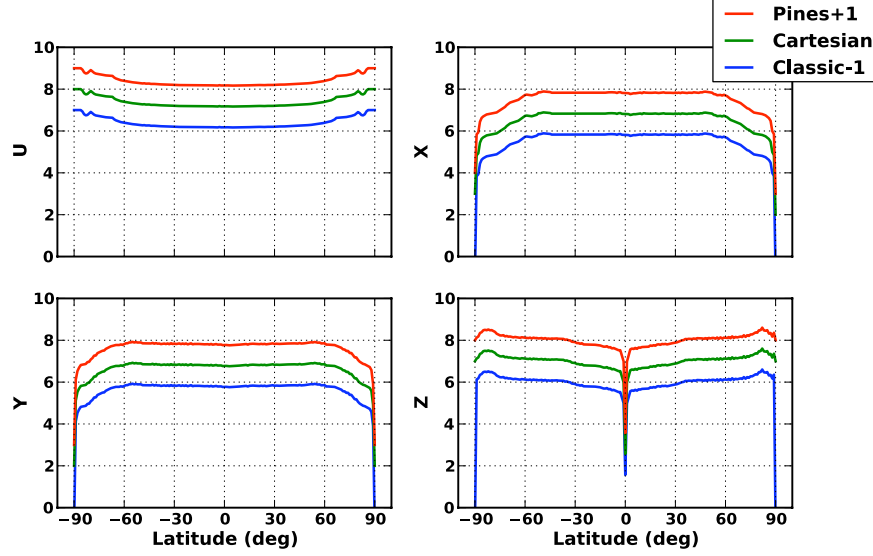
Figure 4.2: Average numerical precision of gravity potential (U) and the components of acceleration for the different formulations of the spherical harmonic model, evaluated to degree 200, when compared to the true gravity field. The Pines model and Classic model values have been offset by +1 and -1, respectively.
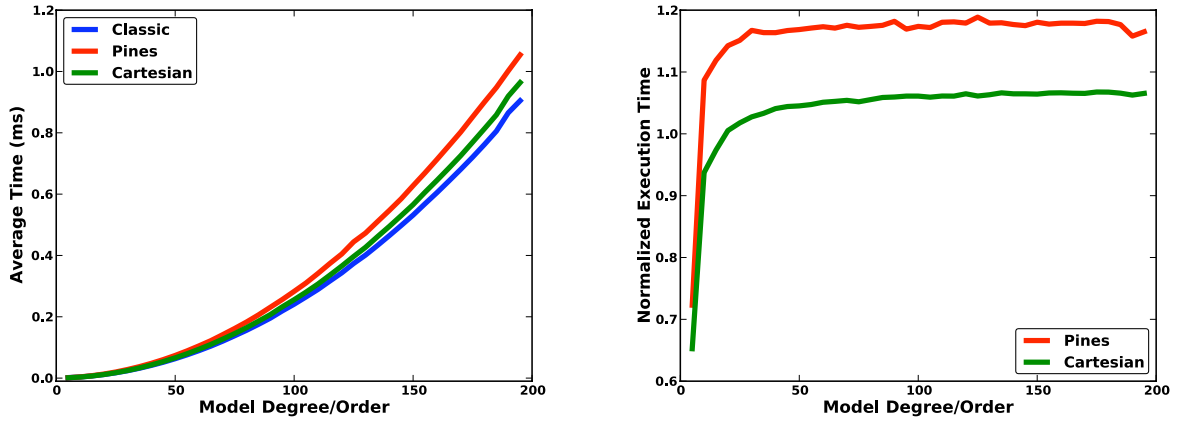
Figure 4.3: The figure on the left profiles the average execution time of the cubed sphere and the three spherical harmonic model formulations. The figure on the right demonstrates the execution time normalized by the execution time of the classic model.

We include a comparison of the average execution time, based on 10^6 evaluations, in Fig-

ure 4.3. For lower degree and order models, the classic formulation is slower than the other formulations. We believe this is due to the initial evaluation of the trigonometric functions used in the recursive formulation of $\sin(m\lambda)$ and $\cos(m\lambda)$. Both the Pines and Cartesian models are slower than the classic model for larger degree due to the addition of the fourth partial sum. The Cartesian model is faster than the Pines model because the derived Legendre functions of degree $n+1$ are not evaluated.

Based on these results, we selected the Cartesian model as the new base model for the cubed-sphere gravity model. Aside from the polar singularity, there is little difference in the accuracy of the mathematical models. Although generally less computationally efficient than the classical formulation, the Cartesian model eliminates the singularity at the poles. The additional computation burden only impacts the model generation time, which is a one-time cost for each model generated.

4.1.2   Interpolation Configuration

Beylkin and Cramer (2002) proved that the gravity field could be approximated by the cubed-sphere gravity model. No stringent precision requirements were considered, and the degree of the B-spline and Chebyshev interpolating polynomials were selected ad hoc. In the case of the grid on the surface of the cube, grid spacing equaled half the spatial resolution described by the given spherical harmonic base model to match the Nyquist sampling rate. For our purposes, we configure the model to achieve a given precision relative to the base model.

For this process, we assume an absolute precision ϵ at or above a minimum altitude r_{min}. For the Earth and Moon, one may use the gravitation parameter and the two-body acceleration to convert a relative precision, e.g. number of accurate digits, to an absolute precision for the total model. For example, assuming a target precision of D digits, we write

$$\epsilon(r) = \frac{\mu}{r^2} 10^{-D} \tag{4.3}$$

where ϵ corresponds to the target absolute precision at the radius r. The method proposed here seeks to configure the cubed-sphere model precision to less than ϵ for all $r \geq r_{min}$.

Selection of the B-spline and Chebyshev interpolation degrees, along with the associated node densities, are determined empirically to meet the precision requirements. To simplify this process, specifically to reduce the computation time associated with generating a model for testing, we construct a cubed-sphere model restricted to a subset of primary shells above and below r_{min}. We dub this a "reduced" model. This method assumes the largest model errors will be close to r_{min}, which is typically valid. Test software was developed to evaluate the model at a number of random points above r_{min}. For each point, the cubed-sphere model is compared to the base model and the absolute deviation is calculated. We then use the maximum deviation of all points to characterize the precision of the reduced model. Tests utilizing 10^5 random points prove sufficient, with any increase yielding similar results.

After testing the reduced model, we generate a full model to further assess the model precision and ensure requirements are met for all $r \geq r_{min}$. We select a set of points on the unit sphere corresponding to the regions of peak gravity variations, e.g. the Andes mountain range, and evaluate the model at each of these points for multiple $r \geq r_{min}$. We compare the precision of the acceleration vector, defined by the magnitude of the difference between the cubed-sphere- and base-model acceleration vectors, to $\epsilon(r)$. We use this comparison to profile the overall precision of the model. If this new model fails to meet precision requirements, we adjust the parameters and retest.

4.1.3   Exploration of Possible Configurations

In this section, we explore several possible configurations of the cubed-sphere model while providing an example of the configuration process. We explore the trade-offs associated with selecting the interpolation schemes and node density based on model requirements. This includes configuring and testing three models, one each that considers evaluation time, file size, and precision to be of a lower priority.

For this test, we define three properties: (1) precise, (2) small, and (3) fast. Deviations from the base model for a "precise" model are less than 8.9×10^{-15} km/s^2, while an "imprecise" model has a maximum deviation of 8.9×10^{-11} km/s^2. The latter requirement yields 1-2 digits of precision

for the portion of the gravity field described by the interpolation schemes, i.e. not represented by a low-degree spherical harmonic model, at 300 km and greater. A "small" model requires the least amount of memory to achieve the target precision. Finally, a "fast" model uses the lowest degree interpolation possible to meet the precision requirements. For reasons of computer limitations, the maximum allowed model size was 1.8 GB.

Table 4.1: Summary of the models used to explore cubed-sphere configuration trade-offs.

Model	l	m	M	N	Size (MB)	Max. Deviation (km/s^2)	Speed ($\times 10^{-6}$ s)
Fast and Small	3	5	4	104	3.2	6.8×10^{-11}	2.9
Precise and Fast	3	5	70	424	624	7.9×10^{-15}	3.1
Precise and Small	11	11	4	120	12	3.4×10^{-15}	14.5

We generate cubed-sphere models that combine two of the different properties, but at the detriment of the third. Table 4.1 describes the resulting model configurations, which we developed using the procedure outlined in the previous section. All models used a 24×24 spherical harmonic base model. We note that the 624 MB precise and fast model does not approach the 1.8 GB memory limitation. Model size will increase with increased precision requirements, but this model is sufficient for this test. The maximum deviation values provided describe the precision of the reduced model. We base the evaluation speed on an average execution time of 10^6 points.

Figures 4.4 and 4.5 describe the resulting performance of the models described by Table 4.1. Speed of evaluation improves by almost an order of magnitude with reduced degree of interpolation, while a precise and fast model requires considerably more memory. Figure 4.5 demonstrates precision requirements, which are indicated by the reference line, are met by both "precise" models. Given capabilities of modern computers, memory is, arguably, the least important of the three trade-offs for this low degree model. However, higher degree models require considerably more memory to allow for lower-degree interpolation, making them expensive. Thus, speed must be sacrificed for memory in those cases.
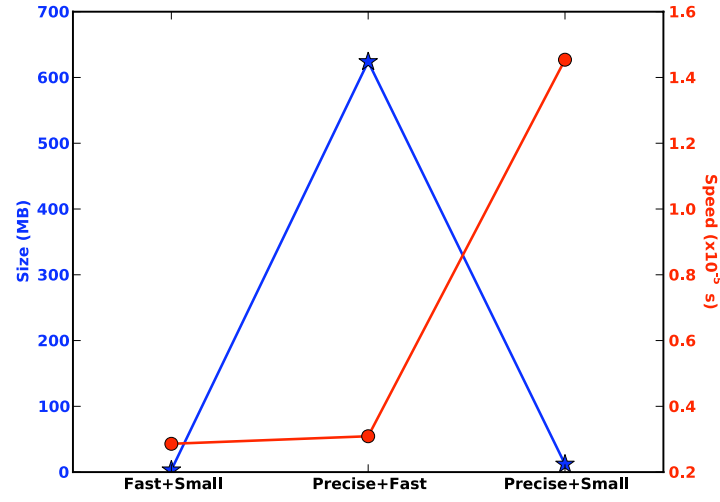
Figure 4.4: File size and average evaluation speed for the different test models.
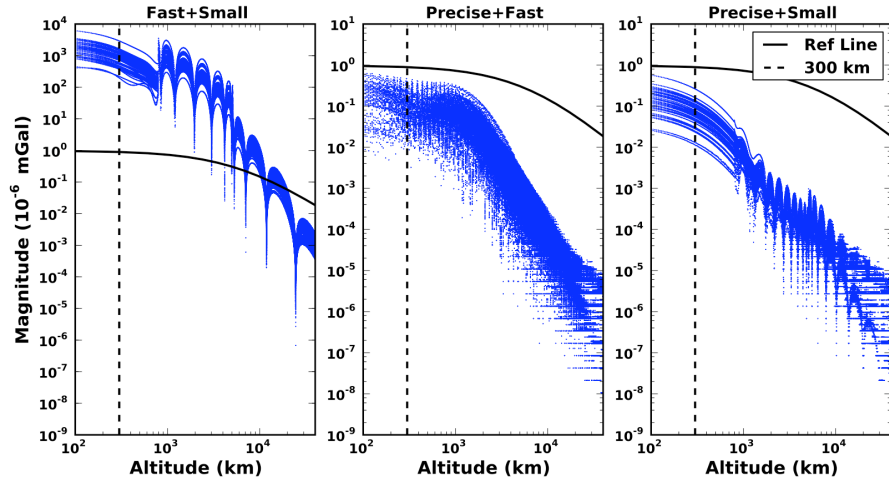
Figure 4.5: Precision of the three test models with changes in altitude.

4.2 MRQSphere Model Configuration

We now discuss the methods developed to configure the MRQSphere model for use in gravity estimation. Since we optimize the MRQSphere model for the gravity estimation problem, model size is only an issue in determining the size of the estimated state vector in the filter. We assume this is not an issue. When compared to the spherical harmonic and cubed-sphere models, the MRQSphere is inefficient for evaluation of the gravity field. Thus, we are primarily concerned with model accuracy.

We base the model accuracy on the achievable measurement accuracy for estimating the gravity field. For this reason, when discussing the MRQSphere model, we are concerned with accuracy and not precision. For a mission to an unknown celestial body, i.e. an asteroid, measurement accuracy is primarily determined by the two-way Doppler measurements gathered by Deep Space Network (DSN) tracking of the satellite. For an Earth-based mission, intersatellite range, Earth-based Doppler, satellite laser ranging (SLR), and GPS observations influence the achievable gravity measurement accuracy. We note that measurements of the gravity field are usually inferred by perturbations of the satellite motion when compared to a reference trajectory. In this section, we do not consider a single measurement type, and only discuss the general problem for configuring a model for a given accuracy.

Unknown parameters for the MRQSphere model include the Gaussian approximation step size h, the indices $\mathbb{J} \subset \mathbb{Z}$, and the degree N for each shell. We assume the node locations and weights are already determined. This assumption is valid given the method described in Ahrens and Beylkin (2009) develops nodes accurate to the limitations of double precision numbers.

We now want to further understand the affects of $\mathbb{J}$ and N_j on the MRQSphere model. In Figure 4.6, we plot the terms of the series in Equations 2.97 and 2.100 for $h = 0.5$. As seen in Figure 4.6(a), points at low altitudes are highly dependent on the shells with a larger σ_j (corresponding to larger indices j). As altitude increases, these terms decay exponentially fast, and terms with smaller σ_j dominate the sum. For example, note in Figure 4.6(a) the relative contribution of the

$j=-2$ shell at ρ values of 1 versus 10. At $\rho = 10$, this shell provides the largest single contribution to $G_{\epsilon,\mathbb{J}}$, but weakly affects the approximation at low altitudes. Thus, only a small subset of shells are required when evaluating the gravity field at high altitudes, and the selection of shells depends on user defined precision ϵ. As we may see in Figure 4.6(b), a small σ_j implies a low degree n to achieve a given accuracy, and, conversely, a large σ_j value implies a larger degree shell. Thus, as expected, low-degree models will be needed at high altitudes where terms with smaller σ_j dominate.

(a) Shell contributions ($n=2$)

(b) Shell degree contribution
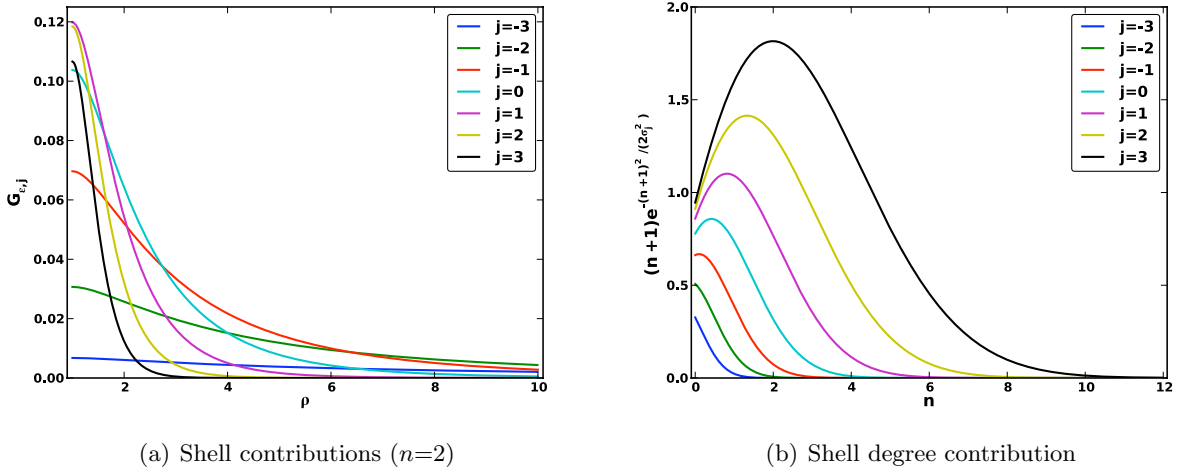
Figure 4.6: Sample Gaussians for $h = 0.5$, which illustrate the relative contribution of different parameters on the MRQSphere model. The first figure illustrates the contributions of the different shells to the function $G_{\epsilon,\mathbb{J}}$ with variations in orbit radius (in units of R). The second figure demonstrates the contribution of gravity degree n for a given shell.

Table 4.2: Data points used to determine β_1 and β_2 using a least-squares fit.

h	ϵ	h	ϵ
0.9	4.95×10^{-5}	0.5	7.65×10^{-9}
0.8	1.23×10^{-5}	0.4	5.50×10^{-11}
0.7	2.11×10^{-6}	0.3	1.64×10^{-14}
0.6	2.00×10^{-7}		

Selection of the step size h is not immediately apparent for a target accuracy ϵ, so we assume the relationship may be written as

$$h = \frac{1}{\beta_1 + \beta_2 \log \epsilon^{-1}} \tag{4.4}$$

where β_1 and β_2 are unknown constants. We derive these constants empirically using a small subset of experimentally determined values, which we provide in Table 4.2. Solving for the constants using the linear system

$$\begin{bmatrix} 1/h_1 \\ 1/h_2 \\ \vdots \\ 1/h_n \end{bmatrix} = \begin{bmatrix} 1 & \log \epsilon_1^{-1} \\ 1 & \log \epsilon_2^{-1} \\ & \vdots \\ 1 & \log \epsilon_n^{-1} \end{bmatrix} \begin{bmatrix} \beta_1 \\ \beta_2 \end{bmatrix}, \tag{4.5}$$

we arrive at

$$\beta_1 = 0.0983589778057344 \tag{4.6}$$

$$\beta_2 = 0.234434655957678. \tag{4.7}$$

We note that the relationship in Equation 4.4 is not exact, but provides a method for calculating an approximate value of h. We then make slight corrections to the approximate value to achieve a target accuracy.
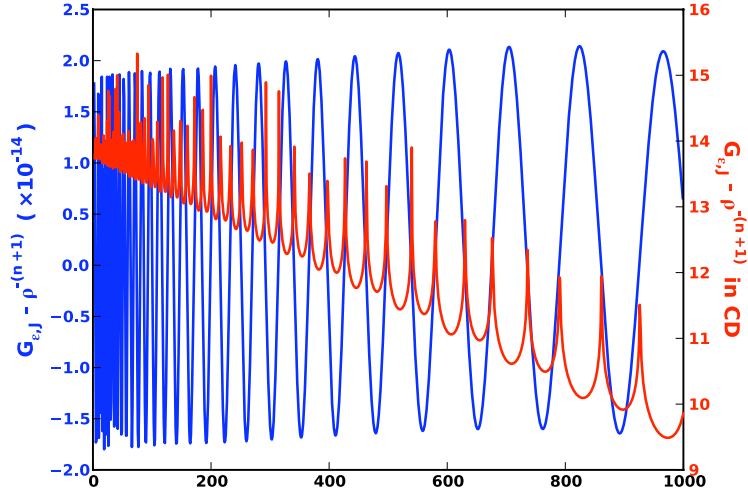
Figure 4.7: A sample configuration of the approximation $G_{\epsilon,\mathbb{J}}$ to $\rho^{-(n+1)}$ where relative accuracy, represented by CD, decays with n while the absolute accuracy ϵ remains nearly constant.

Relative accuracy of the approximation of $\rho^{-(n+1)}$ by Gaussians decreases with altitude. We

include a sample configuration in Figure 4.7 that exhibits such phenomenon. For $\rho^{-(n+1)} < \epsilon$, the absolute accuracy requirements are met while the approximation may be no longer valid. Thus, we must select a step size h to meet accuracy requirements over a range $[\rho_{min}, \rho_{max}]$ where the gravity field may be evaluated or estimated.

Before defining the configuration procedure employed for studies described in Chapter 7, we must define some notation. First, we designate ρ_k as an element of the ordered set of discrete radii $\{\rho_0, \rho_1, \ldots, \rho_{min}\}$ such that $\rho_k > \rho_{k+1}$. Additionally, we define the set $\mathbb{J}_k = \{j_{min}, j_{min} + 1, \ldots, j_{max}\}$ as the minimal set of integers such that $\left| G_{\epsilon, \mathbb{J}_k}(\rho_k, n) - \rho_k^{-(n+1)} \right| \leq \epsilon$.

We now define the procedure employed when configuring the MRQSphere model. First, we select a value of h that meets the accuracy requirements of $G_{\epsilon, \mathbb{J}}(\rho)$ at the largest ρ_{max} where the gravity model may be applied. We remind the reader that these accuracy requirements are based on achievable estimation accuracy with the available measurements of the gravity field. Assuming a set $\mathbb{J}$ such that truncation does not influence approximation accuracy, we determine an initial value of h using Equation 4.4 and then refine that value to meet accuracy requirements. With h now selected, we solve for the minimal set $\mathbb{J}_0 = \{j_{min}, j_{min} + 1, \ldots, j_{max}\}$ that meets accuracy requirements at ρ_{max}. We then determine the minimum ρ_0 such that $\left| G_{\epsilon, \mathbb{J}_0}(\rho_0, n) - \rho_0^{-(n+1)} \right| \leq \epsilon$. We now have a set $\mathbb{J}_0$ used to evaluate $G_{\epsilon, \mathbb{J}_0}(\rho, n)$ where $\rho \geq \rho_0$. Increasing j_{max} by one, $J_1 = \{j_{min}, j_{min} + 1, \ldots, j_{max} = j_{max} + 1\}$, and we then solve for ρ_1. We continue this procedure until $\rho_k \leq \rho_{min}$. The collection of sets $\mathbb{J}_k$ with corresponding radii ρ_k form a table that determines the number of terms in the function $G_{\epsilon, \mathbb{J}}(\rho, n)$. An example may be found in Table 7.2.

The final parameter that must be determined is N_j, the degree of the functions $Z_j(\alpha)$ represented using quadratures for the sphere, for each shell j. Recalling Equation 2.100 and Figure 4.6(b), terms decay exponentially with n. Thus, $Z_j(\alpha)$ varies weakly with n, and decay rates are determined by σ_j. Thus, we may limit the degree of the function represented by the quadratures.

We now develop a method for truncation while meeting a given accuracy on the sphere.

Assuming $V_n(\alpha) = 1$, we write the series in Eq. 2.100 as

$$S_N = \sum_{n=0}^{N} s_n = \sum_{n=0}^{N} (n+1)e^{-(n+1)^2/(2\sigma_j^2)}. \tag{4.8}$$

We then select a degree n for the given shell such that $|S_n - S_{n+1}| < \delta$ where δ is the required accuracy. δ may be an absolute accuracy, but, in practice, we use an accuracy relative to s_2. For example, we may write

$$\delta = s_2 10^{-D} = 3e^{-4.5/\sigma_j^2} 10^{-D} \tag{4.9}$$

where D is the number of significant digits and σ_j is the appropriate value of the given shell. We select the s_2 term because the V_0 term is described by the two-body equation while the V_1 term is zero if the origin of the coordinate system is collocated with the center of mass of the primary body. Higher degree terms (s_3, s_4, etc.) may be selected if the MRQSphere model is only required to model higher degree contributions to the gravity field.

The values of $V_n(\alpha)$ are unknown, still creating some difficulties in selecting an absolute accuracy δ for a given shell. Until the values of $Z_j(\alpha)$ are better determined, we recommend selecting a higher degree model than necessary for initial processing. After generating an initial estimate of the gravity model, $Z_j(\alpha_i)$ values may be projected onto lower degree subspaces (see Section 7.2.2). If these lower degree shells still meet accuracy requirements, the user may continue the process to determine the lowest valid degree for the quadratures on the sphere.

Chapter 5

Orbit Propagation with the Cubed-Sphere Model

In Chapter 2, we presented the cubed-sphere model for fast evaluation of the gravity field. Specifically, this model precomputes coefficients used for B-spline interpolation to evaluate the gravity field at a given point in space. In this chapter, we characterize its use for orbit propagation. This portion of the research assumes the spherical harmonics model represents the true gravity field, and our goal is to reduce orbit propagation time while minimizing any change in resulting trajectories when using the cubed-sphere model. Sections 5.1 and 5.2 were published in Jones et al. (2010b).

To assess the impact of using the cubed-sphere model, we look at differences in the propagated trajectories and the ability of the new model to adhere to mathematical constraints imposed by potential theory. In the first section, we describe the general test procedure. In the second section, we study orbit propagation improvements with cubed-sphere models designed for accuracy at the expense of computational efficiency. The third section considers faster cubed-sphere models with relaxed precision and memory requirements. Finally, we summarize the results of this chapter.

5.1   Test Description

In this section, we describe the orbit propagation methods used throughout the remainder of this chapter. This includes a brief description of software and algorithms, along with all environment parameters (e.g. Earth orientation parameters) required for evaluation. We generated all trajectories in this chapter using these methods, unless otherwise noted.

We minimized software development time by using the TurboProp orbit integration package. This software provides integration tools implemented in C, which may be used in MATLAB or Python. The cubed-sphere model, along with the necessary interface code, was implemented within the TurboProp framework. Tests requiring orbit propagation used the TurboProp Runge-Kutta 7(8) integrator (based on Fehlberg (1968)) with an integration tolerance of 10^{-12}. Further technical details on the TurboProp integrators may be found in Hill and Jones (2009).

For test orbits, we employ a variety of initial conditions, and generate states every 20 seconds over a total 24 hour propagation time span. The initial orbit altitudes span from 100 to 1,000 km at 50 km intervals. Cubed-sphere model accuracy relative to that of the spherical harmonic model decreases at lower altitudes. We provide most altitude specific results at 300 km, since most satellites orbit at or above that altitude. The right ascension of the ascending node ranged from $0°$ to $180°$ in $5°$ increments, while the inclination varied from $0°$ to $85°$ in $2.5°$ intervals. We set all other classical orbit elements to zero. The maximum inclination of $85°$ avoids the singularity at the poles in the classical formulation of the spherical harmonic model. Thus, for each altitude, we propagated 1,295 orbits. We set the Greenwich sidereal time to $0°$ at the epoch time, with an Earth rotation rate of $360°$ per solar day about the planet-fixed z-axis. We used the planetary reference radius and gravitation parameter dictated by the base model. We propagate each set of initial conditions using the cubed-sphere model and the corresponding base model, with resulting trajectories stored for future comparison.

5.2   Models Designed for Accuracy

In this section, we focus on cubed-sphere models designed for high-precision, when compared to the base model, at the expense of computation time. As will be described later, we wish to limit fluctuations in the Jacobi-like integration constant, which demonstrates the ability of the model to adhere to mathematical constraints.

5.2.1 Model Configuration

We generate cubed-sphere models corresponding to the 20×20, 70×70, and 150×150 spherical harmonic Grace Gravity Model 2, Combined (GGM02C) (Tapley et al., 2005). As mentioned previously, we are primarily concerned with maximizing orbit propagation precision, followed by minimizing the model file size. We provide the configuration of these cubed-sphere model in Table 5.1.

Table 5.1: Cubed sphere configurations used for orbit propagation tests.

Property		Value
B-spline degree (m)		11
Chebyshev polynomial degree (l)		11
Number of primary shells (M)		14
Grid Density (N) for:	CS-30 / 20x20	120
	CS-76 / 70x70	304
	CS-162 / 150x150	648

A majority of the results presented in Section 5.2 were generated before the work of Jones et al. (2010c), which includes the selection of the Cartesian model as the base model for the cubed sphere and the development of the model configuration procedure presented in Chapter 4. We first configure the cubed-sphere representation of the 150×150 model, and use these parameters, except for grid density N, for all lower degree models. We select a target relative precision of 14 digits, yielding a maximum model error of 8.9×10^{-17} km/s^2 (or 8.9×10^{-9} mGal) at 300 km. With this precision, we minimize fluctuations in the integration constant (see Section 5.2.2), which helps to ensure long-term orbit propagation accuracy. Since these models use the classical formulation of the spherical harmonics as the base model, they contain a singularity at the poles.

In Figure 5.1, we provide the variations in the gravity anomalies with height as altitude increases for 42 points on the Earth's surface. We select 30 points at random, with the remaining 12 points corresponding to regions of large absolute gravity variations. The anomalies of Figure 5.1 are referenced to the GGM02C spherical harmonic model. We indicate required precision with the ref-

erence line in each figure, which verifies the three cubed-sphere models meet precision requirements at or above 300 km for these points. As expected, peak variations in the cubed-sphere model with respect to the spherical harmonics occur at lower altitudes. Additionally, the largest anomalies occur for the higher degree models. At various altitudes, the differences become discretized due to machine precision and the relatively low contribution the gravity perturbations modeled by the cubed sphere have on the overall gravitational acceleration.
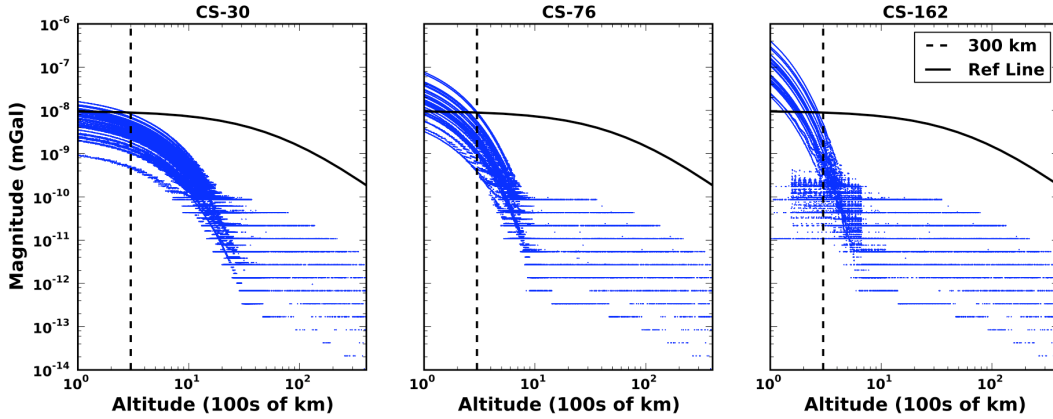
Figure 5.1: Variations in gravity anomalies with altitude for 42 points on the Earth using the CS-30, CS-76, and CS-162 models.

For the CS-162 model, there is a region below 300 km and around 10^{-10} mGal where the variations are periodic. In this case, the differences on the face of the cube are small, and, thus, are weakly affected by the grid spacing. However, approximation error still varies based on proximity to the shells used for Chebyshev interpolation. Thus, as the altitude increases at this point on the Earth's surface, the error periodically increases and decreases.

Although the results of Figure 5.1 indicate that precisions requirements have been met, we conduct a more comprehensive test at an altitude of 300 km. We visualize the gravity anomaly variations of the cubed-sphere with latitude and longitude, and represent these results as gravity anomalies projected onto the surface of the Earth. We evaluate the acceleration vector at a common altitude with latitude and longitude varied in 0.5° intervals. The magnitude of the differences in

the vector is then illustrated in Figures 5.2, 5.3, and 5.4. Like in the orbit propagation tests, acceleration vectors were not computed at the poles to avoid the singularities.
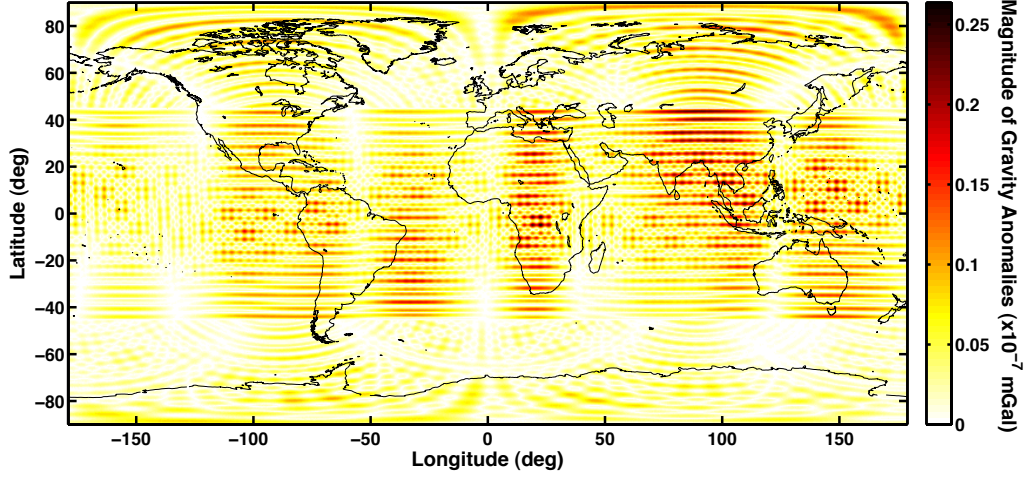
Figure 5.2: CS-30 gravity anomalies at 300 km
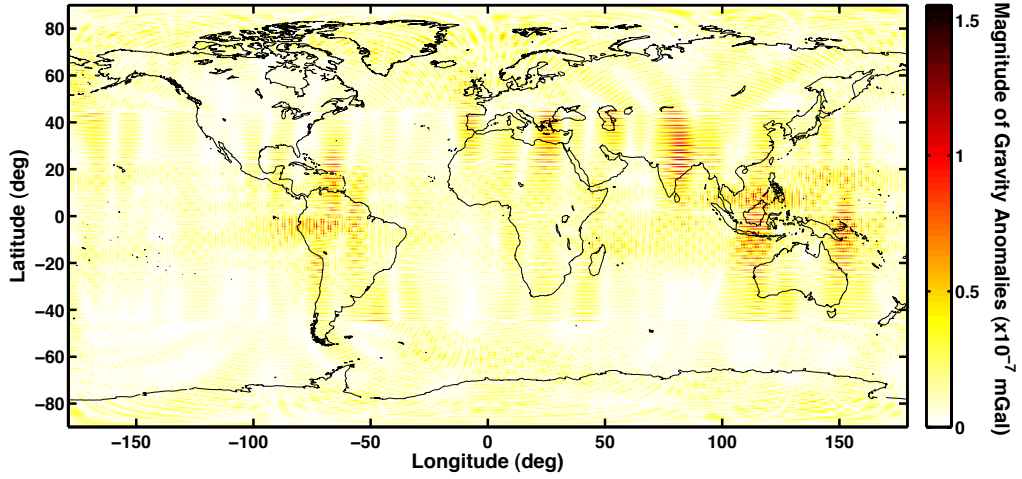
Figure 5.3: CS-76 gravity anomalies at 300 km

Fig 5.2 illustrates the gravity anomalies for the CS-30 model, and shows that anomalies are less than 10^{-7} mGal, with most below 10^{-8} mGal. The cube grid is visible, e.g. over the East Indies.

The regions of peak variation correspond to regions of high gravity fluctuations, as determined by the spherical harmonic model (e.g. the Himalayan mountain ranges and the East Indies). We note that the GGM02C gravity model is not accurate to 10^{-7} mGal (Tapley et al., 2005), and the gravity anomalies in Figures 5.2 through 5.4 are within the error of the base model.

We provide gravity anomalies for the CS-76 model in Figure 5.3. This figure indicates the average precision of the model meets the accuracy requirement of 8.9×10^{-8} mGal, however peak errors are as large at 1.6×10^{-7} mGal. The grid spacing is visible, albeit with a smaller spacing as expected with the increased node density. Regions of higher differences are more isolated than the CS-30 case, with peak anomalies near the Himalayas, Pacific rim, and South America. Magnitude of the anomalies are larger, which corresponds to the results seen in Figure 5.1, but still meet accuracy requirements.
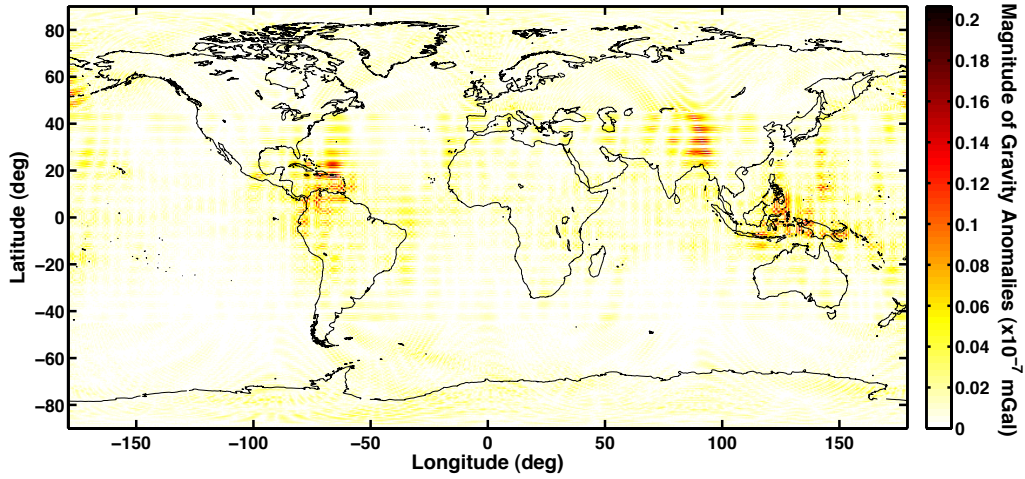
Figure 5.4: CS-162 gravity anomalies at 300 km

The gravity anomalies for the CS-162 model at 300 km are found in Figure 5.4. The model meets precision requirements and the grid spacing is still visible, but areas of peak variations are isolated to select regions. Like the previous cases, these regions correspond to those with a generally large variation in the gravity field. The largest anomaly may be found off of the coast of Haiti at approximately 18° latitude and -67° longitude.

5.2.2   Integration (Jacobi) Constant Comparisons

A given geopotential model must satisfy the Laplace equation,

$$\nabla^2 U = \frac{\partial^2 U}{\partial x^2} + \frac{\partial^2 U}{\partial y^2} + \frac{\partial^2 U}{\partial z^2} = 0. \tag{5.1}$$

Unfortunately, the direct calculation of the second derivatives within the cubed-sphere model from accelerations results in the loss of accuracy of 1-2 digits. To avoid such a loss of accuracy, values of the derivatives may be added to the model based on the variational equations of the spherical harmonic model.
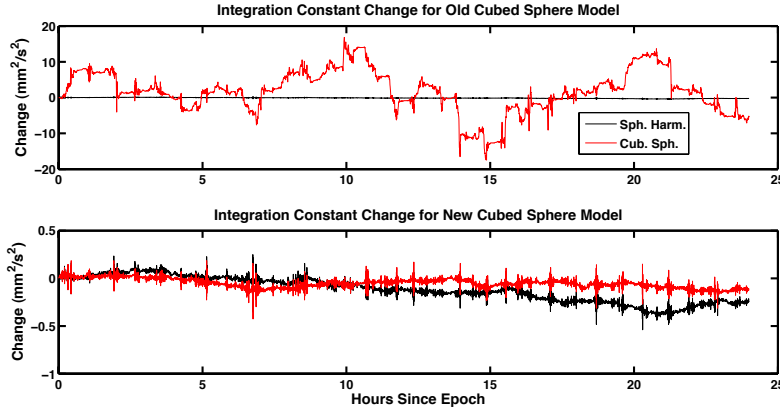
Figure 5.5: Changes in integration constant with the new CS-162 model configuration versus the configuration of Beylkin and Cramer (2002) for an orbit with an inclination of 15° and right ascension of 50° at a 300 km altitude.

Instead of testing the cubed sphere under the Laplace criterion, this study applies another technique using the Jacobi-like integration constant (Bond and Allman, 1996),

$$K = \frac{\dot{\mathbf{r}} \cdot \dot{\mathbf{r}}}{2} - \left[\frac{\mu}{r} - U(\mathbf{r}, t) \right] - \omega \cdot (\mathbf{r} \times \dot{\mathbf{r}}). \tag{5.2}$$

This constant assumes that the geopotential is time varying in the inertial reference frame, which is valid due to Earth rotation. Here, ω is the angular velocity of the primary body. For a valid gravity model and a propagated orbit, K must remain constant over time, or $K(t) - K(t_\circ) = 0$. To simplify notation, we denote $K_\circ = K(t_\circ)$. In practice, the constant fluctuates due to the numerical integration process and errors in the estimate of the gravity field.

We designed these new models to improve accuracy, specifically the integration constant performance, when compared to the models developed for Beylkin and Cramer (2002). Figure 5.5 illustrates the extent of the improvement. Previously, the cubed sphere integration constant deviations were consistently 1-3 orders of magnitude greater than those of the spherical harmonic model. This would have resulted in reducing the validity of the model for applications requiring long-term orbit propagation. In some cases, such as this example, the integration constant test for the new cubed sphere model performs even better than the spherical harmonic model.

Table 5.2: Percentage of runs where $O(K-K_o)$ is less than the other model.

Model	Cubed Sphere	Spherical Harmonics
CS-30	0.024%	0.020%
CS-76	0.012%	0.008%
CS-162	0.264%	0.272%
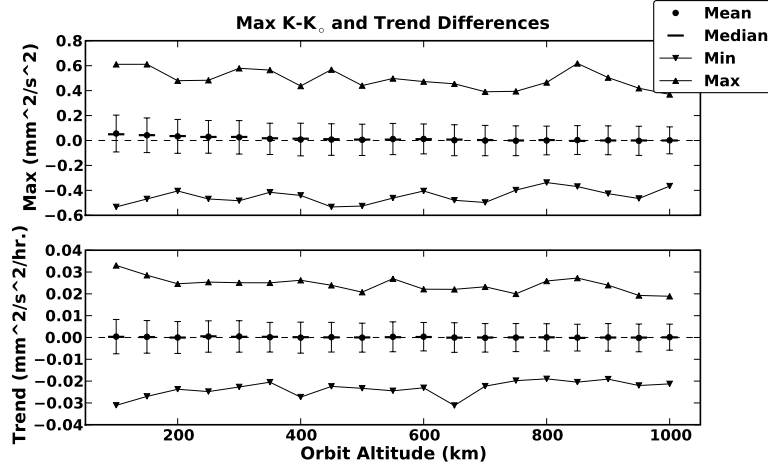
Figure 5.6: Comparison of the integration constant variations for the CS-30 model with the spherical harmonics base model. Error bars are 1-σ.

A major concern when comparing the variations in the integration constant for the cubed sphere and the spherical harmonic models is the relative magnitude of the fluctuations. In some cases, the magnitude of the variations of the cubed-sphere model were as much as an order of magnitude less than the spherical harmonic model, and vice versa. Table 5.2 provides the percentage

of the 24,605 runs for each model that exhibited this behavior. In most cases, the order of magnitude of the fluctuations was the same. However, a small percentage of the tests yielded integration constant changes an order of magnitude less for one model when compared to the other. In the case of the CS-162 model, where the percentage of runs sharply increased, tests at altitudes at or below 250 km exhibited the larger fluctuations.

In Figure 5.6, we illustrate the performance of the CS-30 model under the integration constant test as compared to the spherical harmonic model. The top figure depicts the relative performance of the maximum fluctuations. For the comparison of the fluctuation magnitude, the maximum absolute deviation for both the cubed-sphere model orbit and the spherical harmonics orbit are differenced. We compute the mean, median, min, max, and standard deviation of these differences for all orbits at a given altitude, and illustrate these values for all altitudes tested. We note that a negative number indicates the integration constant fluctuations for the cubed-sphere model orbit are less than those of the spherical harmonic model orbit. The bottom subplot portrays the relative performance of trends in the integration constant variations. For each orbit, we perform a linear fit to the integration constant fluctuations. The trend in the fluctuations is described by the slope, with Figure 5.6 illustrating the differences in these trends. For the slope in the trend line, units are designated as $mm^2/sec^2/hour$, since the units of the integration constant are mm^2/sec^2 (i.e. change in the constant per hour). For altitudes below 400 km, the mean and median magnitude differences indicate the spherical harmonic model slightly outperforms the cubed sphere. However, the average difference drops to nearly zero above 400 km. The maximum and minimum differences remain consistent. Given the mean and median differences in the trend line slope are around zero with 1-σ values within 0.01 $mm^2/sec^2/hour$, the two models typically have the same long term trend.

Similarly, Figure 5.7 illustrates the integration constant performance for the CS-76 model. We note that the magnitude and trend of the integration constant change is larger for the cubed sphere at lower altitudes, but settles at around 300 km. The median is smaller than the mean at these lower altitudes, indicating a relatively small number of tests increase the mean value. Again,
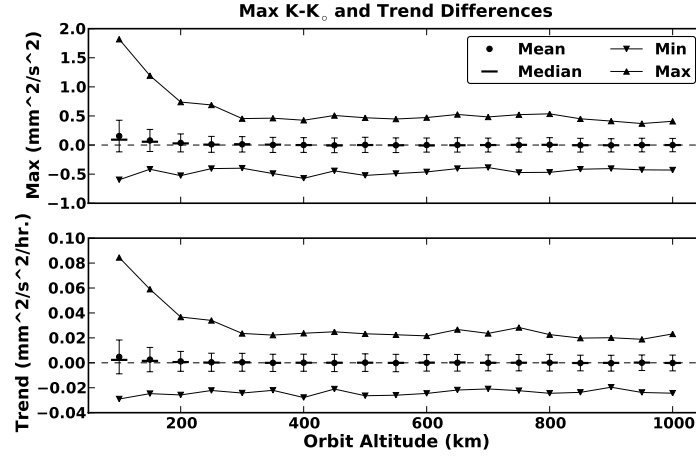
Figure 5.7: Comparison of the integration constant variations for the CS-76 model with the spherical harmonics base model. Error bars are 1-σ.
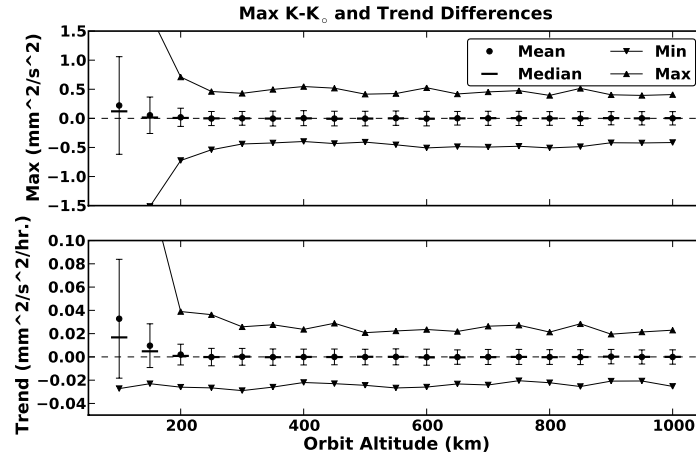
Figure 5.8: Comparison of the integration constant variations for the CS-162 model with the spherical harmonics base model. Error bars are 1-σ.

the models closely agree for higher altitudes, as indicated by the mean and median values with small error bars.

Results for the CS-162 model are provided in Figure 5.8. We note that some extreme values have been truncated to improve visibility of performance statistics at higher altitudes. In the case of the magnitude differences, the minimum values for the 100 and 150 km orbits are -3.39 and -1.51 mm^2/sec^2, respectively. The maximum values are 5.20 and 1.79 mm^2/sec^2. In the case of the trend slope differences, the missing maximums are 0.44 and 0.14 $mm^2/sec^2/hour$. Like the CS-76 model, differences between the cubed sphere and spherical harmonic models are greater at lower altitudes. This trend remains consistent through the remaining tests, and is attributed to the greater differences in the gravity anomalies at lower altitudes seen in the next section. In this case, the differences in the models settle around 250 km.

5.2.3   Orbit Propagation Comparisons

To assess the orbit propagation accuracy, we difference the propagated trajectories from those using the spherical harmonic model, and compute the 3D RMS difference. An orbit propagation "error" refers to the difference between the cubed sphere and the spherical harmonic model orbits.
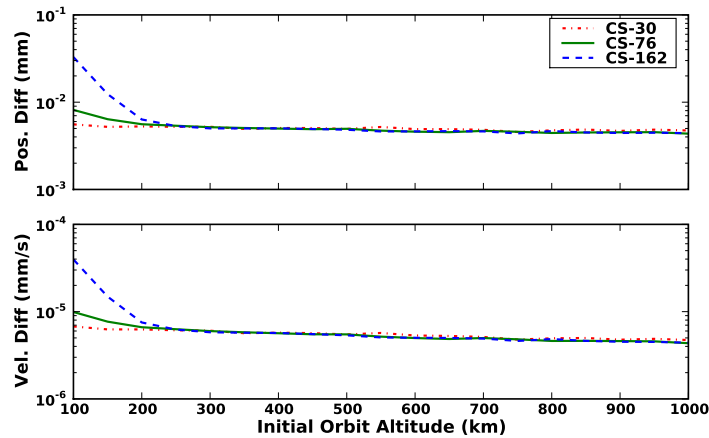
Figure 5.9: Summary of the total 3D RMS orbit propagation differences for the CS-30, CS-76 and CS-162 models at a given initial altitude.

Figure 5.9 summarizes the orbit propagation results for the CS-30, CS-76, and CS-162 cubed-sphere models. These 3D RMS values include the state differences at all times and orbits, independent of the orbit initial conditions. Orbit position and velocity differences are on the order of fractions of a mm and mm/sec, respectively. The magnitude of the orbit propagation errors for the three models converges at 200 km, and continues with a slight downward trend as orbit altitude increases. At low altitudes, results improve with reduced fidelity of the base model, which is consistent with the gravity anomalies provided in Figure 5.1. Of course, these results may be adjusted by an appropriate configuration of the cubed sphere for high-degree base models. However, this demonstrates that very close agreement with the base model can be achieved.

Table 5.3: Average Speedup Factor for the Cubed Sphere Versus the Base Model

Cubed-Sphere Model	Spherical Harmonic Model	Average Speedup Factor
CS-30	20x20	0.73
CS-76	70x70	5.97
CS-162	150x150	30.82

In Table 5.3, we present the ratio of the time required to propagate the orbit using the spherical harmonics and the cubed sphere. The computation time used in these calculations includes only the execution of the Runge-Kutta 7(8) algorithm, and does not include file load times or initialization. As expected, the file load time for the cubed sphere exceeds that of the spherical harmonics, however this may be mitigated through a careful implementation. Propagation using the CS-30 model is slower than the corresponding spherical harmonics model. Later results demonstrate the cubed-sphere model can be faster than the spherical harmonic model for all degrees greater than 20. We also note that these results are computer and compiler dependent. These results are an average over six individual computers, each with different capabilities. Evaluation time of the spherical harmonic model varied most with each computer.

In Figures 5.10 and 5.11, we illustrate orbit propagation performance for the CS-162 model at 300 km. There do not appear to be any trends in the errors when observing their distribution based on inclination and right ascension of the ascending node. The relatively large deviation at
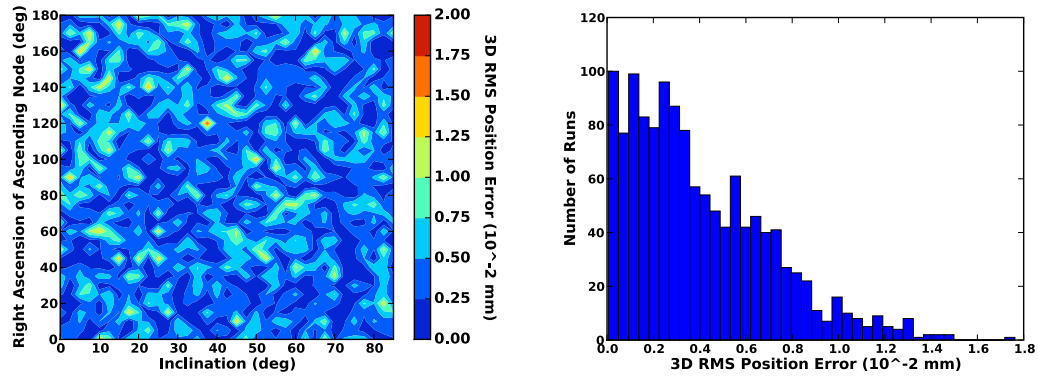
Figure 5.10: Spatial distribution and histogram of the 3D RMS position differences for propagated orbits initially at 300 km with the CS-162 model.
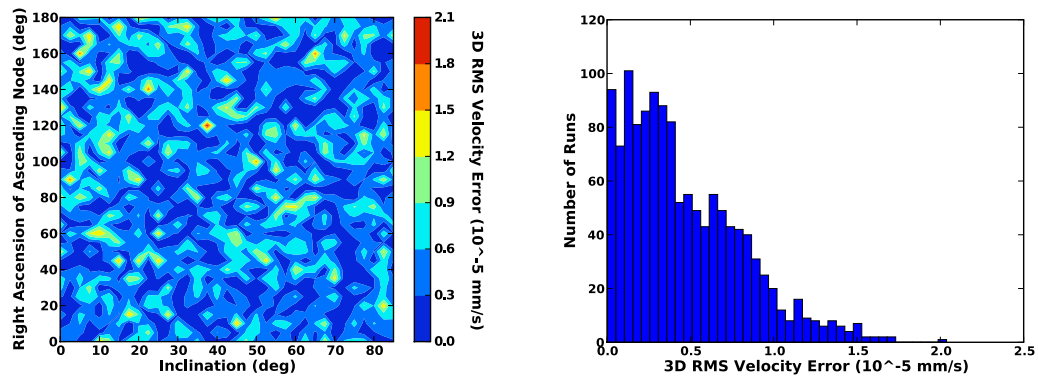
Figure 5.11: Spatial distribution and histogram of the 3D RMS velocity differences for propagated orbits initially at 300 km with the CS-162 model.

the right ascension of the ascending nodes and inclination combination of 120° and 37.5° is directly correlated with gravity anomalies in Figure 5.4. Specifically, the orbit groundtrack intersects the large gravity anomalies at approximately 28° latitude and 92° longitude twice during the orbit, and once directly over the peak anomaly near Haiti. Other than this orbit, all others are within 0.015 mm of those computed via the spherical harmonics. The spatial distribution of the velocity errors roughly corresponds to that of the position errors.
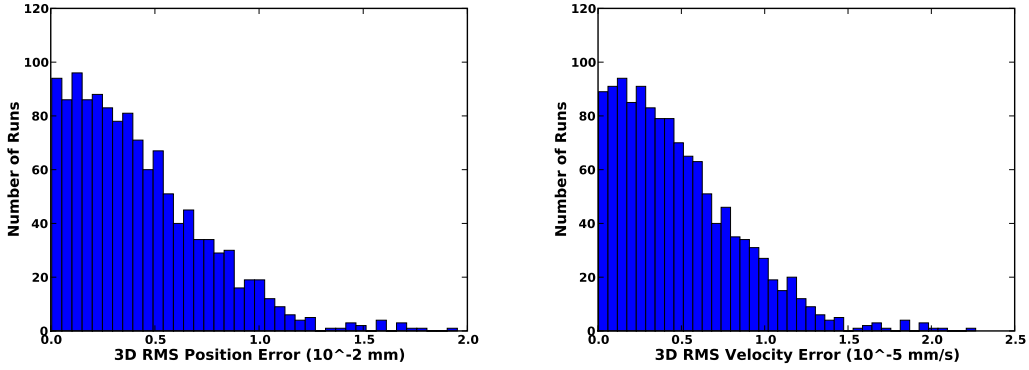
Figure 5.12: Distribution of 3D RMS differences for propagated orbits initially at 300 km with the CS-30 model.
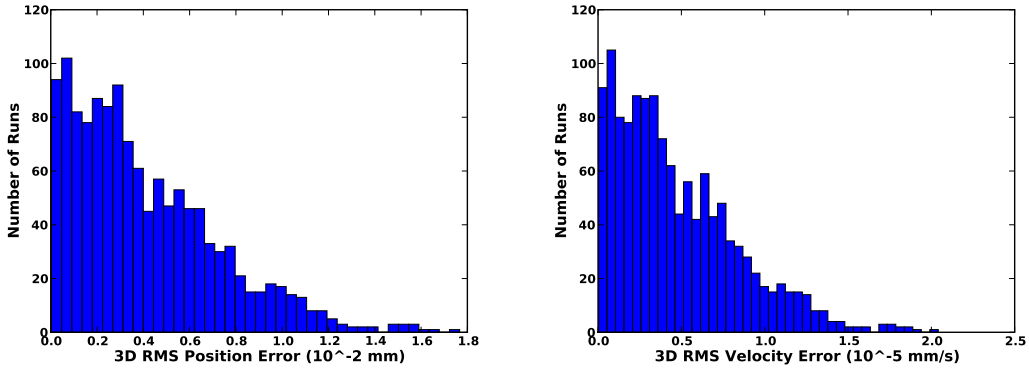
Figure 5.13: Distribution of 3D RMS differences for propagated orbits initially at 300 km with the CS-76 model.

Histograms of the propagated state errors for the CS-30 and CS-76 models at 300 km are provided in Figures 5.12 and 5.13, respectively. We do not include corresponding contour plots

since results are similar to those seen for the CS-162 model. Accuracy differences in the CS-30 and CS-76 models are illustrated sufficiently by the histogram plots.

Table 5.4: Cubed Sphere State 3D RMS Performance at 300 km

Model	Component	Min	Max	Mean	Median
CS-30	Position (mm)	$4.70\text{x}10^{-5}$	0.0200	0.0042	0.0036
	Velocity (mm/s)	$2.99\text{x}10^{-8}$	$2.27\text{x}10^{-5}$	$4.84\text{x}10^{-6}$	$4.11\text{x}10^{-6}$
CS-76	Position (mm)	$3.25\text{x}10^{-5}$	0.0177	0.0041	0.0033
	Velocity (mm/s)	$3.22\text{x}10^{-8}$	$2.04\text{x}10^{-5}$	$4.73\text{x}10^{-6}$	$3.79\text{x}10^{-6}$
CS-162	Position (mm)	$5.71\text{x}10^{-5}$	0.0176	0.0040	0.0033
	Velocity (mm/s)	$2.50\text{x}10^{-8}$	$2.04\text{x}10^{-5}$	$4.64\text{x}10^{-6}$	$3.80\text{x}10^{-6}$

Table 5.4 summarizes the 3D RMS orbit propagation differences at 300 km. To better interpret these results, we perform a similar test using no gravity perturbations, i.e. the two-body problem, and compare results to those computed via Kepler's Equation. In Table 5.5, we provide these two-body propagation errors. After comparing these two tables, we see that the mean and median errors are similar, but slightly larger with gravity perturbations. This implies that, at this level of precision in the cubed-sphere models, the orbit propagation tolerance dominates the mean error. We may change this by using a different integration tolerance, but we expect to lose approximately three digits when integrating for 24 hours. However, the differences in the gravity models increase the minimum and maximum errors by an order of magnitude.

Table 5.5: Keplerian Orbit Propagation Accuracy at 300 km

Component	Min	Max	Mean	Median
Position (mm)	1.16×10^{-4}	0.0062	0.0015	0.0012
Velocity (mm/s)	1.27×10^{-7}	7.19×10^{-5}	1.71×10^{-6}	1.42×10^{-6}

Orbits with an eccentricity of 0.05 were tested using a similar scheme with the altitude of periapsis set at 300 km. Results are comparable to those depicted here for all three of the cubed-sphere models. Although increasing the variations in the eccentricity provides a more comprehensive comparison, larger values yield an altitude of apoapsis above 1000 km. At these altitudes, the gravity anomalies of the cubed sphere relative to the spherical harmonics are below the machine

precision (as seen in Figure 5.1). Thus, higher eccentricities are not of significant interest.

To test the effects of primary shell boundaries on propagated orbits, differences for a circular orbit at 358.7702 km were profiled. This altitude corresponds with the lower bound of the 4th primary shell. Both the integration constant and the orbit differences tests yield results comparable to those already illustrated for a 350 km orbit. Thus, for these cubed-sphere models, the possible discontinuities at primary shell boundaries do not appear to influence the orbit propagation differences.

5.3   Models Designed for Speed

In this section, we consider orbit propagation with cubed-sphere models designed for optimal speed. We repeat the tests described previously, but, for reasons described in the next section, we raise the minimum altitude tested to 200 km.

5.3.1   Model Configuration

We generate CS-106f, CS-100f, and CS-176f models based on 20×20, 70×70, and 150×150 spherical harmonic models, respectively, that are precise to 12 digits (8.9×10^{-15} km/s^2 or 8.9×10^{-7} mGal) at or above 300 km. We also limit file sizes to 1.8 GB. To prevent any confusion with previous or future models, we temporarily add the 'f' suffix to designate a fast model.

Table 5.6: Summary of fast cubed-sphere models for rapid orbit propagation

Model	Base Model	l	m	M	N	Size (MB)	Max. Deviation (km/s^2)
CS-106f	20×20	3	5	70	424	623	3.8×10^{-15}
CS-100f	70×70	3	9	160	400	1385	9.0×10^{-15}
CS-176f, 200-1,000 km	150×150	3	9	56	704	1379	6.8×10^{-15}

We provide descriptions of these fast cubed-sphere models in Table 5.6. With these models, we reduce the radial interpolation from eleventh to third degree polynomials. Similarly, we shift from eleventh to fifth or ninth degree B-splines. We note that the increased degree of B-Spline

interpolation m from the CS-106f to CS-100f models allows for the use of a sparser grid when modeling the higher spatial resolution of the 70×70 model. Additionally, due to memory limitations and the region of interest, we only generate a CS-176f model covering altitudes in the range 200-1,000 km. The properties listed in Table 5.6 for the CS-176f model reflect this radially constrained model.
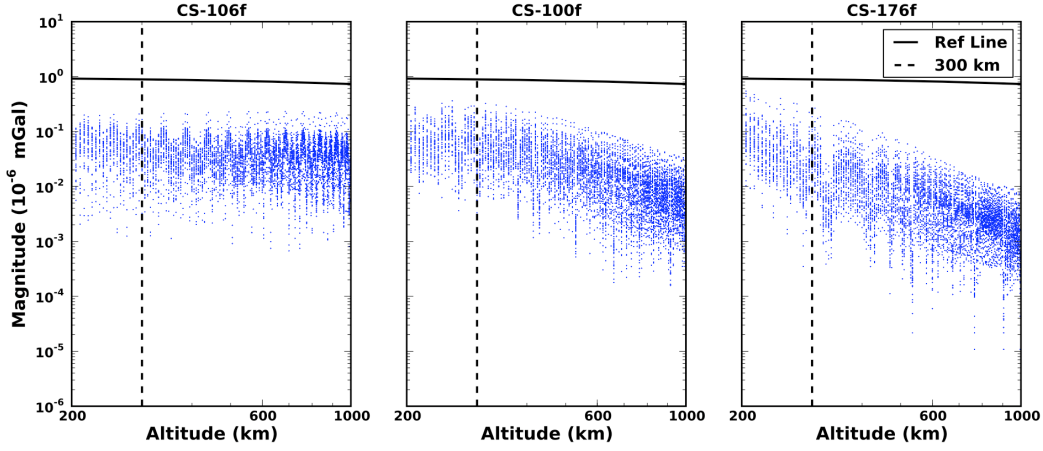
Figure 5.14: Variations in gravity anomalies with altitude for 42 points on the Earth using the CS-106f, CS-100f, and CS-176f models.
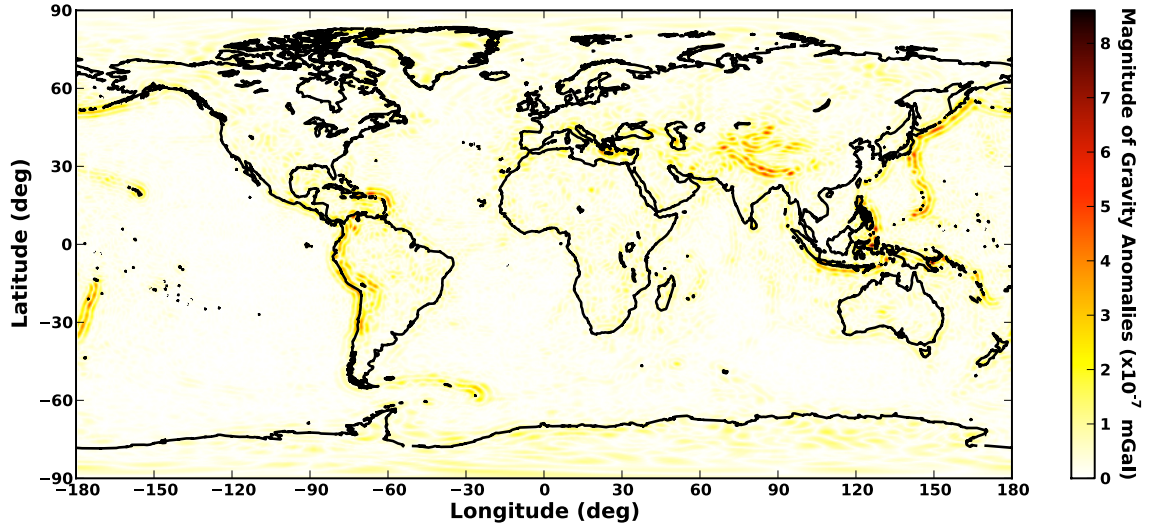
Figure 5.15: CS-176f gravity anomalies at 300 km

Figure 5.14 illustrates the variations in the gravity anomalies with altitude for the fast cubed-sphere models. For the 200-1,000 km altitude range, these models meet precision requirements. Unlike the other models, anomalies for the CS-106f model do not decay with altitude, which affects later orbit propagation results. All models demonstrate the periodic variations seen in Figure 5.1. Again, this is a result of decreasing precision with distance from the Chebyshev interpolation nodes.

In Figure 5.15, we present the gravity anomalies at 300 km above the Earth's surface for the CS-176f model. The cubed-sphere grid spacing no longer dominates the gravity differences. Instead, differences are correlated with the absolute gravity variations for the Earth. These anomalies are within the 8.9×10^{-7} mGal precision requirement at 300 km. We do not provide results for the CS-106f and CS-100f models since they yield results similar to those of Figures 5.2 and 5.3, except with a larger magnitude. They also meet the precision requirements.

5.3.2   Orbit Propagation Comparisons

Using the same procedure described in Section 5.2.3, we compare the trajectories generated via the cubed-sphere model with those using the spherical harmonic model. We provide the speedup factors for these fast models in Table 5.7. Results demonstrate that sacrificing two digits of precision in the cubed-sphere model yields 2-3 times faster integration than the models of Section 5.2. Lower degree models yield the largest improvements because of the greater reduction in degree of the B-spline interpolants.

Table 5.7: Average Speedup Factors for the Fast Cubed-Sphere Models Versus the Base Model

Cubed-Sphere Model	Spherical Harmonic Model	Average Speedup Factor
CS-106f	20x20	2.24
CS-100f	70x70	12.54
CS-176f	150x150	60.10

We summarize orbit differences in Table 5.8. When compared to the results in Table 5.4, the minimum errors increase by an order of magnitude. Although slightly larger, the mean and median errors are still dominated by the orbit propagation algorithm. Finally, the maximum errors

Table 5.8: Cubed Sphere State 3D RMS Performance at 300 km

Model	Component	Min	Max	Mean	Median
CS-106f	Position (mm)	8.6×10^{-4}	0.0392	0.0075	0.0060
	Velocity (mm/s)	7.59×10^{-7}	4.54×10^{-5}	8.65×10^{-6}	6.87×10^{-6}
CS-100f	Position (mm)	5.84×10^{-4}	0.0287	0.0056	0.0045
	Velocity (mm/s)	5.67×10^{-7}	3.33×10^{-5}	6.41×10^{-6}	5.09×10^{-6}
CS-176f	Position (mm)	3.85×10^{-4}	0.0225	0.0039	0.0033
	Velocity (mm/s)	4.17×10^{-7}	2.61×10^{-5}	4.51×10^{-6}	3.71×10^{-6}

increase by approximately a factor of two.

Figure 5.16 illustrates the 3D RMS orbit propagation errors with the fast cubed-sphere models. Lower altitude orbits exhibit a slightly reduced accuracy, which is expected given the reduced model accuracy. For the CS-106f model, errors do not attenuate with altitude as a result of the reduced slope in the gravity anomaly changes with height seen in Figure 5.14. Otherwise, high-altitude trajectory errors are similar to those in Figure 5.9.
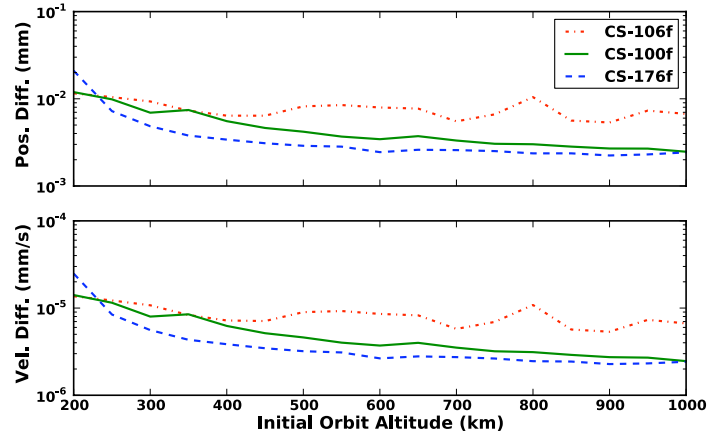
Figure 5.16: Summary of the total 3D RMS orbit propagation differences for the CS-106f, CS-100f and CS-176f models at a given initial altitude.

5.4   Chapter Summary

Results indicate that the cubed-sphere model can closely approximate a spherical harmonic model. Tests demonstrate agreements in orbit propagation on the order of fractions of a millimeter. Integration of orbits via the cubed-sphere model equivalent to a 150x150 spherical harmonic model was over 30 times faster than via the base model. As Table 5.3 indicates, the break-even point is achieved at above degree 20.

Cubed-sphere models configured for a highly-precise representation of the gravity field greatly reduced variations in the integration constant, with changes consistent between the cubed sphere and the spherical harmonic models. The agreement between the models is reduced below 200 km. In some cases, the cubed-sphere model actually performs better than the corresponding spherical harmonic model, probably due to the random nature of fluctuations in the integration constant near the limit of the machine precision. Gravity anomalies were also reduced, and are now within 10^{-6} mGal for all altitudes above the Earth, and less than 10^{-7} mGal for altitudes at or above 300 km when using the current configuration.

Models designed for fast evaluation demonstrated an additional 2-3 times improvement in orbit propagation speed. Given the relaxed precision requirements, gravity anomalies were an order of magnitude greater than those of the models designed for accuracy. However, orbit propagation accuracy was only slightly reduced. Thus, assuming reduced orbit propagation accuracy requirements, large improvements in propagation speed may be achieved.

Chapter 6

Orbit Determination with the Cubed-Sphere Model

In this chapter, we extend the use of the cubed-sphere model to the problem of orbit determination. The previous chapter demonstrates that the cubed-sphere model can provide increased orbit propagation efficiency with little or no difference when compared to base model derived solutions. As mentioned in Chapter 1, the astrodynamics community now requires near real-time orbit determination for multiple applications. Here, we study the effects of faster state propagation on the computational efficiency of real-time and near real-time orbit determination systems. As mentioned in Chapter 2, estimation of the interpolating coefficients in the cubed-sphere model is intractable, thus we do not consider corrections to the gravity field in this chapter. We cover gravity estimation using the MRQSphere model in Chapter 7.

The first section describes the configuration of the cubed-sphere models used throughout this chapter. We then describe the filter implementation used for future orbit determination tests. Next, we describe the addition of second derivatives, i.e. the Jacobian of the gravity acceleration with respect to the position, to the cubed-sphere model for use in the extended Kalman Filter (EKF). This includes a description of the precision of the generated state transition matrix. Section 6.4 details the tests employed to assess filter performance with the cubed-sphere model, followed by results of these tests in Section 6.5. Finally, we summarize all results in Section 6.6. The methods in this chapter are similar to those in Jones et al. (2010c), but many of the results have been improved with better software implementations.

6.1   Model Configurations

Before adding the cubed-sphere model to the orbit determination process, we require a larger selection of models, i.e. models based on 20×20 through 200×200 spherical harmonic models in increments of 10×10. In Chapter 5, we fix the degree of the Chebyshev interpolation for all models and only vary the grid density on the surface of the cube. Using the procedure described in Section 4.1.2, we now allow this parameter to vary with each model. For this reason, models using Chebyshev polynomials of degree ten or less will exhibit improved computational efficiency when compared to those of Chapter 5. However, we still use eleventh degree B-splines for all models. Like the cubed-sphere models of Section 5.2, we require a precision of 8.9×10^{-9} mGal at 300 km in altitude or above for these new models, and minimize the file size at the detriment of evaluation speed. Configurations of these new cubed-sphere models may be found in Table 6.1.

For these models, we change the formulation of the spherical harmonic base model to remove the singularity at the poles. In this chapter, we simulate a GRACE satellite, which has an inclination of 89°. For this reason, we switch to the Cartesian formulation of the spherical harmonic model (see Section 4.1.1) to avoid any problems when evaluating the gravity field 1° from the poles.

In Figures 6.1 and 6.2, we illustrate variations in the gravity anomalies, as a function of height, for all of the models described in Table 6.1. Each model satisfies the precision requirement at or above 300 km in altitude. Some models exhibit discontinuities between primary shells (e.g., see the CS-94 model), but these jumps remain within the precision requirement.

6.2   Filter Implementation

In this research, we study filter efficiency improvements for both the EKF and UKF when using the cubed-sphere model for evaluation of the gravity field. Section 3.3 introduces each of these filters. In this section, we describe both the filter configurations and integration of the cubed-sphere model with the EKF and UKF.

Using the EKF requires the evaluation of the gravity acceleration's Jacobian with respect to
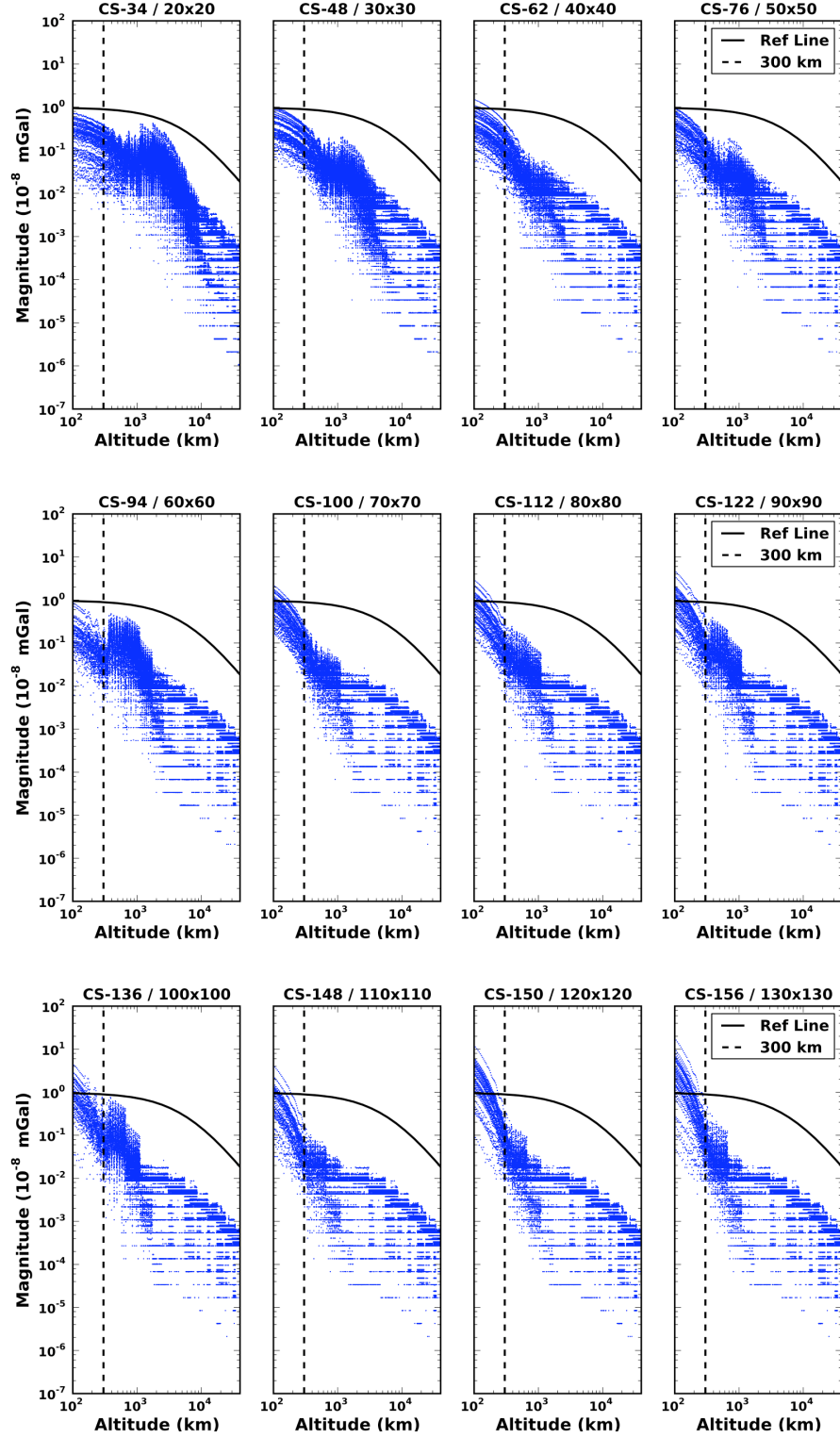
Figure 6.1: Differences between the spherical harmonic model and the cubed-sphere model for base model degrees 20 through 130.
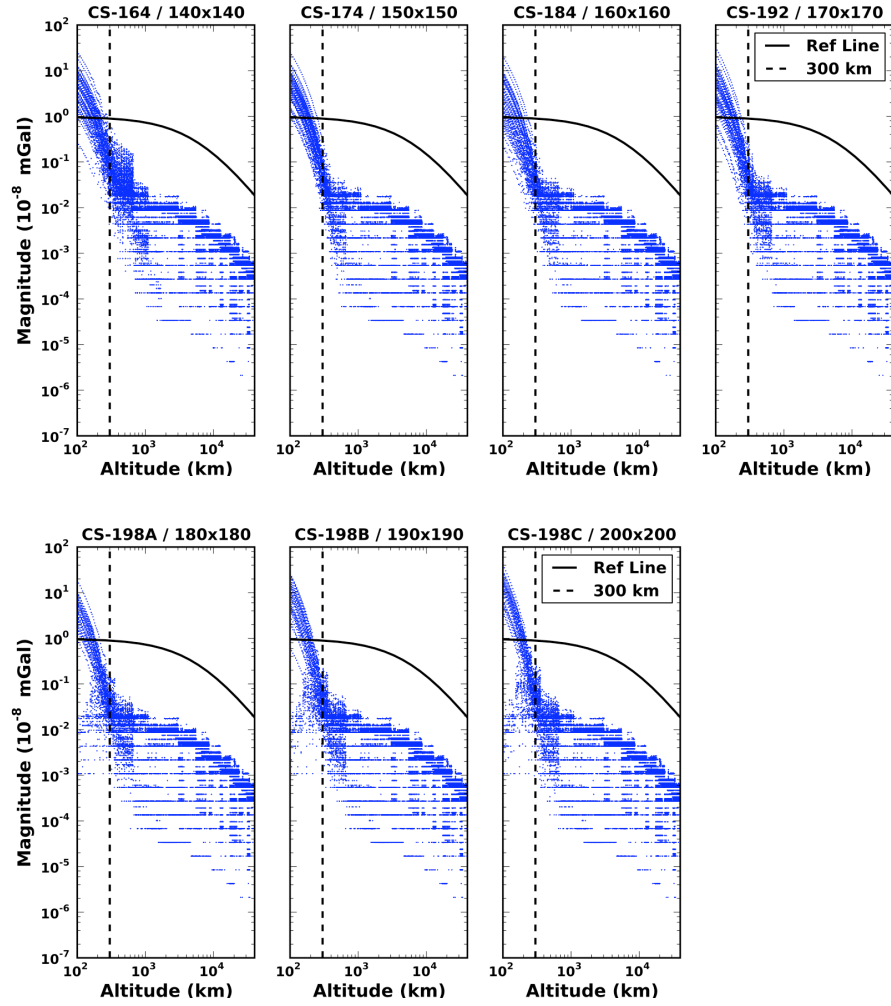
Figure 6.2: Differences between the spherical harmonic model and the cubed-sphere model for base model degrees 140 through 200.

Table 6.1: Precise cubed-sphere gravity model configurations for degree 20 through 200.

Model	Base Model	l	m	M	N	Size (MB)
CS-34	20×20	6	11	14	136	34
CS-48	30×30	7	11	14	192	67
CS-62	40×40	8	11	14	248	115
CS-76	50×50	8	11	14	304	163
CS-94	60×60	8	11	14	376	237
CS-100	70×70	9	11	14	400	294
CS-112	80×80	9	11	14	448	361
CS-122	90×90	9	11	14	488	422
CS-136	100×100	9	11	14	544	515
CS-148	110×110	10	11	14	592	662
CS-150	120×120	10	11	14	600	679
CS-156	130×130	10	11	14	624	731
CS-164	140×140	10	11	14	656	802
CS-174	150×150	11	11	14	696	978
CS-184	160×160	11	11	14	736	1087
CS-192	170×170	11	11	14	768	1178
CS-198A	180×180	11	11	14	792	1248
CS-198B	190×190	11	11	14	792	1248
CS-198C	200×200	11	11	14	792	1248

the satellite position; a capability we now add to the cubed-sphere model. Recall that the EKF maps (to first order) the covariance matrix P_{i-1} from time t_{i-1} to t_i using the state transition matrix $\Phi(t_i, t_{i-1})$ in Equation 3.27. As implied by Equations 3.8 and 3.6, generation of $\Phi(t_i, t_{i-1})$ requires the Jacobian of the gravity acceleration

$$\frac{\partial F(t_i)}{\partial \mathbf{X}(t_i)} = \frac{\partial \mathbf{a}_{\text{grav}}}{\partial \mathbf{r}} = \frac{\partial^2 U}{\partial \mathbf{r}^2} = \begin{bmatrix} \dfrac{\partial^2 U}{\partial x^2} & \dfrac{\partial U^2}{\partial x \partial y} & \dfrac{\partial U^2}{\partial x \partial z} \\[2mm] \dfrac{\partial U^2}{\partial x \partial y} & \dfrac{\partial^2 U}{\partial y^2} & \dfrac{\partial U^2}{\partial y \partial z} \\[2mm] \dfrac{\partial U^2}{\partial x \partial z} & \dfrac{\partial U^2}{\partial y \partial z} & \dfrac{\partial^2 U}{\partial z^2} \end{bmatrix}. \tag{6.1}$$

Since this matrix is symmetric, we only require the evaluation of six terms: $\partial^2 U/\partial x^2$, $\partial^2 U/\partial y^2$, $\partial^2 U/\partial z^2$, $\partial^2 U/\partial x \partial y$, $\partial^2 U/\partial x \partial z$, and $\partial^2 U/\partial x^2$. We model these derivatives as submodels in the cubed-sphere model. This requires additional memory since P in Equation 2.80 has been increased by 6. With this addition, we add the cubed-sphere model to the EKF.

Since the UKF propagates individual σ-points, and does not require the evaluation of any Jacobians, we require no changes to the cubed-sphere model for this filter. We add capabilities to the integration software that simultaneously propagates the σ-points, but this is simply a choice of implementation. One may also propagate each point forward in time via separate executions of the integration software.

To make this assessment of orbit determination speed improvements more realistic, we include the NRLMSISE-00 (Picone et al., 2002) model of atmospheric density in the filter's force model. Highly precise orbit determination systems require the modeling of all known perturbing forces, e.g. atmospheric drag. The contribution of each of these perturbations varies with time, the satellite state, and other variables. We are interested in low-altitude scenarios where gravity perturbations are strongest, thus requiring higher-degree gravity models. The second largest perturbing force for such low-altitude satellites is drag due to interactions with the residual atmosphere (Vallado and McClain, 2007). We model the drag acceleration by

$$\mathbf{a}_{\mathrm{drag}} = -\frac{1}{2}\frac{C_D A}{m}\rho(t,\mathbf{r})\left|\mathbf{v}_{\mathrm{rel}}\right|\mathbf{v}_{\mathrm{rel}} \tag{6.2}$$

where C_D is the coefficient of drag, A and m are the satellite's area and mass, respectively, ρ is the atmospheric density, and $\mathbf{v}_{\mathrm{rel}}$ is the velocity vector of the satellite relative to the atmosphere. We assume

$$\mathbf{v}_{\mathrm{rel}} = \mathbf{v}_{\mathrm{sat}} - \boldsymbol{\omega}_\oplus \times \mathbf{r}_{\mathrm{sat}}, \tag{6.3}$$

where $\boldsymbol{\omega}_\oplus$ is the rotation vector of the Earth. In other words, we presume the residual atmosphere has circular motion based on the primary body's rotation rate. Atmospheric density models seek to provide an accurate value of ρ based on the satellite position, time, and other parameters. Given the computational complexity of modern atmospheric density models, we include the NRLMSISE-00 model in our filter dynamics. Specifically, we use C code provided by Dominik Brodowski.[1] With the increased fixed-cost of evaluating the equations of motion, including this model reduces integrator speedup. We also include C_D in the estimated state vector and assume A/m is known.

---

[1] http://www.brodo.de/space/nrlmsise/

We include filter process noise to compensate for force modeling errors. Incorrect propagation of the filter state, due to errors in the force model, impacts a filter in various ways. To partially account for these errors, we include filter process noise in both the EKF and UKF. This adds a correction term Q (see Equations 3.27 and 3.39) to the time update of the state covariance matrix (Tapley et al., 2004b), which we define as

$$Q = \begin{bmatrix} \dfrac{\Delta t^4}{4}\sigma_{\ddot{X}}^2 & 0 & 0 & \dfrac{\Delta t^3}{2}\sigma_{\ddot{X}}^2 & 0 & 0 \\[2ex] 0 & \dfrac{\Delta t^4}{4}\sigma_{\ddot{Y}}^2 & 0 & 0 & \dfrac{\Delta t^3}{2}\sigma_{\ddot{Y}}^2 & 0 \\[2ex] 0 & 0 & \dfrac{\Delta t^4}{4}\sigma_{\ddot{Z}}^2 & 0 & 0 & \dfrac{\Delta t^3}{2}\sigma_{\ddot{Z}}^2 \\[2ex] \dfrac{\Delta t^3}{2}\sigma_{\ddot{X}}^2 & 0 & 0 & \Delta t^2\sigma_{\ddot{X}}^2 & 0 & 0 \\[2ex] 0 & \dfrac{\Delta t^3}{2}\sigma_{\ddot{Y}}^2 & 0 & 0 & \Delta t^2\sigma_{\ddot{Y}}^2 & 0 \\[2ex] 0 & 0 & \dfrac{\Delta t^3}{2}\sigma_{\ddot{Z}}^2 & 0 & 0 & \Delta t^2\sigma_{\ddot{Z}}^2 \end{bmatrix}, \tag{6.4}$$

where Δt is the time between measurements and $\sigma_{\ddot{X}}$, $\sigma_{\ddot{Y}}$, and $\sigma_{\ddot{Z}}$ represent the standard deviation of the unknown acceleration in each component direction. Filter tuning refers to the selection of these σ values, which are largely unknown, to yield a more accurate estimate. Including Q prevents filter saturation, i.e. the ignoring of observations because the state-error covariance matrix is nearly zero. Derived from Equations 4.9.47 and 4.9.50 of Tapley et al. (2004b), Equation 6.4 assumes a constant acceleration in each component direction for small Δt. In this implementation, we do not add process noise for large Δt since this violates the constant acceleration assumption. We set $\sigma_Q = \sigma_{\ddot{X}} = \sigma_{\ddot{Y}} = \sigma_{\ddot{Z}}$ and select a value such that approximately 97.1% of all estimated state errors are within the 3-σ filter covariance ellipsoid. We generate a value of σ_Q for each gravity model degree.

During the course of research, we observed that the mapping of the state-error covariance matrix using $\Phi(t_i, t_{i-1})$ in the EKF did not prevent filter saturation when observation gaps are

present. Thus, we apply the phasing factor

$$\bar{P}_i = 4^{\Delta t/\gamma} * \left(\Phi(t_i, t_{i-1})P_{i-1}\Phi^T(t_i, t_{i-1})\right) \tag{6.5}$$

to the covariance matrix after an observation gap where γ is a time scale. We note that we either apply this phasing factor or the process noise matrix Q, but never both at the same time. We set $\gamma = 60$ minutes (3600 sec), meaning this phase factor doubles the estimated-state standard deviation every hour when observations are not available. The UKF did not exhibit this problem, which we attribute to the inclusion of second- and third-order effects in propagating the covariance matrix with the unscented transformation.

In both the EKF and UKF, we process a combination of range ρ and range-rate $\dot{\rho}$ measurements

$$\rho = \sqrt{(X - X_s)^2 + (Y - Y_s)^2 + (Z - Z_s)^2} \tag{6.6}$$

$$\dot{\rho} = \left((X - X_s)\left(\dot{X} - \dot{X}_s\right) + (Y - Y_s)\left(\dot{Y} - \dot{Y}_s\right) + (Z - Z_s)\left(\dot{Z} - \dot{Z}_s\right)\right)/\rho \tag{6.7}$$

where X, Y, and Z are the inertial components of the satellite position and X_s, Y_s, and Z_s are the inertial components of the reference station position. We then set

$$G(t_i) = \begin{bmatrix} \rho \\ \dot{\rho} \end{bmatrix}, \tag{6.8}$$

and, using Equation 3.12,

$$\tilde{H} = \begin{bmatrix} \dfrac{X - X_s}{\rho} & \dfrac{Y - Y_s}{\rho} & \dfrac{Z - Z_s}{\rho} & 0 & 0 & 0 \\[3ex] \dfrac{\dot{X} - \dot{X}_s - \dot{\rho}\dfrac{\partial \rho}{\partial X}}{\rho} & \dfrac{\dot{Y} - \dot{Y}_s - \dot{\rho}\dfrac{\partial \rho}{\partial Y}}{\rho} & \dfrac{\dot{Z} - \dot{Z}_s - \dot{\rho}\dfrac{\partial \rho}{\partial Z}}{\rho} & \dfrac{X - X_s}{\rho} & \dfrac{Y - Y_s}{\rho} & \dfrac{Z - Z_s}{\rho} \end{bmatrix}^* . \tag{6.9}$$

We include rows of Equation 6.9 as appropriate for a given set of observations.

6.3 Propagation of the State Transition Matrix

To determine the minimum precision required for the cubed-sphere-model representation of the Jacobian, we approximate the effects of errors in $A(t)$ on the resulting state transition matrix

$\Phi(t, t_\circ)$. By limiting the number of accurate digits in $A(t)$, and thus $\dot{\Phi}(t, t_\circ)$, we reduce the accuracy of mapping a state deviation vector $\Delta\mathbf{x}_0$ with $\Phi(t, t_\circ)$. In summary, we control the accuracy of $A(t)$ and observe errors in the mapped deviation vector. We select an initial satellite state by fixing the semimajor axis, eccentricity, and true anomaly to 6678.1363 km, 1.0×10^{-5}, and $0°$, respectively, and randomly select the inclination, right ascension of the ascending node, and argument of periapsis. We convert these orbital elements into Cartesian coordinates to get an initial state $\mathbf{X}_0$. Using the two-body equations and a perturbed $A(t)$, we propagate $\mathbf{X}_0$ forward in time for 10 sec to generate a state $\mathbf{X}_{10}$ and $\Phi(10, 0)$. In a second execution of the integrator, we propagate $\mathbf{X}_0' = \mathbf{X}_0 + \Delta\mathbf{x}_0$ to get $\mathbf{X}_{10}'$. We provide more information on the selection of $\Delta\mathbf{x}_0$ below. We map $\Delta\mathbf{x}_0$ forward using $\Phi(10, 0)$, and calculate the error in the deviation vector (computed via the state transition matrix) using

$$\delta\mathbf{x}_{10} = \Phi(10, 0)\Delta\mathbf{x}_0 - (\mathbf{X}_{10}' - \mathbf{X}_{10}), \tag{6.10}$$

where $\mathbf{X}_{10}' - \mathbf{X}_{10}$ describes the true propagation of the deviation vector. For a common precision of $A(t)$, we compute a mean RSS $\delta\mathbf{x}_{10}$ over 1,000 of these tests.
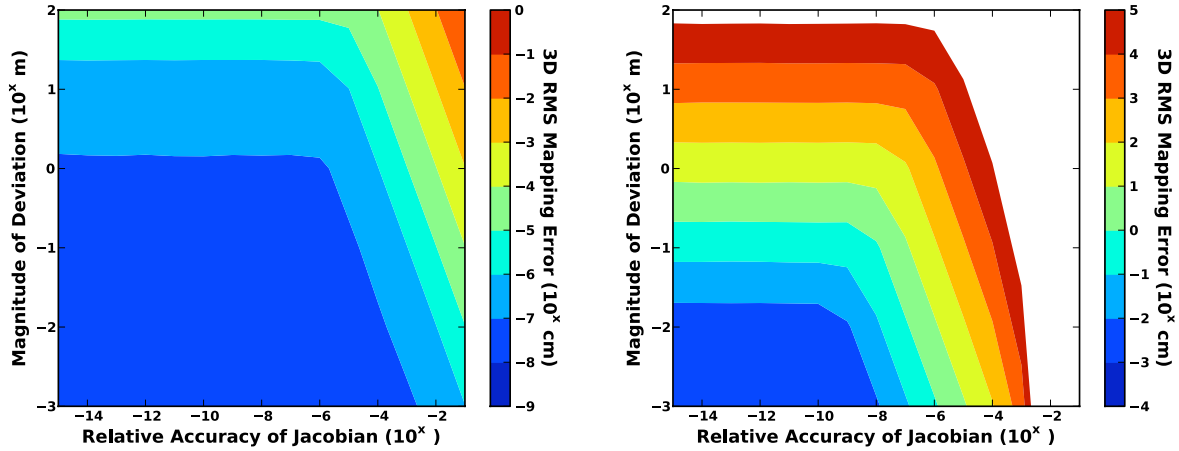
Figure 6.3: Monte Carlo analysis of errors in a deviation vector mapped via $\Phi(t, 0)$, where $t = 10$ sec (left) and $t = 86400$ sec (right), as a function of the relative accuracy of the force model Jacobian and the magnitude of the deviation vector $\Delta\mathbf{x}_0$.

We also perform this test for different deviation vector magnitudes. When generating a deviation vector $\Delta\mathbf{x}_0$, we randomly select an azimuth and elevation angle (relative to the inertial

frame), and combine this direction with a given magnitude to generate an initial deviation in the position vector. We perform this process again to generate a velocity perturbation, but scale the magnitude by 1/100. The position and velocity deviation vectors combine to form a full deviation $\Delta\mathbf{x}_0$.

Figure 6.3 illustrates the 3D RMS errors in mapping a deviation vector using $\Phi(t, t_\circ)$ in the test previously described. The precision of the Jacobian indicates the relative accuracy of the $A(t)$ used for propagating the state transition matrix. For this relatively small time interval of 10 sec, errors in $A(t)$, and thus $\Phi(t, t_\circ)$, weakly affect errors in the mapping of $\Delta\mathbf{x}_0$. Increasing the accuracy of the Jacobian beyond six digits, i.e. a precision less than 10^{-6}, demonstrates a negligible reduction in errors.

The second plot in Figure 6.3 provides results for the same test, but with the propagation time increased from 10 sec to 1 day. In this case, we see a larger variation in the mapping accuracy. For precise orbit determination, i.e. systems with deviation-vector magnitudes closer to 1 to 10 cm, accuracy beyond ten digits yields little improvement. We typically do not use a state transition matrix that maps over such a large time interval in sequential orbit determination. Such capabilities are usually required for batch processing, i.e. simultaneous processing of observations over a large time interval.

We now assess the precision of the state transition matrix computed via the cubed-sphere model when compared to solutions using the spherical harmonic model. For this process, we use a procedure similar to that of Section 5.2 for the CS-34, CS-100, CS-174, and CS-198C cubed-sphere models. We use CD to quantify the differences in $\Phi(t, t_\circ)$. In this case, $\Phi(t, t_\circ)$ is a 6×6 matrix containing values of multiple magnitudes and different units. Given these characteristics, we measure precision by Equation 4.2 instead of an absolute value, e.g. m/s^2. Additionally, instead of providing 36 values of CD at each point in time, we average over all 36 values at all times for a given altitude.

We generate cubed-sphere models representing the terms of the Jacobian using the parameters provided in Table 6.1. Using the same model configuration for representing the gravity acceleration

and its Jacobian yields a faster evaluation, i.e. reducing the number of duplicate evaluations. We note that differentiation reduces accuracy by 1-2 digits. If we require a Jacobian accurate to 14 digits, like the acceleration, then we must reconfigure the models to achieve this accuracy. As demonstrated in Figure 6.3, we do not require an $A(t)$ matrix this accurate.
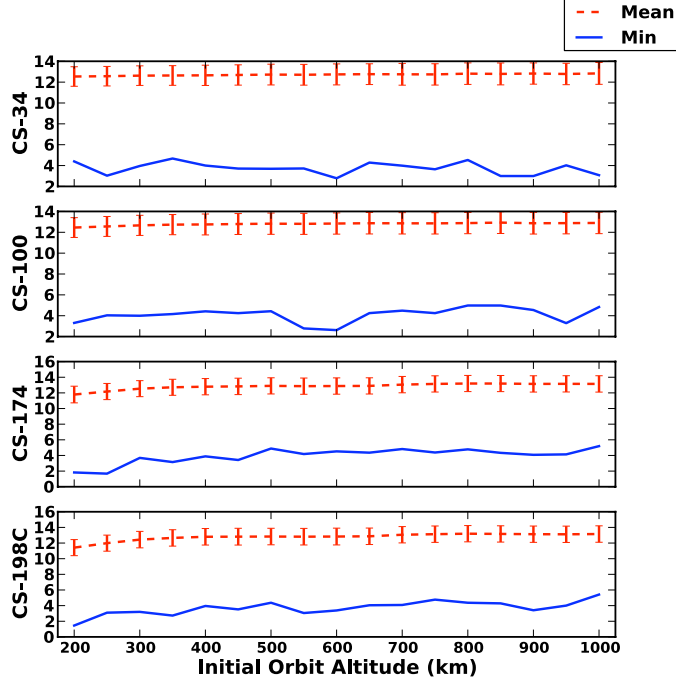
Figure 6.4: Precision, in CD, of the state transition matrix computed using the CS-34, CS-100, CS-174, and CS-198C cubed-sphere gravity models when compared to those computed via the spherical harmonic base model. Provided statistics include the mean precision with 1-σ error bars and the minimum precision.

Figure 6.4 illustrates the mean precision, with 1-σ error bars, of the cubed-sphere model derived elements of $\Phi(t_i, t_0)$ with compared to those of the corresponding base model. Results demonstrate 12 to 13 digits of precision for altitudes at or above 300 km, with standard deviations of approximately 1 digit. Minimum values appear small, however values with low precision correspond to values with a small magnitude. Thus, their contribution to the mapping of P_i is small.

We provide the 3D RMS position and velocity errors for these tests in Figure 6.5. Like results of the previous chapter, position errors remain sub-millimeter, and decrease slightly with altitude.

This extends conclusions from the previous chapter to models of degree 200, i.e. the cubed-sphere model is capable of representing a 200×200 spherical harmonic model with little or no difference in propagated trajectories.

We note that these $\Phi(t_i, t_0)$ results affect a batch filter more than a sequential filter. In the sequential algorithm, like the CKF and EKF, we integrate from t_{i-1} to t_i. In such a process, we use the initial condition $\Phi(t_{i-1}, t_{i-1}) = \mathbb{I}_{n\times n}$ with each execution of the integration algorithm. Thus, differences in $\Phi(t_i, t_{i-1})$ when computed via the cubed-sphere and spherical harmonic model are removed with each filter time update. However, batch methods like the least squares algorithm in Section 3.2 require $\Phi(t_i, t_\circ)$, with differences accumulating.
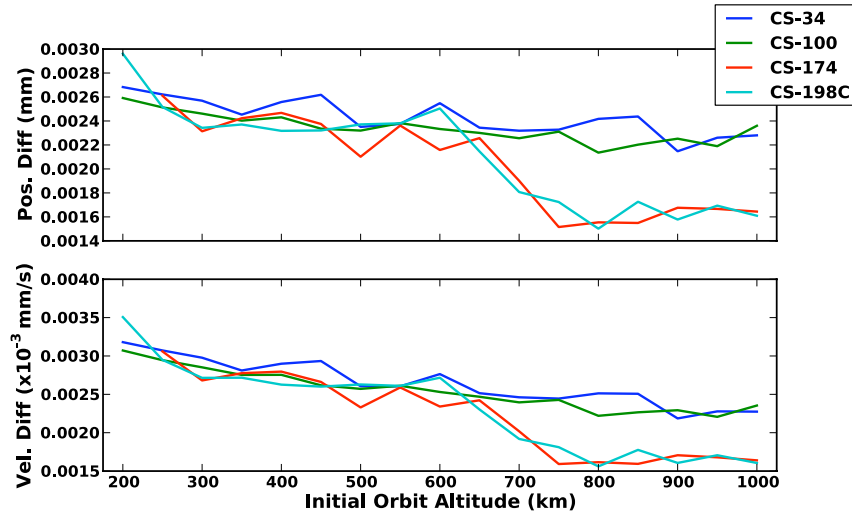
Figure 6.5: Summary of orbit propagation 3D RMS state differences for the CS-34, CS-100, CS-174, and CS-198C cubed-sphere gravity models when compared to trajectories computed with the corresponding spherical harmonic model

6.4   Filter Test Description

We consider scenarios based on satellites at three different orbit altitudes for this study: the Ocean Surface Topography Mission (OSTM)/Jason-2 (Lambin et al., 2010), the Gravity Recovery and Climate Experiment (GRACE) (Tapley et al., 2004a), and a GPS Satellite (ARINC Engineering

Services, 2004). The GRACE satellite orbits at an altitude of approximately 485 km, while the Jason-2 satellite has a higher orbit at ∼1,336 km. Orbit determination systems for these two satellites require a fairly high degree model (Bertiger et al., 2010; Kang et al., 2006). In the case of GRACE, the orbit altitude is low enough to aid in estimating the gravity field to degree 200. GPS satellites orbit at roughly 20,500 km, thus high-degree models are not required. However, we consider this satellite since current efforts seek to generate near real-time orbit determination solutions for the GPS constellation (Weiss et al., 2010). To prevent confusion with GPS-based observations of the Jason-2 and GRACE satellites (see measurement description below), we refer to the satellite in the final scenario as a semi-synchronous, or SemiSync, satellite. A semi-synchronous satellite has a 12 hour period.

Table 6.2: Initial conditions for the simulated Jason-2, GRACE, and SemiSync satellites

Element	Jason-2	GRACE	SemiSync
Semimajor Axis (km)	7714.1363	6863.1363	26559.8
Eccentricity	0.01	0.0	0.01
Inclination (deg)	66.0	89.0	55.0
Right Ascension of Ascending Node (deg)	61.662	80.690	272.85
Argument of Perigee (deg)	149.654	357.069	0.0
True Anomaly (deg)	178.548	15.869	11.68

We generate "truth" orbits for each satellite using the most accurate satellite force models available at the time of this research. For gravity, we use the full GGM02C (Tapley et al., 2005) 200×200 spherical harmonic gravity model. The Jacchia-Bowman 2008 (JB2008) (Bowman et al., 2008) model provides the most realistic representation of atmospheric density available. We use the TurboProp RK5(4) numerical integration tools (Hill and Jones, 2009) for both generation of the true trajectories and within the filters themselves. To generate a higher drag perturbation, we select a simulation epoch time of July 14, 2000 00:00:00 UTC, which corresponds to a solar maximum. Using these force models and the initial states provided in Table 6.2, we propagate forward 24 hours to a final time of July 15, 2000 00:00:00 UTC.

Table 6.3 describes the a priori and modeling errors included in these scenarios. We assume

Table 6.3: Summary of filter error sources. Truth$+\sigma$ means true value plus zero mean, 1-σ Gaussian noise. Sigma values are provided where appropriate.

Element	Truth Value	Filter Value
Initial Position	True Position	Truth + 1-σ, $\sigma = 0.01$ km
Initial Velocity	True Velocity	Truth + 1-σ, $\sigma = 0.001$ km/s
Initial C_D	2.3	2.0
Gravity Estimate	GGM02C	1-σ clone of GGM02C
Gravity Model Degree	200×200	Test dependent
Atmospheric Density Model	JB2008	NRLMSISE-00
GPS Satellite	True Position	Truth + periodic error ($\sigma = 2.8$ cm)
SLR/DORIS Station	True Position	Truth + 1-σ, $\sigma = 2$ cm

a reasonably accurate a priori solution, which primarily affects filter settling time and not overall accuracy. The NRLMSISE-00 atmospheric density model does not incorporate the latest advancements in space weather modeling; hence its reduced accuracy when compared to the JB2008 model. We model errors in the estimated gravity field using 1-σ gravity clones, which we explain in more detail below. Using each of the models in Table 6.1, we vary the truncation of the filter gravity model with each test to assess computational improvement as a function of degree. To simulate errors in the location of the measurement reference station or GPS ephemeris, we add additional errors in the filter models. We add Gaussian noise with zero mean and a standard deviation of 2 cm to the filter estimate of the ground station locations. The filter modeled GPS satellite position includes a 2.8 cm 1-σ error in each component direction. This corresponds to the estimated 5 cm RSS position error of the IGS ultra-rapid ephemeris (Dow et al., 2009). To model the 15 minute sampling period provided by the IGS solution, we make the GPS position error periodic with a $2\pi/15$-minute frequency and a random phase offset. Thus, the maximum possible measurement bias is 5 cm and never drops to 0 cm. We note that the intention of this research is to study computation improvements and relative precision, and not the absolute accuracy of the orbit determination process. However, we include these errors to increase the realism of the test.

Gravity clones allow for the incorporation of statistical uncertainty, i.e. the gravity model

estimate covariance matrix, in Monte-Carlo-like tests. Given

$$P_{\bar{C}S_{nm}} = S^T S, \tag{6.11}$$

where S is upper triangular and computed via the Cholesky decomposition, we may generate a gravity clone

$$\text{Clone} = \bar{C}S_{nm} + S\vec{e} \tag{6.12}$$

where $\bar{C}S_{nm}$ is a vector of the Stokes coefficients describing the spherical harmonics gravity model, $P_{\bar{C}S_{nm}}$ is the full estimation error covariance matrix of the Stokes coefficients, and $\vec{e}$ is a vector of random numbers with zero mean and unit variance.

We generate five 1-σ gravity clones using the publicly available portion of the GGM02C spherical harmonic model covariance matrix. The University of Texas Center for Space Research (CSR) only releases the diagonal terms of the GGM02C covariance matrix, but indicates that correlations are small. Given this reduced $P_{\bar{C}S_{nm}}$, we do not generate true clones, but, likely, a conservative representation of the gravity errors. We generate corresponding cubed sphere representations of these clone models using the configurations of Table 6.1. We use each clone in the orbit determination process, and average absolute filter errors to generate an error incorporating uncertainty in the gravity field.

For these filter tests, we consider the measurement types: Earth-based range observations, Earth-based range-rate, and satellite-based range. These systems approximate observations from the Satellite Laser Ranging (SLR) (Pearlman et al., 2002), Doppler Orbitography and Radiopositioning Integrated by Satellite (DORIS) (Tavernier et al., 2006), and Global Positioning System (GPS) services, respectively. We base locations of the SLR[2] and DORIS[3] ground stations on the actual network. The simulated GPS satellite constellation uses the optimal 24 satellite design described by Massatt and Zeitzew (1998). Using the true satellite trajectory, we generate simulated observations relative to the measurement reference point, and then add Gaussian noise. For the GRACE and Jason-2 scenarios, we provide measurements, when available, every 10 sec. For the

---

[2] http://ilrs.gsfc.nasa.gov/stations/index.html, Retrieved August 7, 2008
[3] http://ids.cls.fr/html/doris/network.html, Retrieved August 7, 2008

SemiSync scenario, we reduce this to every minute. More accurate measurement types are available, such as GPS carrier phase, but they often require additional processing. The goal of this research is to characterize computation improvements for systems requiring fast orbit determination algorithms and high-degree gravity models. Thus, we do not consider measurement types requiring additional computational resources.

Table 6.4: Observation Noise Properties

Measurement	Gaussian Measurement Noise	Filter Observation σ
GPS Pseudorange	1 m	1.002 m
SLR Range	5 mm	4 cm
DORIS Doppler	2 mm/s	1 cm/s

We provide simulated observation properties in Table 6.4. We do not estimate the measurement reference locations; thus, the filter must compensate for the station location error as a measurement error. We select the filter observation σ value to yield a normal distribution of prefit-residual errors in filter processing, i.e. the differences between the filter predicted observations and the provided observations were normally distributed with zero mean and a standard deviation approximately equal to the filter observation σ value. Thus, the filter observation σ value also accounts for errors in the locations of the GPS satellites and ground stations.

In Figure 6.6, we provide the process noise σ_Q for each of the filter tests, and use the same values in both the EKF and UKF. As mentioned previously, we select these values to yield filter errors that agree with the filter state-error covariance matrix. We verified the proper tuning of the filter process noise by comparing the filter estimated 1-σ error to the actual measurement 1-σ error. Values were approximately equal, implying measurement noise accounts for the demonstrated filter errors. Further changes in process noise will not necessarily improve filter accuracy. With a higher measurement error, we expect an increased state error. When coupled with errors in the filter force model, this induces more error in the time-updated filter state. Thus, do to the larger measurement error, we require a larger process noise σ_Q for the GPS pseudorange scenarios. Given the lower altitude of the GRACE satellite, the increased magnitude of the gravity model error requires an

even larger σ_Q. Process noise for the SemiSync satellite is virtually zero because of its high-altitude orbit, which reduces the effects of both gravity and atmospheric density modeling errors.
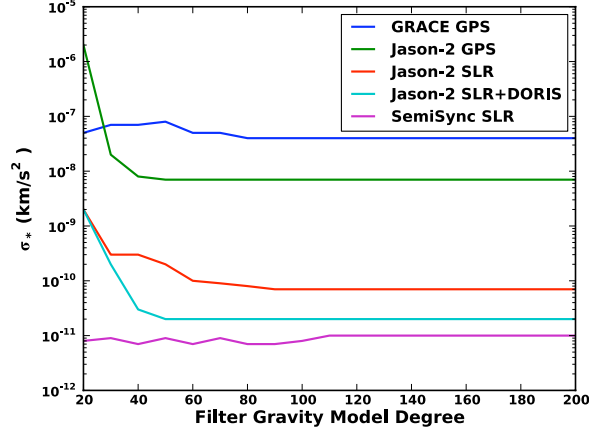
Figure 6.6: Filter process noise σ_Q values.

6.5   Orbit Determination Results

6.5.1   Filter Execution Time Considerations

In this section, we discuss the two principle elements affecting the execution time of the EKF and UKF: the time and measurement updates. We use results of this section to understand the filter speedup results in Section 6.5.2.

Figure 6.7 illustrates the integration speedup when using the cubed-sphere model instead of the spherical harmonic model. Like the tests of Chapter 5, we propagate an initial condition using both the cubed-sphere and spherical harmonic models, then compute an orbit propagation speedup factor. For each gravity model degree, we perform this test 30 times and compute the average speedup. In the single-state results, we integrate the position and velocity of a single satellite for 24 hours. The UKF-like integration propagates 13 satellite state vectors, and reflects the integration speedup for our implementation of the cubed-sphere model in the UKF. Finally, the third plot describes the speedup when integrating one satellite state vector and the state transition

matrix. The matrix operations in this third test, which have not yet been fully optimized within TurboProp (Hill and Jones, 2009), increase the fixed cost of evaluating the force model; thus, the speedup factor decreases.
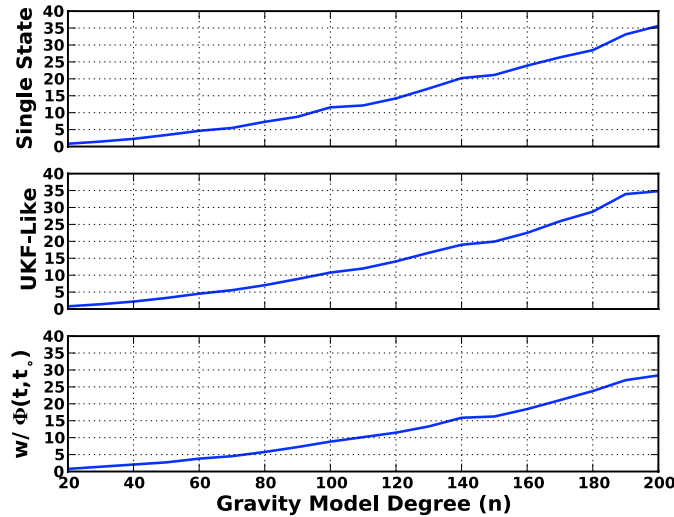
Figure 6.7: Speedup factors when using the cubed-sphere model, as opposed to the spherical harmonic model, for propagation. The second and third plots describe the speedup for integration methods used in the UKF and EKF filters, respectively.

The single-state results in Figure 6.7 reflect a change in the computer used for testing. In Chapter 5, the CS-162 model provided approximately 30-times faster integration than when using the 150×150 spherical harmonic model. In Figure 6.7, the speedup factor when using the CS-174 model is around 21. Instead of averaging over results from multiple computers like the previous test, we perform these experiments on the CCAR computer Cheetah, which provides the fastest evaluation of the spherical harmonic model. Thus, they represent a conservative assessment of integration speedup. We use this same computer for all future speed performance tests.

For Figure 6.8, we duplicate the methods of Figure 6.7, but include the NRLMSISE-00 atmospheric density model and compute the drag acceleration in the satellite dynamics. Including the density decreases the percentage of the overall computation cost associated with the gravity model. As a result, we expect integration speedup factors to decrease. However, the percentage

decrease is not as large for integration with the state transition matrix due to the required matrix operations.
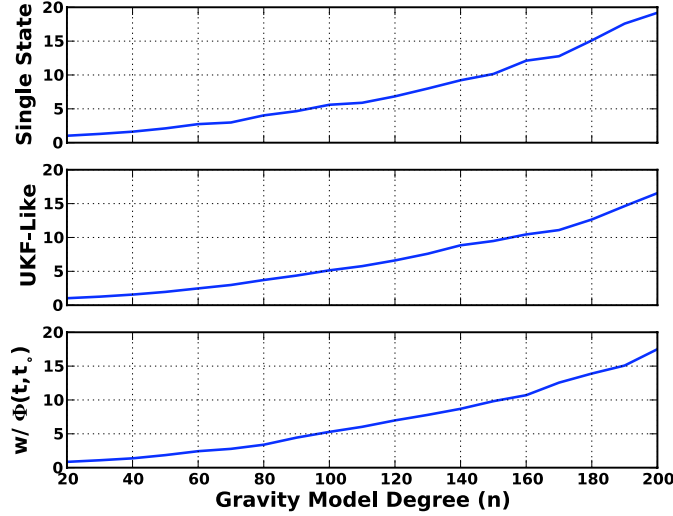
Figure 6.8: Speedup factors when using the cubed-sphere and NRLMSISE-00 density models for propagation. This includes speedup factors for orbit propagation methods used in the UKF and EKF filters.

To gain some analytic insight into the affect of reduced time update computation time on orbit determination efficiency, we generate an approximation of the filter speedup S_F based on the measurement update evaluation time T_M and orbit propagation speedup factors S_I. We separate the filter execution time into a sum of the time and measurement updates, and write the filter speedup factor

$$S_F = \frac{T_{SH} + T_M}{T_{CS} + T_M},$$
(6.13)

where T_{SH} and T_{CS} are the evaluation times of the time update using the spherical harmonic model and the cubed-sphere model, respectively. We assume a constant T_{CS} for all cubed-sphere models, and that T_M does not vary between the cubed-sphere and spherical harmonic model tests. Upon representing time in units of T_{CS}, we write

$$S_F \approx \frac{S_I + \tilde{T}_M}{1 + \tilde{T}_M}$$
(6.14)

where

$$\frac{T_{SH}}{T_{CS}} \approx S_I, \tag{6.15}$$

and $\tilde{T}_M = T_M/T_{CS}$. Although integration dominates the execution of the time update, other operations add some computation cost. Hence, Equation 6.15 is an approximation. We now have an estimate of the filter speedup as a function of the measurement update evaluation time, normalized by T_{CS}, and the integration speedup. Figure 6.9 illustrates the filter speedup predicted by Equation 6.14, and indicates that, for the integration speedup factors provided in Figure 6.8, we require an efficient measurement update to achieve large gains in filter efficiency.

Table 6.5 includes statistics on the average time between observations and the average number of observations per measurement update for the five filter scenarios. These statistics influence the time required for measurement processing. For the scenarios using GPS measurements, there are no data gaps. For the Jason-2 SLR scenario, relatively large data gaps raise the average time between observations by almost a factor of two. We process more observations in the SemiSync SLR scenario than all others due to its high altitude, i.e. the high altitude makes the satellite visible to a large number of ground stations for longer periods of time.
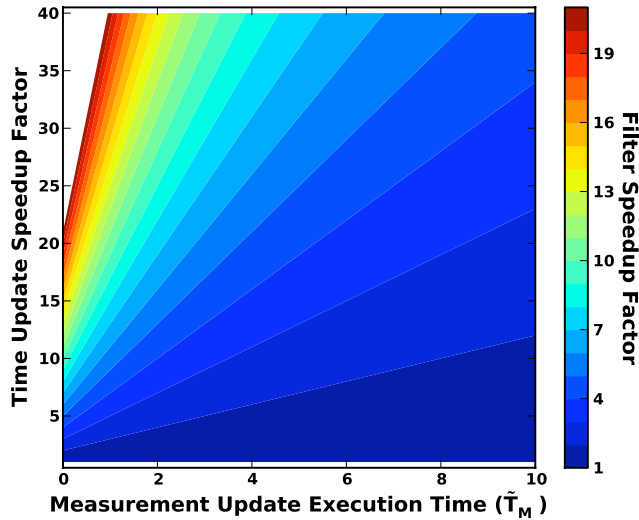
Figure 6.9: Predicted filter speedup factors as predicted by Equation 6.14.

Table 6.5: Observation Statistics for Each Simulation

Scenario	Average Data Gap (sec)	Average Number of Obs
GRACE GPS	10	11.3
Jason-2 GPS	10	11.0
Jason-2 SLR	17.5	4.9
Jason-2 SLR+DORIS	10.5	6.4
SemiSync SLR	60	17.5

In Figure 6.10, we provide the values of $\tilde{T}_M$ for all simulations. $\tilde{T}_M$ values decrease slightly for higher degree, corresponding to increasing T_{CS}, but remain approximately constant for each scenario. These results, in combination with Figure 6.9, imply that SLR simulations will yield the largest filter speedup factor. For this case, data gaps increase the average T_{CS}, thus decreasing $\tilde{T}_M$ while preserving S_I. Inclusion of the DORIS data reduces the data gaps and increases the number of observations processed per measurement update; hence, $\tilde{T}_M$ increases. The SemiSync scenarios have the largest measurement update evaluation time given the large number of observations. Normalized measurement processing time for the EKF increases because the time required for integration decreases with fewer states, i.e. integration of $n(2n+1)$ elements in the UKF versus $n(n+1)$ in the EKF, where n is the number elements in the satellite state vector.
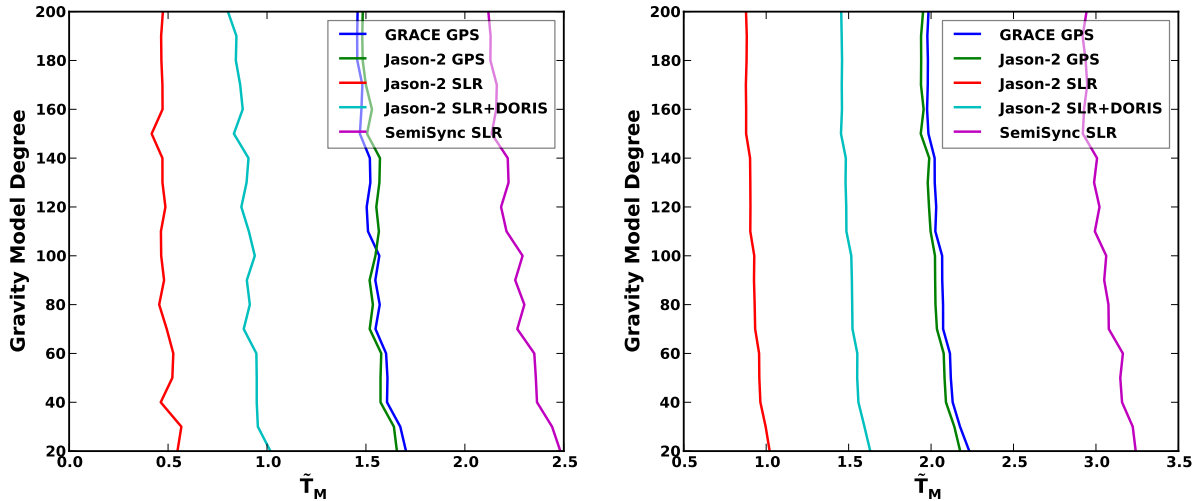
Figure 6.10: Measurement update evaluation times, in $\tilde{T}_M$, for all UKF (left) and EKF (right) simulations. We place $\tilde{T}_M$ on the x-axis to facilitate comparison with Figure 6.14.

6.5.2 Filter Execution Time Results

Figure 6.11 illustrates the speedup factors for the EKF and UKF. As implied by Figure 6.10, speedup factors vary with the filter and scenario. As a result of the relatively low $\tilde{T}_M$, processing of SLR measurements in the Jason-2 scenario exhibits the largest benefit when using the cubed-sphere model. Filter speedup does not reach the levels of the orbit propagation speedup factors. Further improvements will require a more efficient measurement update implementation.
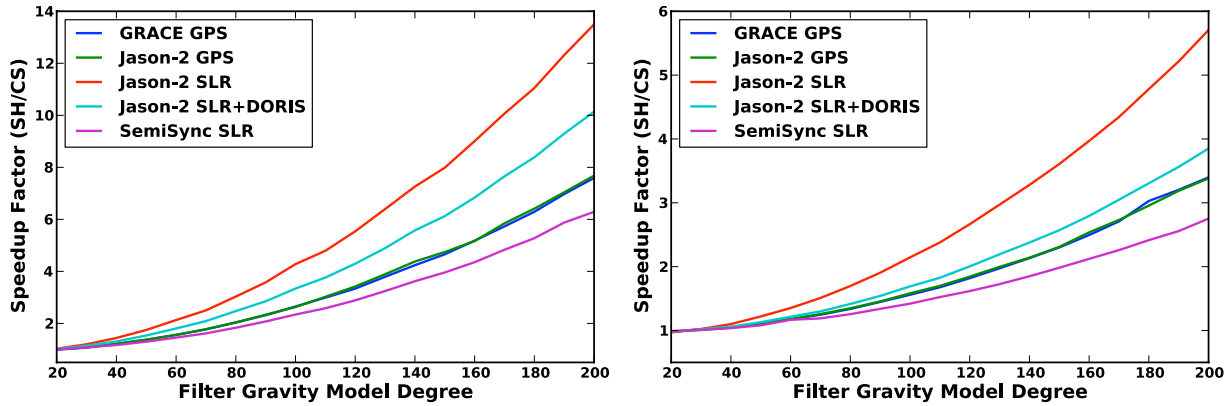
Figure 6.11: Filter speedup factors for the UKF (left) and EKF (right) simulations.
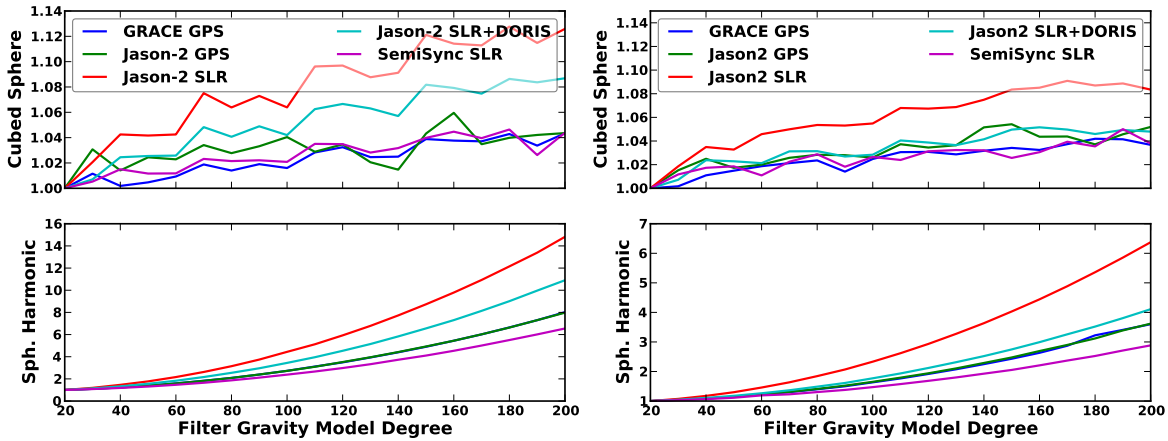
Figure 6.12: Change in filter execution times for the UKF (left) and EKF (right) simulation. We demonstrate this change by normalizing all execution times by the time required to complete the corresponding 20×20 scenario.

In Figure 6.12 we provide the filter execution time normalized to the execution time of the
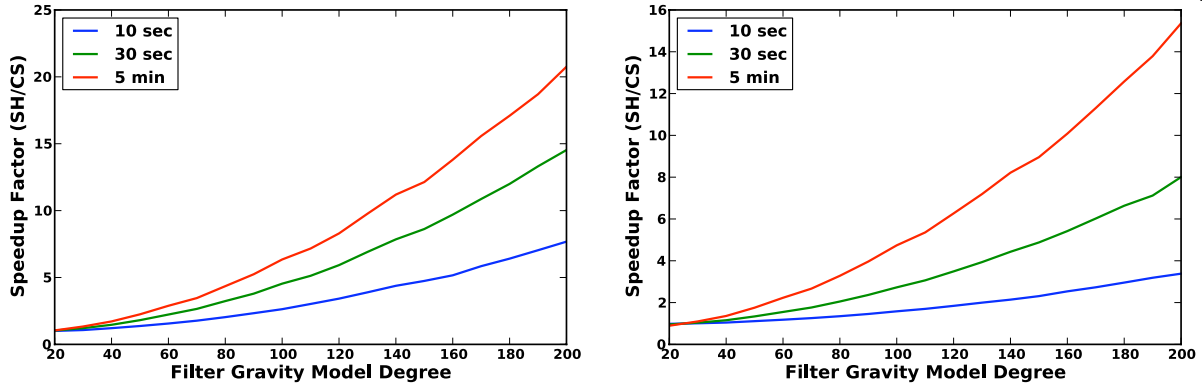
Figure 6.13: Speedup factors for the Jason-2 satellite using GPS observations provided at different rates in the UKF (left) and EKF (right).

20×20 model, which illustrates the change in filter execution with increasing gravity model degree. For the cubed-sphere model, only the degree of the Chebyshev interpolation increases with the degree of the base model, thus slightly increasing the computation time. Execution time for filters using the cubed-sphere-model filter increases by a factor of 1.14, whereas the spherical-harmonic-model filter increases by as much as a factor of 15 for the UKF. Thus, assuming an increase in integrator memory requirements is acceptable, a filter may use a higher-degree gravity model with little additional computation cost.

For Jason-2 precise orbit determination, the NASA Jet Propulsion Laboratory processes GPS normal points every 5 minutes, but may change to every 30 sec.[4] For Figure 6.13, we process GPS observations at these reduced frequencies, and illustrate the increased speedup factors for the Jason-2 satellite. With the increased orbit propagation time required for these longer intervals, the filter speedup factor improves. JPL uses a square-root information filter for Jason-2 orbit determination, which is closer to the EKF than the UKF. For this test, the EKF integrator speed increases by almost a factor of 5 for the 5 min scenario, and 2.5 for the 30 sec test.

Figure 6.14 illustrates the ratio of the execution times for the UKF with the cubed-sphere model and the EKF with the spherical harmonic model. Although the UKF includes higher-order dynamics in the propagation of the estimated-state covariance matrix, the additional computation

---

[4] Personal communication with Shailen Desai of the NASA Jet Propulsion Laboratory

cost limits its use. Assuming a given system allows for orbit determination with a high-degree spherical harmonic model, we seek to determine the cost of switching to an UKF with the cubed-sphere model. The figure indicates that such a switch may be possible, with little or no additional computation cost, for systems using high-degree models and larger data gaps. In the case of the Jason-2 satellite with a model of degree 180 or higher, using an UKF with the cubed-sphere model provides faster orbit determination than the EKF with the spherical harmonic model. Otherwise, for high-degree models, orbit determination with a 200×200 model in the UKF requires a maximum of 50% more computational resources when compared to using the spherical harmonic model in the EKF.
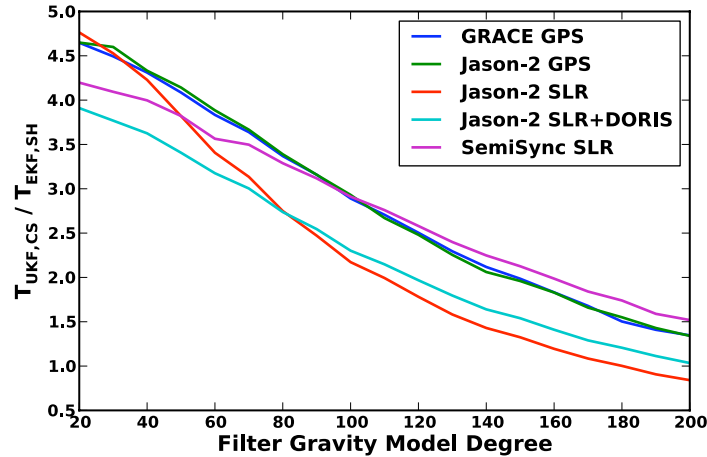
Figure 6.14: Execution time of the UKF with the cubed-sphere model, when normalized by the execution time for the EKF with the spherical harmonic model.

6.5.3   Filter Precision

In this section, we discuss differences between filter solutions generated with the cubed-sphere model and those using the spherical harmonic model. First, we provide a short treatment of absolute accuracy for the GRACE and Jason-2 scenarios, but only to provide a sense of scale for later results. We do not provide plots of the absolute accuracy for the SemiSync satellites with model degree. Given the large altitude, no improvement is exhibited for higher degree models,

and all 3D RMS position and velocity errors remain accurate to approximately 9.64 cm and 0.013 mm/s, respectively. Then, we discuss changes in the filter estimated state when using different gravity formulations.

Figure 6.15 illustrates the absolute accuracy of the filters in the GRACE and Jason-2 scenarios. We note that errors decrease with increased gravity model degree, with GRACE errors decreasing until degree 80 and Jason-2 accuracy improving to degree 50. This indicates the principle source of estimation error using the low-degree models is gravity truncation. In position, the filter performance improves by as little as a factor of 2 when using a gravity model of higher-degree, and velocity errors are reduced by almost an order of magnitude.
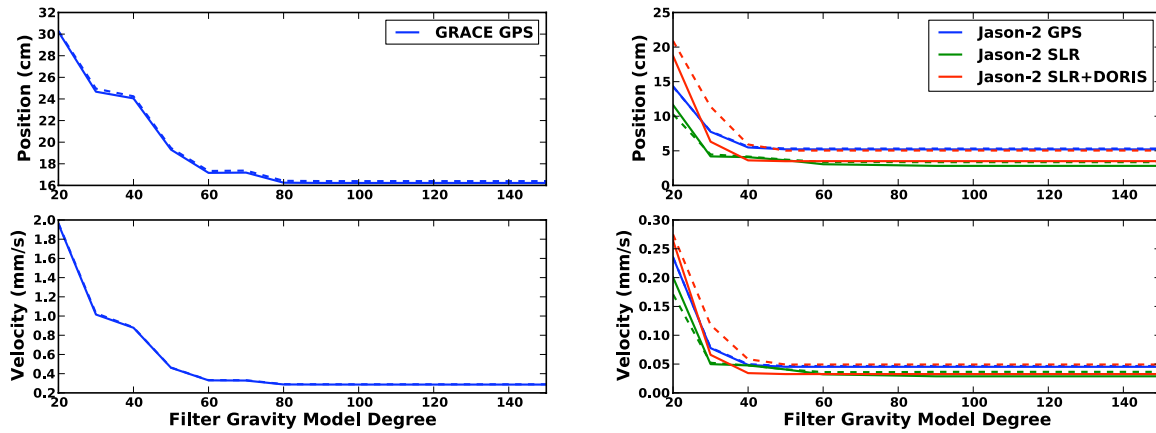
Figure 6.15: 3D RMS filter performance for the GRACE (left) and Jason-2 (right) scenarios. Solid and dashed lines correspond to UKF and EKF results, respectively.

In Figure 6.16, we provide the 3D RMS difference between the EKF scenarios using the cubed-sphere and the spherical harmonic models. We calculate these 3D RMS values using all differences for all gravity clones for a given gravity model degree. Given a filter accuracy on the order of centimeters, these results demonstrate little deviation between the two filters. We do see smaller differences for the GRACE and Jason-2 GPS scenarios, which we attribute to larger process noise, i.e. an increased weighting of observations in the filter solution of Equation 3.30 and 3.45. Therefore, with a larger process noise matrix, we decrease the contribution of the system dynamics in the filter estimated state, and, thus, lessen differences cause by the two gravity models.

Conversely, with less process noise, the filter places more weight on the force model in estimating the state, thus failing to reduce differences created by slight variations in the force model. We note that several 3D RMS values for the SemiSync satellite are effectively zero, i.e. any differences remain less than the floating point error. Hence, they are not visible on this logarithmic plot.
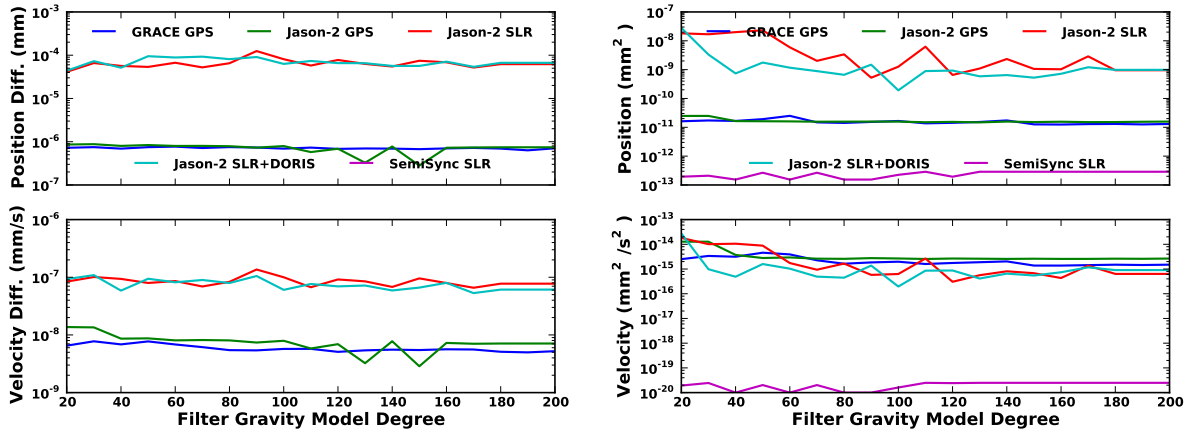
Figure 6.16: 3D RMS differences between EKF solutions (left) and covariance matrices (right) computed with the cubed-sphere and spherical harmonics models.

Also in Figure 6.16, we provide RMS differences of the diagonal elements of the covariance matrix, i.e. the the filter's estimated-state variances. We see similar deviations in these variances, i.e. the variances in the SLR and DORIS scenarios are greater than the GPS scenarios, except in the case of velocity. In this latter case, differences are within 1-2 orders of magnitude.

Figure 6.17 illustrates the differences between the cubed-sphere- and spherical-harmonic-based solutions using the UKF. Typically, differences for the SLR and DORIS scenarios remain larger. We note that the differences between the cubed-sphere- and spherical-harmonic-based filters using GPS measurements increase by an order of magnitude when compared to the differences for the EKF. In the case of the SLR and DORIS scenarios, the more accurate measurements negate this fact.

As seen when comparing Figures 6.16 and 6.17, state-error covariance matrix deviations for the UKF increase by as much as eight digits when compared to those of the EKF. The UKF includes second, and possibly third, order effects in the propagation of the covariance matrix. Small

deviations in the σ-points yield larger differences in these higher orders, which reduce the precision between the covariance matrices generated when performing a time update via the cubed-sphere versus the spherical harmonic model. Given state-error covariance values on the order of 10^5 or 10^6 mm^2, the resulting covariance matrices still agree to at least seven 7 digits. However, we do not, typically, require such accuracy of the state-error covariance matrix. Tests demonstrate that increasing the α value in the UKF (see Section 3.3.2), reduces the magnitude of these UKF differences, and decreasing it increases the differences. Increasing α reduces the contribution of the σ-points in calculating the time updated $\bar{P}_i$; thus, the small differences in the propagated σ-points no longer influence the filter. We recommend that this phenomenon be further explored to verify this interpretation.
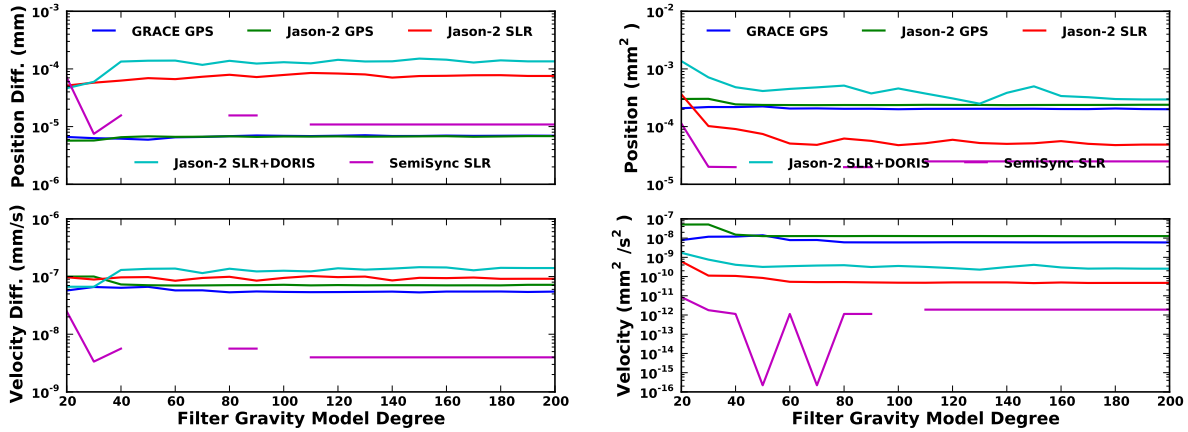
Figure 6.17: 3D RMS differences between UKF solutions (left) and covariance matrices (right) computed with the cubed-sphere and spherical harmonics models.

6.6 Chapter Summary

In this chapter, we integrated the cubed-sphere model with both an EKF and UKF. Models included in this test were designed for optimal precision with the base model. We used these new filter configurations to demonstrate that orbit determination with the cubed-sphere model yields computation improvement with little difference in the estimated state. The state differences themselves are dependent on the process noise included in the filter. However, all results demonstrate

state differences several orders of magnitude below the best orbit determination capabilities available today. Scenarios using GPS pseudorange observations, which include a larger process noise matrix, yielded differences an order of magnitude greater when using a UKF.

We also demonstrated the propagation accuracy of a cubed-sphere-model-based state transition matrix. The trajectory propagation with the cubed-sphere model provides a highly-precise $\Phi(t_i, t_{i-1})$ when compared to those computed via the spherical harmonic model. Additionally, this test demonstrated that cubed-sphere models representing a $200{\times}200$ spherical harmonic model also yield small differences in integrated states.

Results demonstrate an improvement in computational efficiency of the orbit determination process, especially for high-degree systems. However, further improvements also required increased measurement update efficiency. Thus, while removing the computational burden of the gravity model for the orbit determination process, we require additional work to optimize both the time and measurement updates for larger computation gains.

Chapter 7

Gravity Estimation with the MRQSphere Model

In Chapters 5 and 6, we discussed the cubed-sphere gravity model, which was designed for efficient evaluation of the gravity field. Now, we shift to a model designed for gravity estimation: the Multiresolution Representation using Quadratures for the Sphere, or MRQSphere, model. Except for the orbit propagation statistics, we presented these results in Jones et al. (2010a).

In Chapters 2 and 4, we presented the MRQSphere model and the techniques employed for model configuration. In this chapter, we demonstrate the MRQSphere's estimation capabilities. We accomplish this by applying the model to the asteroid 433 Eros, and use the NEAR15A gravity model (Konopliv et al., 2002) as the true gravity field. We then define the estimation method and present results from a simulation study.

7.1   MRQSphere Model for 433 Eros

We base the configuration of a model, i.e. the stepsize h and $\mathbb{J} \subset \mathbb{Z}$, on the model accuracy requirements dictated by the accuracy of measurements (see Chapter 4). Here, we focus on a model analogous to the low-degree model generated using radiometric and landmark data from the NEAR mission to 433 Eros. This 15x15 spherical harmonic gravity model (NEAR15A) (Konopliv et al., 2002) primarily used observations of the satellite at orbits 2 Eros radii (R_E) and above, where Eros' radius is 16 km. For reference, we provide an isometric view of Eros in Figure 7.1, which we based on the radiometric shape model determined by the NEAR mission (Zuber et al., 2000). As demonstrated later, the side lobes of Eros influence accuracy results. Only the gravity

perturbations, i.e. gravity field terms of degree 2 or greater, are modeled by the MRQSphere model.
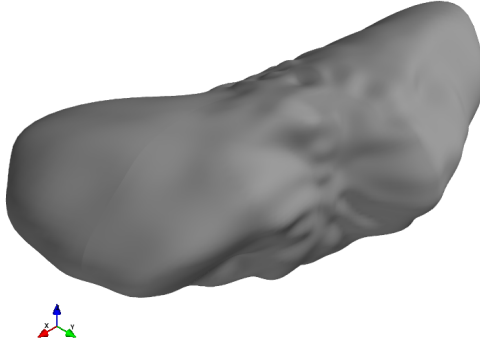
Figure 7.1: An isometric view of the asteroid 433 Eros.

Table 7.1: Configuration of the MRQSphere representation of the NEAR15A spherical harmonic model

Parameter	Value
Gaussian Stepsize (h)	0.425
Precision ϵ of approximating $\rho^{-(n+1)}$	5×10^{-10}
Relative accuracy of truncating the sum Z_j (Equation 2.100)	7 significant digits

Table 7.2: Shells required for a given range of radius (accurate to 10^{-5})

Range (in R_E)	$\mathbb{J}_{min}$	$\mathbb{J}_{max}$
Above 33.963085	-5	0
33.963085 - 17.221399	-5	1
17.221399 - 10.223156	-5	2
10.223156 - 6.437202	-5	3
6.437202 - 4.578281	-5	4
4.578281 - 3.412891	-5	5
3.412891 - 2.702480	-5	6
2.702480 - 2.244688	-5	7
2.244688 - 1.925941	-5	8

We provide the selected parameters for the NEAR15A MRQSphere model in Table 7.1. Recall that, for the MRQSphere model, we express radial distance as ρ, or units of primary body radii. When generating Figure 2.7, we began with knowledge of ρ, h, and ϵ, and used these parameters

to determine $\mathbb{J}$. Here, we instead use the procedure discussed in Section 4.2 to find ρ_k such that $|\rho^{-(n+1)} - G_{\epsilon,\mathbb{J}_k}(\rho)| < \epsilon$ when given h, ϵ, and $\mathbb{J}_k$. Using this method, we generate Table 7.2, which specifies the shells required when evaluating the MRQSphere model at a given altitude. For our MRQSphere model, 14 shells are required with indices $j = -5, \ldots, 8$ for orbit radii above 1.93 R_E. We refer to a shell with index j as "shell j."
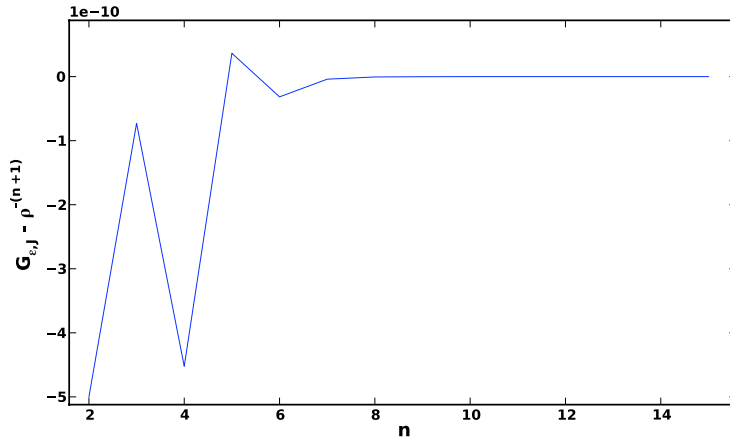
Figure 7.2: Precision (in units of 10^{-10}) of the approximation by Gaussians of $\rho^{-(n+1)}$ using shells -5 through 1 at a radius of 17.2214 R_E.

In Figure 7.2 we illustrate the precision of approximating $\rho^{-(n+1)}$ using Gaussians with the parameters shown in Table 7.1. We see in this figure that, unlike at the other altitude ranges listed in Table 7.2, the shells used at a radius slightly above 17.221399 barely meet the precision requirement of 5×10^{-10}. This influences future results, specifically, the precision of the MRQSphere model as the radius decreases towards 17.22 R_E. The upper boundary for including shell 2 may be changed to avoid this phenomenon but we have not done so intentionally.

With $\mathbb{J}_k$ and ρ_k now specified, the shell degrees, and thus the number of quadrature nodes required, may be determined. We select the number of terms in Z_j to achieve a relative accuracy of 7 significant digits and provide the resulting values in Table 7.3. Quadratures for the sphere are currently available only for particular degrees, thus, for a given j, we use the minimal number of nodes that guarantees proper integration. We denote the corresponding degree as n_{max}. Ad-

ditionally, we place an upper limit of degree 15 on the shells given that the NEAR15A model is

15×15.

Table 7.3: Required gravity field degree (n_{max}) and the number of quadrature nodes for each shell

$j \in \mathbb{J}$	n_{max}	M	$j \in \mathbb{J}$	n_{max}	M
-5	4	32	2	14	312
-4	4	32	3	15	372
-3	4	32	4	15	372
-2	7	72	5	15	372
-1	7	72	6	15	372
0	9	132	7	15	372
1	11	192	8	15	372

7.1.1   Baseline Performance

To provide a basis of comparison, and gain a more thorough understanding of the ideal performance of the MRQSphere model used for this study, we perform a set of baseline tests. The results of these tests profile the accuracy of the model given the true NEAR15A spherical harmonic model, which we used to derive the functions Z_j at the quadrature nodes for this baseline model.
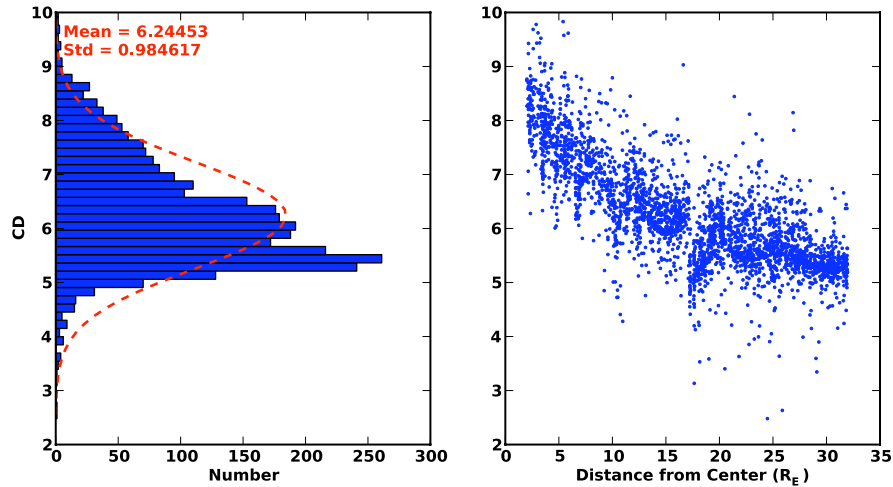
Figure 7.3: Precision of the nominal MRQSphere model with the spherical harmonic model, defined by the number of common digits between them. The figure on the right provides the distribution of accuracy with radius.

A comparison of the MRQSphere model accelerations with those of the spherical harmonic model is provided in Figure 7.3. Recall that we defined CD, the number of common digits, in Equation 4.2. In the case of acceleration, we treat each component of the vector separately. As the radius decreases, the precision improves. For a fixed absolute accuracy ϵ, which controls the approximation via Gaussians, the number of accurate digits in Equation 2.97 increases for lower altitudes. As the radius decreases towards 17 R_E, the precision deteriorates slightly. We associate this deterioration with slightly reduced accuracy at this radius as described in Figure 7.2.
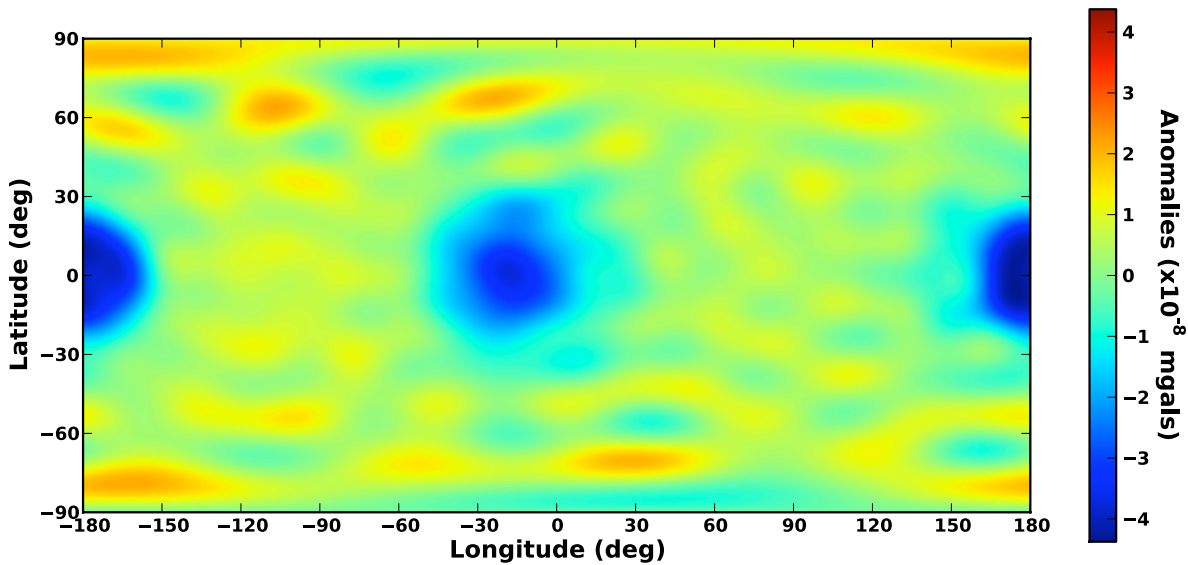
Figure 7.4: Precision of the nominal MRQSphere model and the spherical harmonics at 2 R_E.

In Figure 7.4, we illustrate the spatial distribution of gravity anomalies, when compared to the spherical harmonic model. The regions with the largest anomalies correspond to the locations of the extremal locations of the asteroid, and, thus, match the largest Bouguer anomalies. These regions of relatively large gravity variations agree with those determined by the NEAR15A model (Konopliv et al., 2002).

To characterize the Laplacian of the MRQSphere model, we provide experimental evidence that demonstrates that the error corresponds to the selected accuracy of the model. The Laplacian is evaluated via Equation 2.119 by adding the diagonal elements of the resulting 3×3 matrix. We
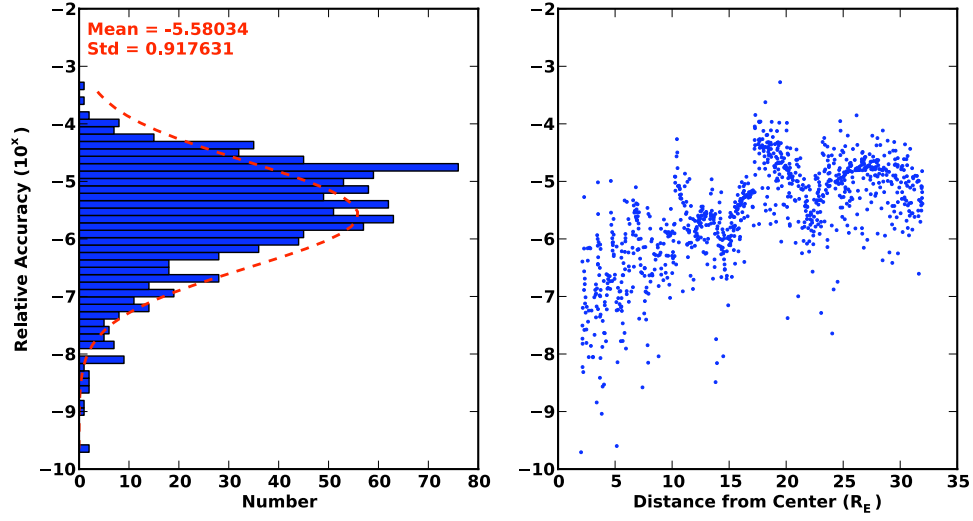
Figure 7.5: Relative accuracy of the Laplacian $(\nabla^2 \tilde{U})$ of the idealized MRQSphere model when compared to the maximum diagonal element of the variational equation matrix. The figure on the right provides the distribution of relative accuracy with radius.
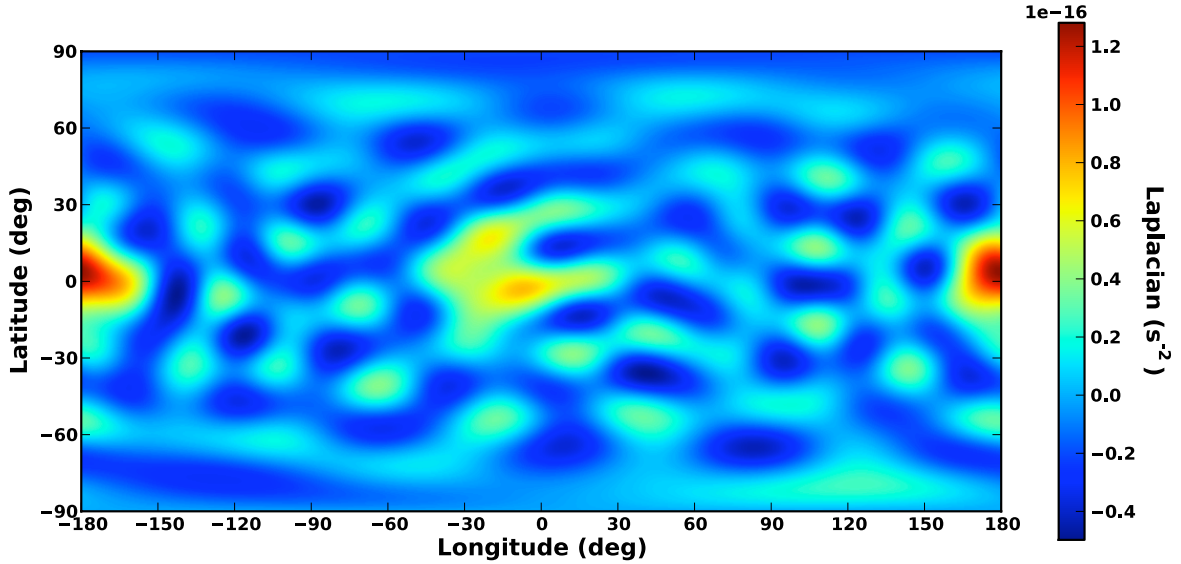
Figure 7.6: Laplacian for the nominal h=0.425 MRQSphere model at $r = 2\ R_E$

calculate the relative error between the resulting sum and the largest value on the diagonal. A histogram of the numerically computed values are included in Figure 7.5, which demonstrates the Laplacian error is approximately 10^{-5}, with a worst-case error of 10^{-3}. Similar to the accuracy of the acceleration vector, the error for the Laplacian of the model becomes smaller as altitude decreases. However, these results demonstrate increased variations in the model accuracy near the shell boundaries. This is apparent for the higher altitudes tested in Figure 7.5 where the altitude range for each shell is larger.

Figure 7.6 demonstrates that, like the acceleration vector, the Laplacian has a spatial dependence. Specifically, the regions near the side lobes of the asteroid, where gravity variations are greatest, exhibit a reduction in accuracy.
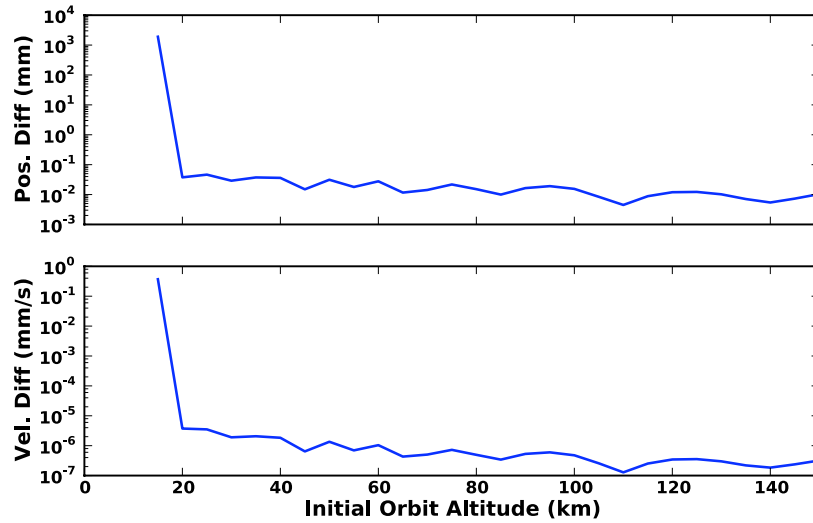
Figure 7.7: Summary of 3D RMS orbit propagation errors using the baseline MRQSphere model for Eros.

In Figure 7.7, we present the orbit propagation accuracies of the MRQSphere model. The test procedure follows that of Chapter 5, i.e. each orbit is initially circular at a given altitude with the indicated right ascension of ascending node (Ω) and inclination. For each altitude, we propagate orbits using a grid uniformly spaced in Ω and inclination. Differences are relative to
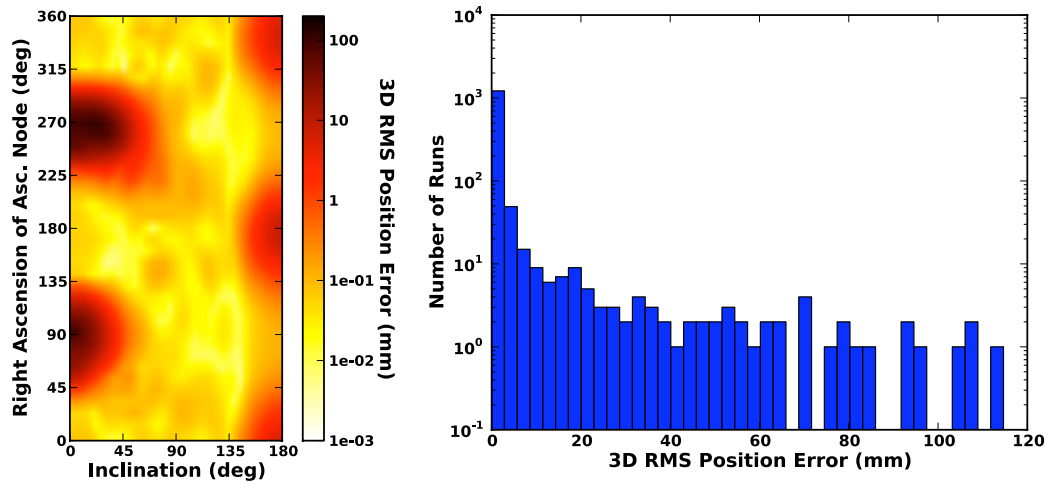
Figure 7.8: Distribution of 3D RMS differences for propagated orbits initially at 17 km with the nominal Eros MRQSphere model.
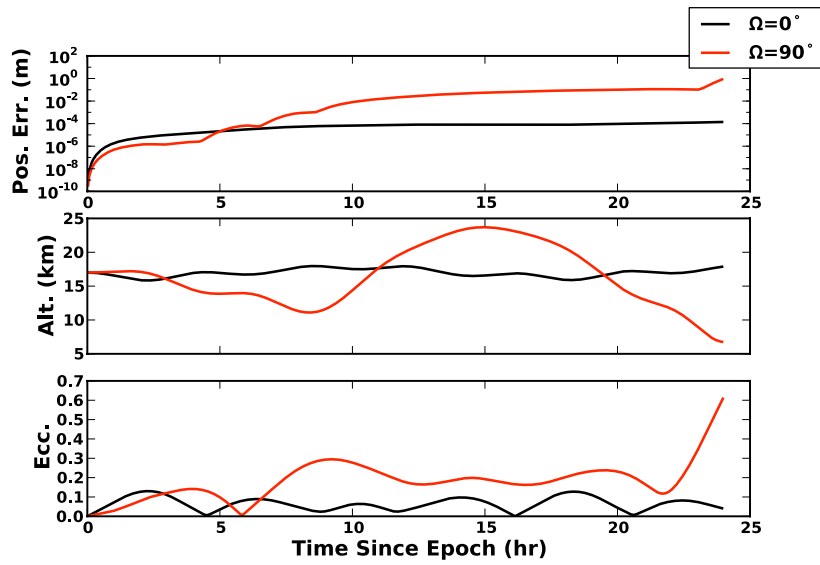
Figure 7.9: Orbit propagation properties for two equatorial orbits about 433 Eros.

orbits propagate with the NEAR15A spherical harmonic model. Results demonstrate a maximum 3D RMS orbit propagation accuracy at a fraction of a millimeter, except for orbits initially at 17 km in altitude.

In Figure 7.8, we provide detailed results for the 17 km orbits. We note that the y-axis of the histogram is logarithmic. As indicated by the contour plot, equatorial orbits result in the largest error. Further investigation demonstrates that interactions with the lobes of Eros cause a decrease in altitude to a region below the valid altitude range of this MRQSphere model.
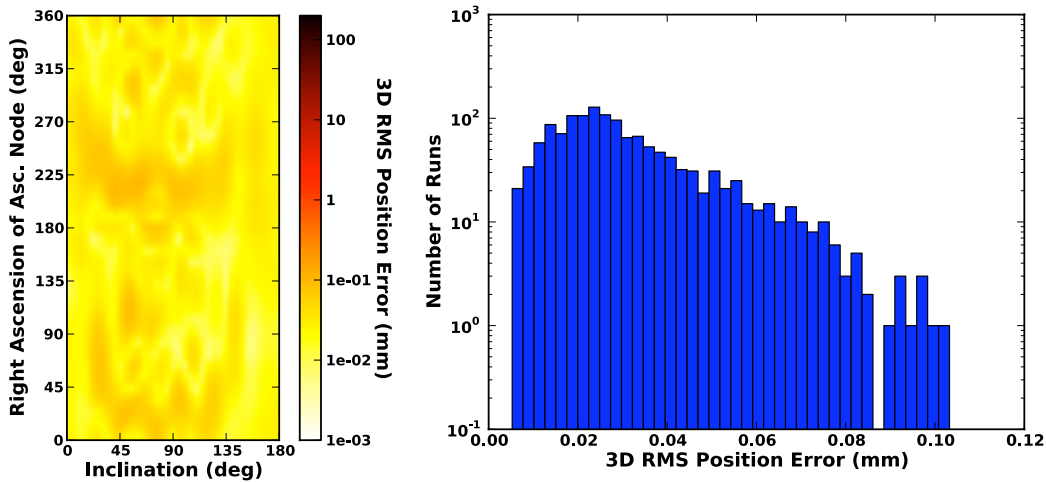
Figure 7.10: Distribution of 3D RMS differences for propagated orbits initially at 20 km with the nominal Eros MRQSphere model.

For Figure 7.9, we propagated two equatorial orbits, one each initially at Ω values of $0°$ and $90°$. The figure illustrates the propagation error and the simulated orbit altitude and eccentricity. Due to the relatively fast rotation rate of Eros, orbits initially at right ascensions close to $90°$ and $270°$ have extended periods of interactions with the lobes. These interactions exert a larger torque on the orbit, thus changing the orbit elements. In this case, it forces the radius of periapsis to drop below $2 R_E$, and, hence, below the minimum orbit altitude for this MRQSphere model. We note that equatorial orbits within approximately $2 R_E$ in radius correspond to the regions of instability derived in Scheeres (2002).

For the purpose of comparison, we provide details on the orbits initially at an altitude of 20

km in Figure 7.10. These orbits remain within the range covered by the MRQSphere model, and, thus, errors are less than 0.11 mm.

7.2   Model Estimation

In this section, we describe the procedure used to estimate the NEAR15A gravity field using the MRQSphere model. First, we describe the estimated state and the observations used, followed by a description of the estimation algorithm employed. Additionally, we define a redistribution technique that allows us to correctly distribute the estimated gravity field among the shells. Finally, we provide and discuss results of the estimation process.

7.2.1   Estimation Process

To simplify the gravity estimation process for this proof of concept, we only estimate the terms of the gravity field. This differs from missions to bodies beyond Earth orbit that often utilize a statistical filter, usually a square-root information filter (SRIF), to estimate the the satellite position, gravity field, and other parameters using radio science and other observations. Here, we assume the satellite state is known, with measurements of the gravity potential provided with some accuracy. Furthermore, we only estimate the Z_j values for a single shell at a time as we approach the asteroid. Thus, our estimated state vector is

$$\mathbf{X}_j = \begin{bmatrix} \sqrt{w_1} Z_j(\alpha_1) \\ \sqrt{w_2} Z_j(\alpha_2) \\ \vdots \\ \sqrt{w_M} Z_j(\alpha_M) \end{bmatrix} \tag{7.1}$$

where M is the number of nodes for a given shell. The reason for the $\sqrt{w_i}$ factor will be explained below. We then rewrite Equation 2.85, in terms of Z_j, as

$$Z_j(\alpha) = \sum_{i=1}^{M} K_N(\alpha \cdot \alpha_i) \sqrt{w_i} (\sqrt{w_i} Z_j(\alpha_i)). \tag{7.2}$$

Additionally, we constrain the observations to include those of the satellite within the altitude range for a single MRQSphere shell, and only estimate one shell at a time. We first estimate the outermost shell, and then reduce the altitude range to proceed to the next shell (given estimates of all previous shells). Since the MRQSphere model starts with the initial range of shells -5 through -1, we must assume an a priori estimate of these shells is available. Section 7.2.3 discusses how this may be accomplished.
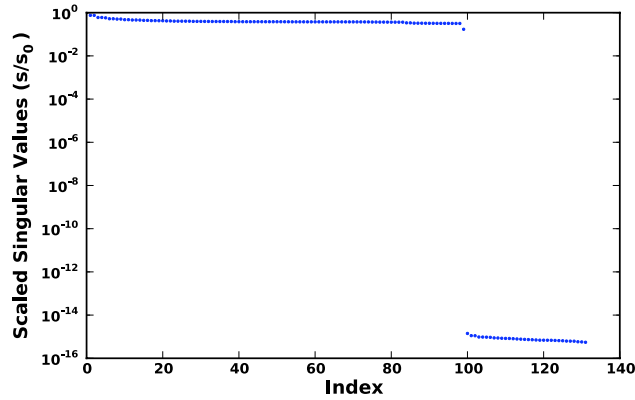
Figure 7.11: Singular values for the H matrix when estimating the j=0 shell with 132 nodes.

Since we only estimate one shell at a time, designated as shell j, contributions of previously estimated shells to the observed potential must be removed. Our observation U_i' is thus

$$U_i' = \frac{R_E}{\mu} \left(U_i - \frac{\mu}{|\mathbf{r}_i|} - \sum_{k=j_{min},\ldots,j-1} \tilde{U}(\mathbf{r}_i; \mathbb{J} = \{k\}) \right) \tag{7.3}$$

where U_i is the original observation and j_{min} is the lowest index in the MRQSphere model. Note that we have also removed the two-body contribution and scaled the observation by μ/R_E to simplify the computations. We add Gaussian noise to the observation with zero mean and a standard deviation of 1×10^{-11}. This noise was selected to provide approximately five, and as little as three, digits of accuracy in the observation, which matches the corresponding parameters selected for the MRQSphere model. The resulting state to observation mapping matrix H for observation U_i' at

position $\mathbf{r}_i$ is

$$H = \left[e^{-\left(\ln \frac{|\mathbf{r}_i|}{R_E}\right)^2 \sigma_j^2/2} K_n(\hat{r}_i \cdot \alpha_1)\sqrt{w_1} \quad \ldots \quad e^{-\left(\ln \frac{|\mathbf{r}_i|}{R_E}\right)^2 \sigma_j^2/2} K_n(\hat{r}_i \cdot \alpha_M)\sqrt{w_M} \right]. \tag{7.4}$$

In Figure 7.11, we provide the singular values of the H matrix defined in Equation 7.4 when estimating the $j=0$ shell. As illustrated, H is not full rank and the normal least-squares algorithm of Section 3.2.1 will not suffice. Thus, we use the SVD algorithm described in Section 3.2.2 for estimating the MRQSphere gravity field, and set scaled singular values less than 10^{-15} to zero.

To model the observations, we simulate a collection of satellite orbits using the full NEAR15A spherical harmonic gravity model, which we consider the true gravity field. Nine sets of observations are generated, one each for the range of orbit radii in Table 7.2. Thus we have one set of observations for each of the shells indexed from 0 through 8. We propagate orbits long enough to provide (roughly) complete coverage of the gravity field, i.e. groundtracks overlay the full surface of the asteroid, and sample the orbit in 5 minute increments. The initial sidereal time of the asteroid was $0°$ with a rotation rate of 3.3116598×10^{-4} rad/s (from Konopliv et al. (2002)).

7.2.2 Estimated Gravity Field Redistribution

Since the shells, as defined by Gaussians, overlap, the estimation process does not control how a contribution of a particular degree n influences the model. Thus, estimated functions Z_j may deviate from their definition in Equation 2.100. To match the estimated function Z_j to that definition, we use projectors onto the subspace of the spherical harmonics. The reproducing kernel in Equation 2.84 is essentially a projector. Let us consider a function f in the subspace $\mathcal{P}_n$ and the kernel K_m, where $m \leq n$. By multiplying both sides of Equation 2.85 by $\sqrt{w_i}$, and changing the index of summation to prevent confusion with elements of $\mathbb{J}_k$, we have

$$\sqrt{w_i} f_m(\alpha_i) = \sum_{l=1}^{M} (\sqrt{w_i} K_m(\alpha_i \cdot \alpha_l)\sqrt{w_l})(\sqrt{w_l} f_n(\alpha_l)), \tag{7.5}$$

where the number of nodes M is sufficient to discretize Equation 2.85 exactly. The matrix $\mathcal{K}_m$, with elements $\sqrt{w_i} K_m(\alpha_i \cdot \alpha_l)\sqrt{w_l}$, is a projector on the subspace $\mathcal{P}_m$ from the subspace $\mathcal{P}_n$. The

eigenvalues of this matrix are either 1 or 0. The inclusion of $\sqrt{w_l}$ in Equation 7.5 is the reason we used these factors in Equation 7.1.

We now describe a method for using these projectors to properly distribute the gravity field among the shells of the MRQSphere model. First, we select a shell with index j and associated quadrature nodes at α_i (usually the last shell estimated), which models the function Z_j of degree N. Next, we evaluate the currently estimated potential $\tilde{U}(\rho_k \alpha_i; \mathbb{J}_k = \{j_{min}, \ldots, j\})$ at the nodes (α_i) of the selected shell j. The radius ρ_k is the lowest valid radius for the set $\mathbb{J}_k$, i.e. the model using only shells j_{min} through j. Applying the projector, we generate the values $\sqrt{w_i}U_m(\alpha_i)$ at each of the quadrature nodes, where $U_m(\alpha_i)$ refers to the potential of degree m. We perform this operation for each degree $m = 2, \ldots, N-1$. Rearranging Equation 2.81 and multiplying by $\sqrt{w_i}$, we have

$$
\begin{aligned}
\sqrt{w_i}V_m(\alpha_i) &= \left((\sqrt{w_i}U_m(\alpha_i)) - \sum_{p=2}^{m-1} \rho^{-(p+1)}(\sqrt{w_i}V_p(\alpha_i)) \right) \rho^{m+1} \\
&= \left((\sqrt{w_i}U_m(\alpha_i)) - (\sqrt{w_i}U_{m-1}(\alpha_i)) \right) \rho^{m+1}.
\end{aligned} \tag{7.6}
$$

Thus, after mapping the full estimated gravity potential to the lower degree subspaces, we now have a representation of $V_m(\alpha_i)$ for $m = 2, \ldots, N-1$. Using

$$
V_m(\beta_k) = \sum_{i=1}^{M} K_m(\beta_k \cdot \alpha_i)\sqrt{w_i}(\sqrt{w_i}V_n(\alpha_i)), \tag{7.7}
$$

we compute the mth degree projections at the nodes β_k of any lower-index shell in the MRQSphere model. Finally, we combine Equations 7.7, 2.99, and 2.100 to recompute values at the nodes for all shells. Through this process, the information on the gravity field is properly distributed among the shells of the MRQSphere model.

In Figure 7.12, we illustrate the effect of this redistribution process. For this example, we use the SVD algorithm to simultaneously estimate shells -2, -1, and 0. The SVD least-squares algorithm appears to estimate shells -2 and -1 correctly, but not shell 0. However, the overall fit to the data is within the measurement noise. After applying this redistribution algorithm, we recover the correct values on the shell 0. Although it is not apparent in the pictures, the accuracy of shells -2 and -1 is also slightly improved.

We note that the current redistribution algorithm does not include a correction of the state-error covariance matrix. Solving this issue has been designated as future work.
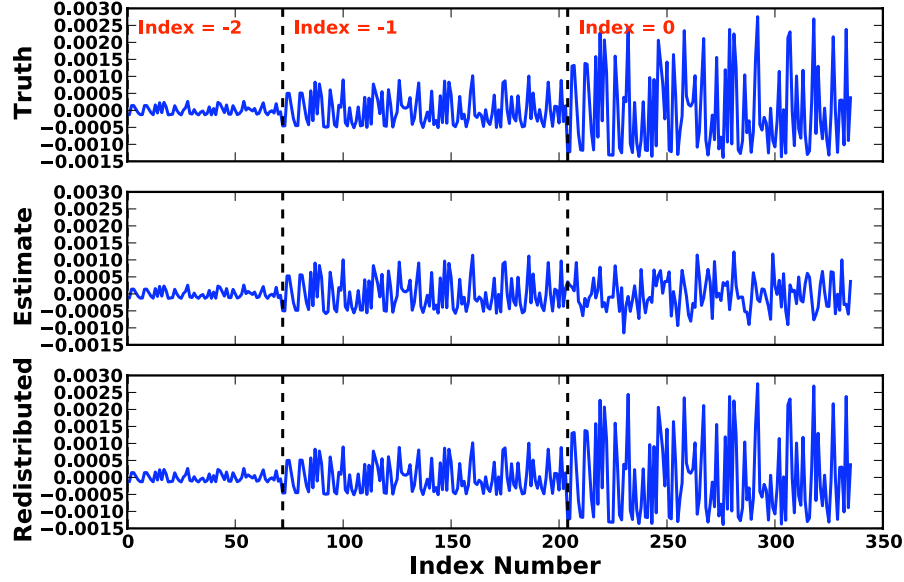
Figure 7.12: Example improvement in gravity field estimation when using the redistribution algorithm with the MRQSphere model.

7.2.3   Estimation Results

As mentioned previously, we assume a low-degree spherical harmonic model is available to initialize shells -5 through -1 in the MRQSphere model. Let us show that a low-accuracy, low-degree spherical harmonic model valid at large distances is sufficient to satisfy this assumption. For this purpose, we conduct three groups of tests. First, we assume no a priori knowledge of the gravity field. Second, we assume that a low-accuracy spherical harmonic model, valid at large distances, is available. Finally, we assume a full, true spherical harmonic gravity model for comparison. We calculate the initial estimates of shells -5 through -1 using this a priori gravity model. We also consider the outcome as a function of which shells participate in estimation.

To generate the low-accuracy spherical harmonic model, we scale the 1-σ standard deviations for each term of the NEAR15A model by 10^4. We selected this value to yield a σ for the $C_{2,0}$ term

of the same order of magnitude as $C_{2,0}$. We then apply Gaussian noise with zero mean and the scaled σ to the true value. For the zonal terms through degree 4, this generates a Stokes coefficient on the same order of magnitude as its true value. For all other terms, the σ value may be orders of magnitude greater than the NEAR15A coefficient. We expect that, in practice, initial estimates of the gravity field will be more accurate than that. Before spacecraft rendezvous, an initial estimate of the gravity field may be generated using radar imaging of the asteroid. In this case, evaluation of surface integrals over the resulting polyhedron shape of the small body yields a low-degree spherical harmonic model (Werner and Scheeres, 1997). Additionally, an initial low-degree spherical harmonic model may be generated using a series of asteroid flybys before capture (Takahashi and Scheeres, 2010).

Table 7.4 presents the statistical accuracy of the resulting acceleration vectors for the different a priori models after estimating all shells. The table also illustrates the effects of increasing the number of shells estimated using the first data set. Shells one through eight are estimated individually for all tests. We note that there is no statistical difference in estimating only shell zero with either a low accuracy a priori gravity model or a true gravity model. However, the effects of providing no initial gravity model has a noticeable impact. For the remainder of this section, we examine results for the estimation of shell 0 with the low-accuracy gravity model.

Table 7.4: MRQSphere determined acceleration precision with the true spherical harmonic model for various combinations of a priori estimates and state vectors. Values presented are mean CD and 1-σ standard deviations.

Shells Estimated (j index)	Zeros	Low Accuracy	True
-5, -4, -3, -2, -1, 0	3.511/.698	3.399/.698	3.340/.769
-2, -1, 0	2.866/.726	2.789/.730	3.288/.760
0	4.073/.668	5.416/.727	5.394/.695

In Figure 7.13, we provide a histogram of the precision of the acceleration vectors with those determined by the spherical harmonic model. Unlike the baseline results presented in Figure 7.3, precision is roughly uniform for all radii. For that baseline model, ϵ determines the absolute limit of the MRQSphere model accuracy. Figure 7.13 demonstrates that, as expected, the estimation

problem further limits accuracy based on the estimation algorithm employed and the measurement accuracy. In this case, measurement accuracy of 4 or 5 digits yields a model accurate to just as many digits. The decrease in precision for low altitude points, i.e. points requiring the evaluation of shell 8, is a result of reduced accuracy for the final shell estimated. If the estimation process had been truncated with shell 5 and only points above 4.6 R_E were tested, results demonstrate this downward trend would still be seen. These results have not been provided in the interest of brevity.
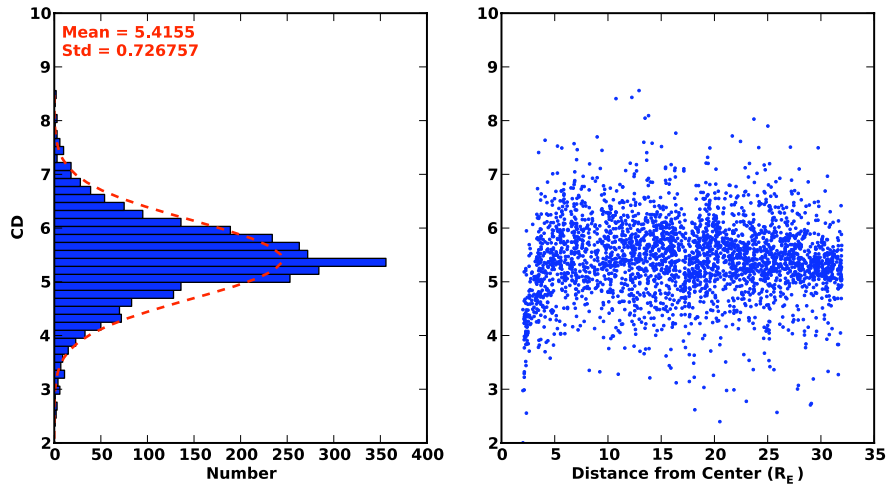
Figure 7.13: Precision of the estimated MRQSphere model with the spherical harmonic model, defined by the number of common digits between them. The figure on the right provides the distribution of accuracy with radius

Figure 7.14 provides the relative accuracy of the Laplacian of the estimated model. Unlike the acceleration vector, there is a small radial dependency on the accuracy of the Laplacian, especially as the radius decreases towards 17.22 R_E. Like the idealized model results of Figure 7.5, the ability of the Laplacian to satisfy the constraints of potential theory depends on the accuracy of the model. In this case, an MRQSphere accurate to 5 digits yields a Laplacian with a relative accuracy of approximately 10^{-5}.

Figure 7.15 illustrates the spatial distribution of errors in the estimated MRQSphere model. Errors do not correspond to regions of high gravity variability, but are more coupled with the dis-
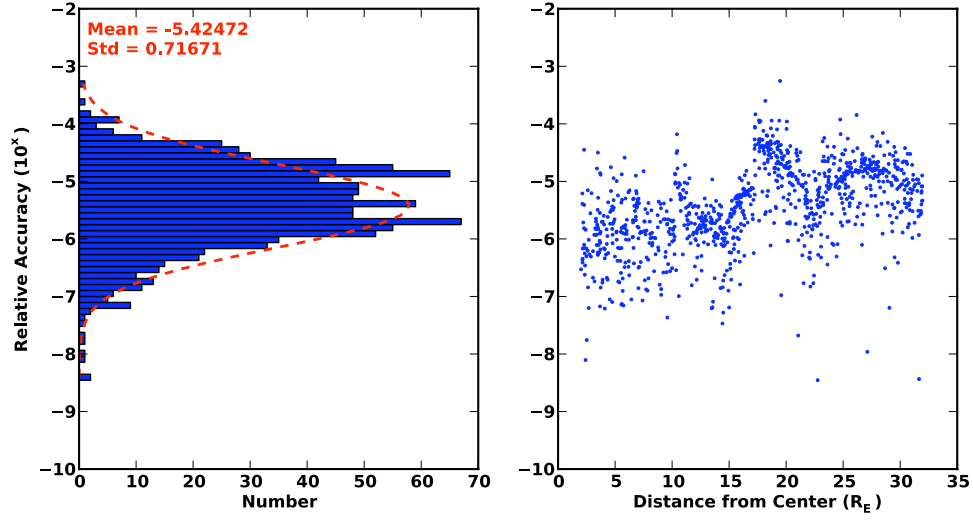
Figure 7.14: Relative accuracy of the Laplacian $(\nabla^2 \tilde{U})$ of the estimated MRQSphere model when compared to the maximum diagonal element of the variational equation matrix. The figure on the right provides the distribution of significant digits with radius.
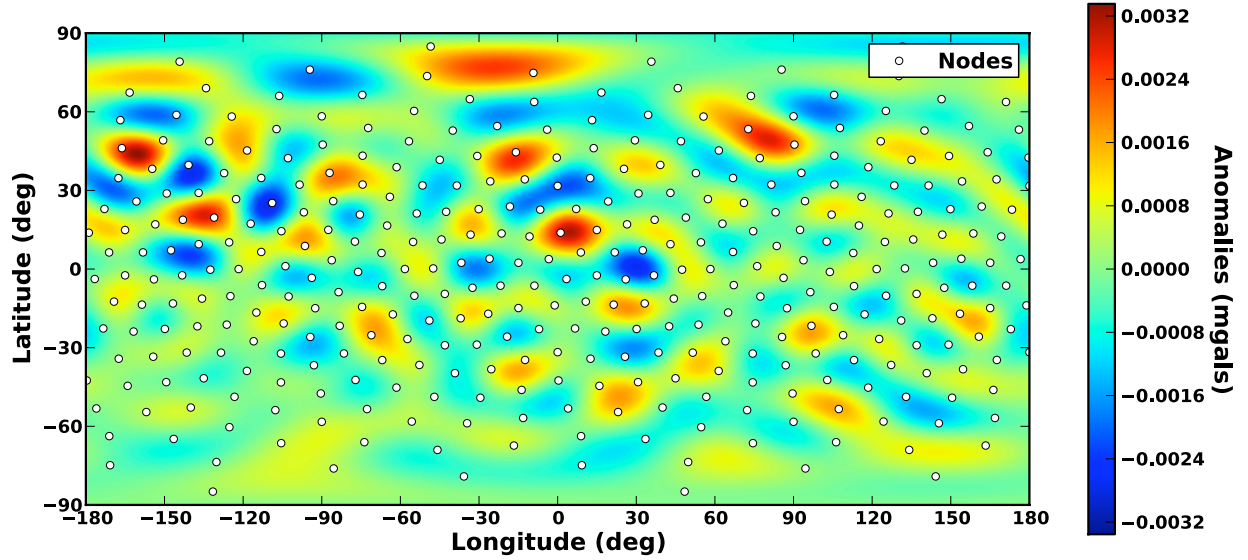
Figure 7.15: Gravity anomalies for the estimated MRQSphere model at $r = 2\ R_E$

tribution of measurements over the surface of the asteroid. In Figure 7.16, we process observations for shell 8 with large regions deprived of measurements. Peak anomalies have doubled in magnitude and correspond to regions with no observations. Regions with observations exhibit results mostly comparable to those in Figure 7.15. Of course, this is an issue with the spherical harmonic gravity model as well. A primary example of this phenomenon is estimation of the lunar gravity field where little is known about the Moon's far side gravity terms (Konopliv et al., 2001).
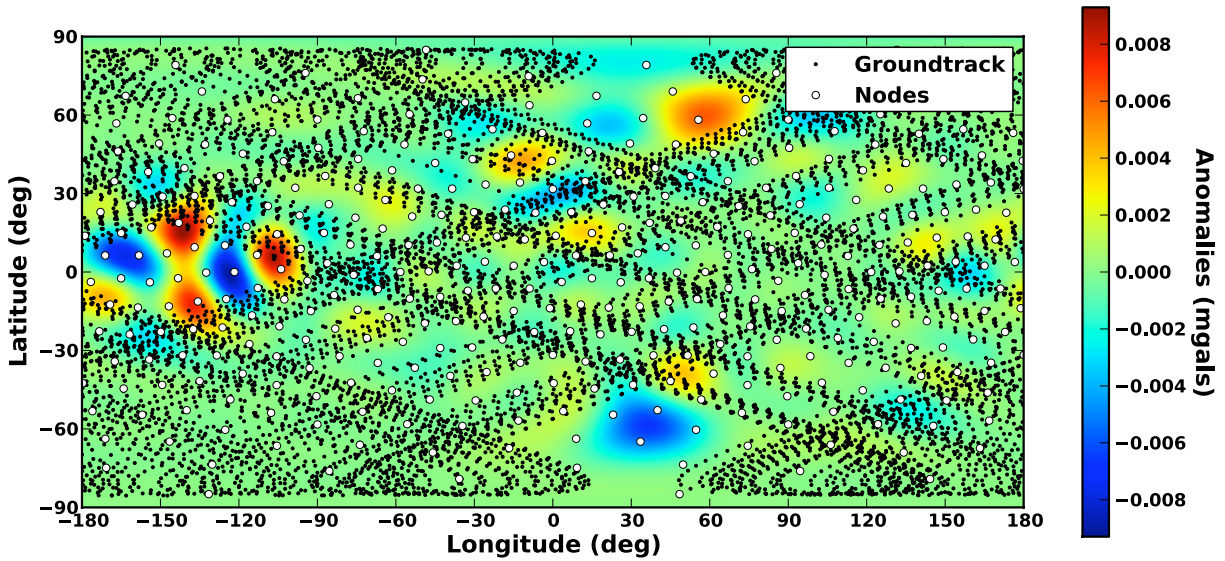
Figure 7.16: Gravity anomalies for the estimated MRQSphere model at $r = 2\ R_E$ with spatial gaps in data.

Figure 7.17 illustrates the 3D RMS orbit propagation error after 24 hours using the same method as that of the orbit propagation test in Section 7.1.1. In this discussion, we ignore orbits at altitudes less than 1 R_E since such orbits correspond to regions of orbit instability, and propagation errors are also a product of orbit altitudes below the applicable range of the MRQSphere model. Orbits initially at a 20 km altitude, corresponding to the range required for shell eight, have a 3D RMS accuracy on the order of 1 m. This error decreases with altitude as the absolute error of the estimated MRQSphere model decreases, i.e. the two-body term dominates and gravity perturbations attenuate. However, a 1 m 3D RMS errors is less than the 5 m orbit determination error for the NEAR mission satellite at comparable altitudes.
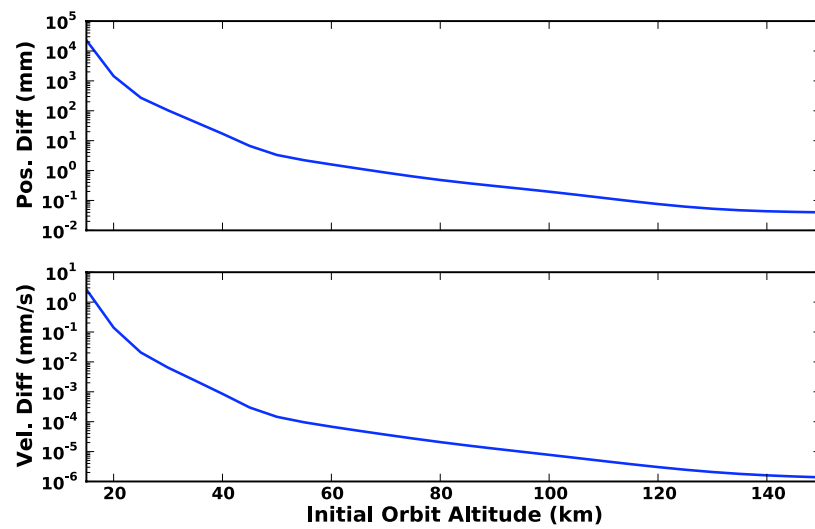
Figure 7.17: Summary of 3D RMS position and velocity errors for orbits propagated with the estimated MRQSphere model versus the spherical harmonic model.

7.3   Chapter Summary

In this chapter, we provided an example configuration of the MRQSphere model representing the gravity field of the asteroid 433 Eros. We used this example to describe performance of the model in the idealized situation. The construction of the MRQSphere model is dependent on several user-defined tuning parameters, most notably the accuracy of the Gaussian approximation of inverse powers of distance ρ. This approximation allows for the multiresolution representation of the gravity field and leads to the definition of the shells to account for its angular variations.

This chapter also demonstrated the estimation capabilities of the MRQSphere gravity representation for a small body using measurements of the gravity potential. We have presented a systematic method for estimating the gravity field using a multiresolution representation. Given an initial gravity model, each shell of the MRQSphere model is estimated separately as the satellite slowly approaches the primary body. As information on the total gravity field improves, a redistribution algorithm applies corrections to previously estimated shells. Using measurements with relatively low accuracy and relatively good spatial distribution, a MRQSphere model was estimated with accuracies comparable to the measurements provided. Like the spherical harmonic model, large regions without measurements yielded a reduced accuracy in the total gravity field.

Chapter 8

Summary and Conclusions

This research considered two new gravity models, the cubed-sphere and MRQSphere models, and their implications for fast orbit propagation and efficient estimation. This chapter summarizes this research, states conclusions, and describes future work.

8.1   Summary of Contributions

We presented and demonstrated the use of the cubed-sphere and MRQSphere models for astrodynamics applications. The cubed-sphere model provides rapid evaluation of the gravity field, with applications to orbit propagation and determination, while the MRQSphere model allows for the estimation of the gravity field. We presented these models, the mathematical tools they employ, and the methods used to configure them based on a given set of requirements. We then tested these models to determine their benefits to astrodynamics applications.

We characterized the impacts of using the cubed-sphere model in satellite orbit propagation. To accomplish this, we performed a series of Monte-Carlo-like studies by comparing propagated trajectories, including their required computation time, with those generated using the spherical harmonic model. Propagation speed improved when using the cubed-sphere model, especially for higher degrees. For highly-precise models, orbit propagation yielded 3D RMS differences on the order of fractions of a millimeter over 24 hours. When we reduced the precision requirements by two digits and relaxed the memory limitations, we generated a cubed-sphere model that was two to three times faster with only a small reduction in precision of the propagated orbits.

We merged the cubed-sphere model with the extended and unscented Kalman filters to demonstrate its use in sequential estimation. In this process, we altered the gravity model to represent the gravity acceleration's Jacobian using an additional six submodels, thus allowing for the generation of a state transition matrix for state-error covariance matrix propagation. We then tested the cubed-sphere model in the EKF and UKF, with speedup factors depending on the density of observations. By observation density, we refer to the number of observations per unit of time. For low-observation-density scenarios, the time update dominates the filter execution time; thus, faster orbit propagation yields faster filter execution. Since the additional computation time required for cubed-sphere models of higher degree is small, orbit determination systems may use high-degree gravity models with little change in computational burden. We also demonstrated that using the cubed-sphere model for orbit determination provides highly precise solutions when compared to those generated using the spherical harmonic model.

We applied the MRQSphere model to the problem of gravity estimation for small bodies. In this simplified study, we modeled and estimated the gravity field for the asteroid 433 Eros. We generated two models: (1) one derived directly from the NEAR15A spherical harmonic model, and (2) a model based on simulated observations of the gravity potential. Based on required accuracy, this MRQSphere model outlined a staged approach to the primary body that allowed for a systematic determination of the gravity field. Using a simplified scenario, we estimated a MRQSphere gravity model that met accuracy requirements when provided measurements with a sufficient spatial distribution. Estimation error increased when we removed this condition, i.e. added gaps in our observation of the gravity field. However, this phenomenon is a problem for other gravity models.

8.2   Conclusions

This research demonstrates that the cubed-sphere model reduces the computational burden for orbit propagation and determination systems. Faster orbit propagation, including the propagation of the state-error covariance matrix, will help existing space surveillance systems to quickly

predict the motion of a catalog of space objects, and may prove to be an important element for future systems that are expected to track over 100,000 objects. Faster orbit determination allows for: (1) reduced computational burden for real-time and near real-time orbit determination, and (2) the inclusion of higher degree gravity models in orbit determination systems limited by computation time. However, improved efficiency of the time update software shifts more of the computational burden towards measurement processing in the filter. Thus, for dense data, we require faster measurement update algorithms and techniques to achieve large improvements in computational efficiency. Additionally, other force models, such as atmospheric density, will now dominate the computation time required for a filter time update.

The MRQSphere model defines a new method for estimating the gravity field, with potential applications to future asteroid missions. Configuration of this model incorporates measurement and model accuracy requirements. Given such a configuration, the MRQSphere model defines a natural, staged manner for approaching a primary body. This simplifies the mission design problem by adding constraints to achieve a given accuracy. Conversely, this aspect provides information on a mission's capability to meet accuracy requirements, i.e. directly correlates knowledge of measurement accuracy and mission design with the highest degree gravity model that may be estimated.

8.3   Future Research

Some research may still be conducted to improve the cubed-sphere model. With recent developments in approximation theory, some of the tools used within the model are no longer optimal. However, given the low cost of memory in modern computers, the model still meets current demands. We instead mention improvements for the current formulation of the cubed-sphere model. The relatively fast attenuation of the higher-degree contributions to the gravity field yield an improved precision with the base model as altitude increases. This means the cubed-sphere model includes too many nodes at these higher altitudes. Improvements may be made to reduce memory requirements by preventing this oversampling of the base model. Additionally, we currently model the gravity potential Jacobian using six additional submodels. This increases the memory

by, at minimum, a factor of two. Other methods, such as direct differentiation of the interpolating functions, may allow for a reduced footprint. Impacts to model computation time and precision with such changes are not yet understood, and, thus, would require additional research. Finally, the configuration methods may be altered to incorporate knowledge of the statistical accuracy of a given base model. This relaxes model precision requirements, thus allowing for faster evaluation and a reduced file size. We have not performed this task since a reduced precision may cause hesitation in the adoption of this model.

Several opportunities exists for further characterizing the use of the cubed-sphere model for orbit determination. In this research, we only considered sequential estimation techniques. With the addition of the Jacobian, we may now use this model in a batch least squares estimation algorithm. This is more congruent with the estimation techniques employed by the Air Force for space object catalog estimation. Additionally, the model should be tested in a third-party orbit determination system such as GIPSY-OASIS or GEODYN. This aids in disseminating the model and provides a more realistic estimation of navigation efficiency improvements.

Our research involving the MRQSphere model simply proves that it may be used for gravity estimation, but more research is required. In the context of small bodies, the two major goals for future work are: (1) integrating the MRQSphere model with a more traditional orbit determination scheme using a square-root information filter (SRIF), and (2) altering the representation for evaluation within the circumscribing sphere. Integration of the model with the SRIF should demonstrate the MRQSphere's applicability to small-body gravity estimation and provide a more realistic characterization of the model's estimation capabilities using radio science observations. A challenge in this task is defining an algorithm to correct the estimated-state covariance matrix using the redistribution algorithm. Research to allow for evaluation of the MRQSphere determined gravity field within the circumscribing sphere is ongoing.

Use of the MRQSphere model is not limited to small bodies. Potential applications include Earth-based gravity estimation, although a more localized representation is desired for such an application. This allows for high-degree solutions, i.e. one on par with current representations,

without increasing the computational burden caused by evaluating the reproducing kernel for each node on the sphere.

We have not considered what improvements the MRQSphere model may have on future mission design or scientific studies. Semi-analytic theory currently exists for orbit perturbations using the spherical harmonic model, which is especially important for characterizing the dynamical environment near such irregularly shaped objects. Additionally, geodesists use the spherical harmonic model to measure mass flux and, in combination with other data, to constrain estimates of mass distribution in a given body. Such applications of the MRQSphere have not yet been considered, but are somewhat premature at this stage.

Bibliography

Ahn, K. S., *Application of Singular Value Decomposition to Gravity Field Model Development Using Satellite Data*, Ph.D. thesis, The University of Texas at Austin, 1996.

Ahrens, C. and Beylkin, G., "Rotationally Invariant Quadratures for the Sphere," *Proceedings of the Royal Society A*, Vol. 465, No. 2110, pp. 3103–3125, October 2009.

ARINC Engineering Services, *Navstar GPS Space Segment/Navigation User Interfaces (IS-GPS-200D)*, Navstar GPS Joint Program Office, December 7 2004.

Ashenberg, J., "Proposed Method for Modeling the Gravitational Interaction Between Finite Bodies," *Journal of Guidance, Control, and Dynamics*, Vol. 28, No. 4, pp. 768–774, July-August 2005.

Augustine, N. R., Austin, W. M., Chyba, C., Kennel, C. F., Bejmuk, B. I., Crawley, E. F., Lyles, L. L., Chiao, L., Greason, J., and Ride, S. K., "Seeking a Human Spaceflight Program Worthy Of A Great Nation," Tech. rep., U.S. Human Spaceflight Plans Committee, 2009.

Bate, R. R., Mueller, D. D., and White, J. E., *Fundamentals of Astrodynamics*, Dover Publications, Inc., New York, 1971.

Bertiger, W., Desai, S., Dorsey, A., Haines, B. J., Harvey, N., Kuang, D., Sibthorpe, A., and Weiss, J. P., "Sub-Centimeter Precision Orbit Determination with GPS for Ocean Altimetry," *Marine Geodesy*, Vol. 33, No. S1, pp. 363–378, 2010.

Bettadpur, S. V., Schutz, B. E., and Lundberg, J. B., "Spherical harmonic synthesis and least squares computations in satellite gravity gradiometry," *Journal of Geodesy*, Vol. 66, No. 3, pp. 261–271, October 1992.

Beylkin, G. and Cramer, R., "Toward Multiresolution Estimation and Efficient Representation of Gravitational Fields," *Celestial Mechanics and Dynamical Astronomy*, Vol. 84, pp. 87–104, 2002.

Beylkin, G. and Monzón, L., "Approximation by Exponential Sums Revisited," *Applied Computational Harmonic Analysis*, Vol. 28, No. 2, pp. 131–149, March 2010.

Boikov, V., Khutorovsky, Z. N., and Alfriend, K. T., "Singular Value Decomposition and Least Squares Orbit Determination," in *AAS/AIAA Astrodynamics Conference*, Mackinac Island, Michigan, August 19-23 2007.

Bond, V. R. and Allman, M. C., *Modern Astrodynamics*, Princeton University Press, Princeton, New Jersey, 1996.

Bowman, B. R., Tobiska, W. K., Marcos, F. A., Huang, C. Y., Lin, C. S., and Burke, W. J., "A New Empirical Thermospheric Density Model JB2008 Using New Solar and Geomagnetic Indices Using New Solar and Geomagnetic Indices," in *AIAA/AAS Astrodynamics Specialist Conference*, Honolulu, Hawaii, August 18-21 2008.

Casotto, S. and Fantino, E., "Evaluation of methods for spherical harmonic synthesis of the gravitational potential and its gradients," *Advances in Space Research*, Vol. 40, pp. 69–75, 2007.

Cheng, A. F., Santo, A. G., Heeres, K. J., Landshof, J. A., Farquhar, R. W., Gold, R. E., and Leet, S. C., "Near-Earth Asteroid Rendezvous: Mission Overview," *Journal of Geophysical Research*, Vol. 102, No. E10, pp. 23,695–23,708, October 1997.

Chui, C. K., *An Introduction to Wavelets*, *Wavelet Analysis and Its Applications*, Vol. One, first ed., Academic Press, Inc., Boston, 1992.

Clenshaw, C. W., "A Note on the Summation of Chebyshev Series," *Mathematical Tables and Other Aids to Computation*, Vol. 9, pp. 118–120, 1955.

Colombi, A., Hirani, A. N., and Villac, B. F., "Adaptive Gravitational Force Representation for Fast Trajectory Propagation Near Small Bodies," *Journal of Guidance, Control, and Dynamics*, Vol. 31, No. 4, pp. 1041–1051, July-August 2008.

Colombi, A., Hirani, A. N., and Villac, B. F., "Structure Preserving Approximations of Conservative Forces for Application to Small Body Dynamics," *Journal of Guidance, Control, and Dynamics*, Vol. 32, No. 6, pp. 1847–1858, November - December 2009.

Colombo, O., "Numerical Methods for Harmonic Analysis on the Sphere," Tech. Rep. 310, Department of Geodetic Science and Surveying, 1981.

Crassidis, J. L. and Junkins, J. L., *Optimal Estimation of Dynamic Systems*, Applied Mathematics and Nonlinear Science, Chapman and Hall/CRC, 2004.

Cunningham, L. E., "On the Computation of the Spherical Harmonic Terms Needed During the Numerical Integration of the Orbital Motion of an Artificial Satellite," *Celestial Mechanics*, Vol. 2, No. 2, pp. 207–216, 1970.

deBoor, C., *A Practical Guide to Splines*, *Applied Mathematical Sciences*, Vol. 27, first hardback ed., Springer, New York, 2001.

Deprit, A., "Note on the Summation of Legendre Series," *Celestial Mechanics*, Vol. 20, No. 4, pp. 319–323, 1979.

Desai, S. D., Bertiger, W., Dorsey, A., Haines, B. J., Lane, C., and Weiss, J. P., "GPS-Based Precise Orbit Determination in Near Real Time for Operational Altimetry," in *AAS Guidance, Navigation, and Control Conference*, Breckenridge, Colorado, February 6-10 2010.

Dilts, G. A., "Computation of Spherical Harmonic Expansion Coefficients Via FFT's," *Journal of Computational Physics*, Vol. 57, No. 3, pp. 439–453, February 1985.

Dow, J. M., Neilan, R. E., and Rizos, C., "The International GNSS Service In a Changing Landscape of Global Navigation Satellite Systems," *Journal of Geodesy*, Vol. 83, pp. 191–198, 2009.

Einstein, A., "Die Grundlage der allgemeinen Relativitätstheorie," *Annalen der Physik*, Vol. 49, 1916.

Engels, R. C. and Junkins, J. L., "Local Representation of the Geopotential by Weighted Orthonormal Polynomials," *Journal of Guidance and Control*, Vol. 3, No. 1, pp. 55–61, Jan.-Feb. 1980.

Fantino, E. and Casotto, S., "Methods of Harmonic Synthesis for Global Geopotential Models and Their First-, Second-, and Third-order Gradients," *Journal of Geodesy*, Vol. 83, No. 7, pp. 595–619, November 2009.

Fašková, Z., Čunderlík, R., and Mikula, K., "Finite Element Methods for Solving Geodetic Boundary Value Problems," *Journal of Geodesy*, Vol. 84, pp. 135–144, 2010.

Fehlberg, E., "Classical Fifth-, Sixth-, Seventh-, and Eight-Order Runge-Kutta Formulas with Stepsize Control," Technical Report NASA-TR-R-287, NASA Marshall Space Flight Center, Huntsville, Alabama, October 1968.

Fujiwara, A., Mukai, T., Kawaguchi, J., and Uesugi, K. T., "Sample return mission to NEA: MUSES-C," *Advances in Space Research*, Vol. 25, No. 2, pp. 231–238, 2000.

Galilei, G., *Discorsi e dimostrazioni matematiche, intorno à due nuove scienze*, Louis Elsevier, Leiden, 1638.

Garmier, R. and Barriot, J.-P., "Ellipsoidal Harmonic expansions of the gravitational potential: Theory and Application," *Celestial Mechanics and Dynamical Astronomy*, Vol. 79, No. 4, pp. 235–275, April 2001.

Garmier, R., Barriot, J.-P., Konopliv, A. S., and Yeomans, D. K., "Modeling of the Eros gravity field as an ellipsoidal harmonic expansion from the NEAR Doppler tracking data," *Geophysical Research Letters*, Vol. 29, No. 8, pp. 721–723, 2002.

Geissler, P., Petit, J.-M., Durda, D. D., Greenberg, R., Bottke, W., and Nolan, M., "Erosion and Ejecta Reaccretion on 243 Ida and Its Moon," *Icarus*, Vol. 120, pp. 140–157, 1996.

Glassmeier, K.-H., Boehnhardt, H., Koschny, D., Kührt, E., and Richter, I., "The Rosetta Mission: Flying Towards the Origin of the Solar System," *Space Science Reviews*, Vol. 128, No. 1-4, pp. 1–21, February 2007.

Gottlieb, P., "Estimation of Local Lunar Gravity Features," *Radio Science*, Vol. 5, No. 2, pp. 301–312, 1970.

Gottlieb, R. G., "Fast Gravity, Gravity Partials, Normalized Gravity, Gravity Gradient Torque and Magnetic Field: Derivation, Code and Data," Tech. Rep. NASA Contractor Report 188243, NASA Lyndon B. Johnson Space Center, Houston, TX, February 1993.

Gradshteyn, I. S. and Ryzhik, I. M., *Table of Integrals, Series and Products*, 7th ed., Elsevier Academic Press, 2007.

Heiskanen, W. A., "Investigations on the gravity formula," *Publications of the Isostatic Institute of the International Association of Geodesy*, Vol. 1, 1938.

Heiskanen, W. A. and Moritz, H., *Physical Geodesy*, W. H. Freeman and Company, San Francisco, 1967.

Hill, K. and Jones, B. A., *TurboProp Version 4.0*, Colorado Center for Astrodynamics Research, May 2009.

Hinga, M. B., *Using Parallel Computation to Apply the Singular Value Decomposition (SVD) in Solving for Large Earth Gravity Fields Based on Satellite Data*, Ph.D. thesis, The University of Texas at Austin, 2004.

Hobson, E. W., *The Theory of Spherical and Ellipsoidal Harmonics*, first ed., Chelsea Publishing Company, New York, 1931.

Hofmann-Wellenhof, B. and Moritz, H., *Physical Geodesy*, second ed., SpringerWienNewYork, 2006.

Hujsak, R. S., "Gravity Acceleration Approximation Functions," *Advances in the Astronautical Sciences*, Vol. 93, No. Pt. 1, pp. 335–349, 1996.

Hwang, C., Tseng, T.-P., Lin, T., Švehla, D., and Schreiner, B., "Precise Orbit Determination for the FORMOSAT-3/COSMIC Satellite Missions Using GPS," *Journal of Geodesy*, Vol. 83, No. 5, pp. 477–489, 2008.

James, L. D., "Keeping the Space Environment Safe for Civil and Commercial Users," Testimony to the Subcommittee on Space and Aeronautics, House Committee on Science and Technology, 28 April 2009.

Jekeli, C., Lee, J. K., and Kwon, J. H., "On the Computation and Approximation of Ultra-High Degree Spherical Harmonics," *Journal of Geodesy*, Vol. 81, pp. 603–615, 2007.

Jones, B. A., Beylkin, G., Born, G. H., and Provence, R. S., "A New Representation for Small-Body Gravity Estimation," in *AIAA/AAS Astrodynamics Specialist Conference*, Toronto, ON, Canada, August 2-5 2010a.

Jones, B. A., Born, G. H., and Beylkin, G., "Comparisons of the Cubed-Sphere Gravity Model with the Spherical Harmonics," *Journal of Guidance, Control, and Dynamics*, Vol. 33, No. 2, pp. 415–425, March-April 2010b.

Jones, B. A., Born, G. H., and Beylkin, G., "Orbit Determination with the Cubed-Sphere Gravity Model," in *20th Annual AAS/AIAA Spaceflight Mechanics Meeting*, San Diego, California, February 15-17 2010c.

Julier, S. J., "The Scaled Unscented Transformation," in *Proceedings of the IEEE American Control Conference*, pp. 4555–4559, IEEE, Anchorage, Alaska, May 8-10, 2002 2002.

Julier, S. J. and Uhlmann, J. K., "A New Extension of the Kalman Filter to Nonlinear Systems," *Proceedings of SPIE*, Vol. 3068, pp. 182–193, 1997.

Junkins, J. L., "Investigation of Finite-Element Representations of the Geopotential," *AIAA Journal*, Vol. 14, No. 6, pp. 803–808, June 1976.

Junkins, J. L., "Development of Finite Element Models for the Earth's Gravity Field. Phase I: Macro Gravity Model for Satellite Orbit Integration," Contract Report ESS77/103, University of Virginia, Research Laboratory for the Engineering Sciences, Charlottesville, Va., March 1977.

Junkins, J. L. and Saunders, J. T., "Development of Finite Element Models for the Earth's Gravity Field. Phase II: Fine Structure Disturbance Gravity Representations," Contract Report ESS77/104, University of Virginia, Research Laboratory for the Engineering Sciences, Charlottesville, Va., March 1977.

Kang, Z., Tapley, B., Bettadpur, S. V., Ries, J. C., Nagel, P., and Pastor, R., "Precise Orbit Determination for the GRACE Mission Using Only GPS Data," *Journal of Geodesy*, Vol. 80, pp. 322–331, 2006.

Kaula, W. M., *Theory of Satellite Geodesy*, Dover Publications, Inc., Mineola, New York, 1966.

Konopliv, A. S., Asmar, S. W., Carranza, E., Sjogren, W., and Yuan, D., "Recent Gravity Models as a Result of the Lunar Prospector Mission," *Icarus*, Vol. 150, No. 1, pp. 1–18, 2001.

Konopliv, A. S., Miller, J. K., Owen, W. M., Yeomans, D. K., and Giorgini, J. D., "A Global Solution for the Gravity Field, Rotation, Landmarks, and Ephemeris of Eros," *Icarus*, Vol. 160, pp. 289–299, 2002.

Lambin, J., Morrow, R., Fu, L.-L., Willis, J. K., Bonekamp, H., Lillibridge, J., Perbos, J., Zaouche, G., Vaze, P., Bannoura, W., Parisot, F., Thouvenot, E., Coutin-Faye, S., Lindstrom, E., and Mignogno, M., "The OSTM/Jason-2 Mission," *Marine Geodesy*, Vol. 33, No. S1, pp. 4–25, 2010.

Laplace, P.-S., *Traité de Mécanique Céleste*, Vol. 1, (translated into English: N. Bowditch, Chelsea Publishing Company, Inc., 1829, Revised 1966), 1798.

Lawson, C. L. and Hanson, R. J., *Solving Least Squares Problems*, first ed., Series in Automatic Computation, Prentice-Hall, Inc., Englewood Cliffs, New Jersey, 1974.

Lemoine, F. G., Cerri, L., Zelensky, N. P., Ries, J. C., and Bertiger, W. I., "Modern Radar Altimetry Challenges to Precise Orbit Determination," in *33rd Annual AAS Guidance and Control Conference*, Breckenridge, Colorado, February 6-10 2010.

Lemoine, F. G., Kenyon, S. C., Factor, J. K., Trimmer, R. G., Pavlis, N. K., Chinn, D. S., Cox, C. M., Klosko, S. M., Luthcke, S. B., Torrence, M. H., Yand, Y. M., Williamson, R. G., Pavlis, E. C., Rapp, R. H., and Olson, T. R., "The Development of the Joint NASA GSFC and NIMA Geopotential Model EGM96," Tech. Rep. NASA/TP-1998-206861, NASA Goddard Space Flight Center, Greenbelt, Maryland, 20771, USA, July 1998.
URL http://cddis.nasa.gov/926/egm96/egm96.html

Lundberg, J. B. and Schutz, B. E., "Recursion Formulas of Legendre Functions for Use with Nonsingular Geopotential Models," *Journal of Guidance*, Vol. 11, No. 1, pp. 31–38, Jan.-Feb. 1988.

Marov, M. Y., Avduevsky, V. S., Akim, E. L., Eneev, T. M., Kremnev, R. S., Kulikov, S. D., Pichkhadze, K. M., Popov, G. A., and Rogovsky, G. N., "Phobos-Grunt: Russian sample return mission," *Advances in Space Research*, Vol. 33, No. 12, pp. 2276–2280, 2004.

Marshall, P. M., *Least Squares Solutions in Statistical Orbit Determination Using Singular Value Decomposition*, Master's thesis, Naval Postgraduate School, Monterey, California, June 1999.

Massatt, P. and Zeitzew, M., "The GPS Constellation Design - Current and Projected," in *Proceedings of the National Technical Meeting*, pp. 435–445, Institute of Navigation, January 21-23 1998.

Meissl, P., "The Use of Finite Elements in Physical Geodesy," Tech. Rep. 313, Department of Geodetic Science and Surveying, 1981.

Melvin, P. J., "Comments on the Summations of Spherical Harmonics in the Geopotential Evaluation Theories of Deprit and Others," *Celestial Mechanics and Dynamical Astronomy*, Vol. 35, No. 4, pp. 345–355, April 1985.

Mohr, P. J., Taylor, B. N., and Newell, D. B., "CODATA Recommended Values of the Fundamental Physical Constants: 2006," Tech. rep., National Institute of Standards and Technology, Gaithersburg, Maryland, 20899, USA, December 2007.

Montenbruck, O. and Gill, E., *Satellite Orbits: Models, Methods, Applications*, Springer, Berlin Heidelberg New York, 2005.

Muller, P. M. and Sjogren, W. L., "Mascons: Lunar Mass Concentrations," *Science*, Vol. 161, No. 3842, pp. 680–684, August 1968.

Nerem, R. S., Jekeli, C., and Kaula, W. M., "Gravity Field Determination and Characteristics: Retrospective and Prospective," *Journal of Geophysical Research*, Vol. 100, No. B8, pp. 15,053–15,074, August 1995.

Newton, I., *Philosophæ Naturalis Principia Mathematica*, (translated into English: A. Motte, 1729; revised by F. Cajori, University of California Press, 1962), 1687.

O'Keefe, J. A., Eckels, A., and Squires, R. K., "Vanguard Measurements Give Pear-Shaped Component of Earth's Figure," *Science*, Vol. 129, No. 3348, pp. 565–566, February 1959.

Park, R. S., Werner, R. A., and Bhaskaran, S., "Estimating Small-Body Gravity Field from Shape Model and Navigation Data," *Journal of Guidance, Control, and Dynamics*, Vol. 33, No. 1, pp. 212–221, January-February 2010.

Pavlis, N. K., Holmes, S. A., Kenyon, S. C., and Factor, J. K., "An Earth Gravitational Model to Degree 2160: EGM2008," in *Proceedings of the European Geosciences Union General Assembly*, Vienna, Austria, April 13-18 2008.

Pearlman, M. R., Degnan, J. J., and Bosworth, J. M., "The International Laser Ranging Service," *Advances in Space Research*, Vol. 30, No. 2, pp. 135–143, July 2002.

Picone, J. M., Hedin, A. E., and Drob, D. P., "NRLMSISE-00 Empirical Model of the Atmosphere: Statistical Comparisons and Scientific Issues," *Journal of Geophysical Research*, Vol. 107, No. A12, pp. 1–16, 2002.

Pines, S., "Uniform Representation of the Gravitational Potential and its Derivatives," *AIAA Journal*, Vol. 11, pp. 1508–1511, Nov. 1973.

Rapp, R. H., "A Fortran Program for the Computation of Gravimetric Quantities from High Degree Spherical Harmonic Expressions," Tech. Rep. 334, Department of Geodetic Science and Surveying, 1982.

Rocken, C., Kuo, Y.-H., Schreiner, W. S., Hunt, D., Sokolovskiy, S., and McCormick, C., "COSMIC System Description," *Terrestrial, Atmospheric and Oceanic Science*, Vol. 11, No. 1, pp. 21–52, March 2000.

Russell, C. T., Coradini, A., Christensen, U., Sanctis, M. C. D., Feldman, W. C., Jaumann, R., Keller, H. U., Konopliv, A. S., McCord, T. B., McFadden, L. A., McSween, H. Y., Mottola, S., Neukum, G., Pieters, C. M., Prettyman, T. H., Raymond, C. A., Smith, D. E., Sykes, M. V., Williams, B. G., Wise, J., and Zuber, M. T., "Dawn: A journey in space and time," *Planetary and Space Science*, Vol. 52, No. 5-6, pp. 465–489, 2004.

Scheeres, D. J., "The Orbital Dynamics Environment of 433 Eros," in *23rd International Symposium on Space Technology and Science*, Matsue, Japan, May 2002.

Scheeres, D. J., Khushalani, B., and Werner, R. A., "Estimating asteroid density distributions from shape and gravity information," *Planetary and Space Science*, Vol. 48, No. 10, pp. 965–971, August 2000.

Scheeres, D. J., Ostro, S., Hudson, R., DeJong, E., and Suzuki, S., "Dynamics of Orbits Close to Asteroid 4179 Toutatis," *Icarus*, Vol. 132, pp. 53–79, 1998.

Scheeres, D. J., Ostro, S., Hudson, R., and Werner, R. A., "Orbits Close to Asteroid 4769 Castalia," *Icarus*, Vol. 121, pp. 67–87, 1996.

Seeber, G., *Satellite Geodesy*, second ed., Walter de Gruyter, Berlin New York, 2003.

Sørensen, L. S. and Forsberg, R., "Greenland Ice Sheet Mass Loss from GRACE Monthly Models," in *Gravity, Geiod and Earth Observation*, *International Association of Geodesy Symposia*, Vol. 135, edited by S. P. Mertikas, pp. 527–532, International Association of Geodesy, Springer, Berlin, 2010.

Spencer, J. L., "Pines' Nonsingular Gravitational Potential Derivation, Description and Implementation," Tech. Rep. NASA Contractor Report 147478, NASA Lyndon B. Johnson Space Center, Houston, TX, February 1976.

Svensson, S. L., "Finite Elements on the Sphere," *Journal of Approximation Theory*, Vol. 40, pp. 246–260, 1984.

Szegö, G., *Orthogonal Polynomials*, 4th ed., American Mathematical Society, Providence, RI, 1975.

Takahashi, Y. and Scheeres, D. J., "Rapid Characterization of a Small Body Via Slow Flybys," in *20th Annual AAS/AIAA Spaceflight Mechanics Meeting*, San Diego, California, February 15-17 2010.

Tapley, B., Ries, J., Bettadpur, S., Chambers, D., Cheng, M., Condi, F., Gunter, B., Kang, Z., Nagel, P., Pastor, R., Pekker, T., Poole, S., and Wang, F., "GGM02 - An Improved Earth Gravity Field Model from GRACE," *Journal of Geodesy*, Vol. 79, pp. 467–478, 2005.

Tapley, B. D., Bettadpur, S., Watkins, M., and Reigber, C., "The Gravity Recovery and Climate Experiment: Mission Overview and Early Results," *Geophysical Research Letters*, Vol. 31, No. 9, p. L09,607, May 2004a.

Tapley, B. D., Schutz, B. E., and Born, G. H., *Statistical Orbit Determination*, first ed., Elsevier Academic Press, Burlington, MA, 2004b.

Tapley, B. D., Watkins, M. M., Ries, J. C., Davis, G. W., Eanes, R. J., Poole, S. R., Rim, H. J., Schutz, B. E., Shum, C., Nerem, R. S., Lerch, F. J., Marshall, J. A., Klosko, S. M., Pavlis, N. K., and Williamson, R. W., "The Joint Gravity Model 3," *Journal of Geophysical Research*, Vol. 101(B12), pp. 28,029–28,050, 1996.

Tavernier, G., Fagard, H., Feissel-Vernier, M., LeBail, K., Lemoine, F. G., Noll, C., Noomen, R., Ries, J. C., Soudarin, L., Valette, J.-J., and Willis, P., "The International DORIS Service: Genesis and Early Achievements," *Journal of Geodesy*, Vol. 80, No. 8-11, pp. 403–417, November 2006.

Thompson, B. F., Hammen, D. G., Jackson, A. A., and Crues, E. Z., "Validation of Gravity Acceleration and Torque Algorithms for Astrodynamics," in *18th Annual AAS/AIAA Spaceflight Mechanics Meeting*, Galveston, Texas, January 28 - 31 2008.

Thomson, W. and Tait, P. G., *Treatise on Natural Philosophy*, Cambridge University Press, 1879.

Tirpak, J. A., "Securing the Space Arena," *Air Force Magazine*, Vol. 87, No. 7, pp. 30–34, July 2004.

Tscherning, C. C., "Computation of the Second-Order Derivatives of the Normal Potential Based on the Representation by a Legendre Series," *Manuscripta Geodectica*, Vol. 1, pp. 71–92, 1976.

Tscherning, C. C., "Functional Methods for Gravity Field Approximation," in *Mathematical and Numerical Techniques in Physical Geodesy*, *Lecture Notes in Earth Sciences*, Vol. 7, edited by H. Sünkel, pp. 1–47, Springer Berlin / Heidelberg, 1986.

Tscherning, C. C., Rapp, R. H., and Goad, C., "A Comparison of Methods for Computing Gravimetric Quantities from High Degree Spherical Harmonic Expansions," *Manuscripta Geodectica*, Vol. 8, pp. 249–272, 1983.

Vallado, D. A. and McClain, W. D., *Fundamentals of Astrodynamics and Applications*, third ed., Microcosm Press and Springer, Hawthorne, CA and New York, NY, 2007.

Van der Merwe, R. and Wan, E. A., "The Square-Root unscented Kalman Filter for State and Parameter-Estimation," in *2001 IEEE International Conference on Acoustics, Speech, and Signal Processing*, Vol. 6, pp. 3461–3464, Salt Lake City, Utah, May 7-11 2001.

Weiss, J. P., Bertiger, W., Desai, S., Haines, B. J., Harvey, N., and Lane, C., "Near Real Time GPS Orbit Determination: Strategies, Performance, and Applications to OSTM/Jason-2," in *AAS Guidance, Navigation, and Control Conference*, Breckenridge, Colorado, February 6-10 2010.

Werner, R. A. and Scheeres, D. J., "Exterior Gravitation of a Polyhedron Derived and Compared with Harmonic and Mascon Gravitational Representations of Asteroid 4769 Castalia," *Celestial Mechanics and Dynamical Astronomy*, Vol. 65, pp. 313–344, 1997.

Wong, L., Buechler, G., Downs, W., Sjogren, W. L., Muller, P., and Gottlieb, P., "A Surface-Layer Representation of the Lunar Gravitational Field," *Journal of Geophysical Research*, Vol. 76, No. 26, pp. 6220–6236, 1971.

Zuber, M. T., Smith, D. E., Cheng, A. F., Garvin, J. B., Aharonson, O., Cole, T. D., Dunn, P. J., Guo, T., Lemoine, F. G., Neumann, G. A., Rowlands, D. D., and Torrence, M. H., "The Shape of 433 Eros from the NEAR-Shoemaker Laser Rangefinder," *Science*, Vol. 289, pp. 2091–2101, September 2000.

Point-Mass Model Approximating a Set of Low-Degree Stokes Coefficients

In Chapter 4, we require a point-mass model that, when converted to Stokes coefficients, approximates the GGM02C gravity model (Tapley et al., 2005) to the largest achievable degree. We treat this point-mass model as a true gravity field for comparing the different formulations of the spherical harmonic model. This appendix describes a least-squares approach to generate such a point-mass gravity model.

A.1   Models for Least Squares Fitting of the Stokes Coefficients

In this section, we outline the tools required to generate a point-mass representation of the GGM02C spherical harmonic model. We perform a normal least-squares fit (see Section 3.2.1) of the Stokes coefficients to solve for the positions of these point masses. We may also solve for their masses, but this increases the condition number of the state-observation mapping matrix $\tilde{H}$. Thus, attempts to simultaneously solve for the mass were not as effective. We define the location of a single point mass

$$\mathbf{r}_i = \begin{bmatrix} x_i & y_i & z_i \end{bmatrix}^T , \tag{A.1}$$

and wish to estimate the location of all N point masses. We write the full estimated state vector

$$\mathbf{X} = \begin{bmatrix} \mathbf{r}_1 \\ \mathbf{r}_2 \\ \vdots \\ \mathbf{r}_N \end{bmatrix} \tag{A.2}$$

where N is the number of point masses estimated.

In this least-squares approach, we fit to the spherical harmonics coefficients of the GGM02C model up to a degree n_{max}, thus

$$\mathbf{Y} = \{\bar{C}_{nm}, \bar{S}_{nm} \in \text{GGM02C} : n \geq 2, n \leq n_{max}, m \leq n\}. \tag{A.3}$$

As presented in Chapter 2, we may derive a set of Stokes coefficients $\bar{C}'_{nm}$ and $\bar{S}'_{nm}$ from a collection of point masses using

$$\bar{C}'_{nm} = \frac{1}{M(2n+1)} \sum_{i=1}^{N} \left(\frac{r_i}{R_p}\right)^n \bar{P}_{nm}[\sin(\phi_i)] \cos(m\lambda_i)\eta_i \tag{A.4}$$

$$\bar{S}'_{nm} = \frac{1}{M(2n+1)} \sum_{i=1}^{N} \left(\frac{r_i}{R_p}\right)^n \bar{P}_{nm}[\sin(\phi_i)] \sin(m\lambda_i)\eta_i \tag{A.5}$$

where (r_i, ϕ_i, λ_i) is the location of the i-th point with mass η_i, R_p is the radius of the primary body, $\bar{P}_{nm}$ is the associated Legendre function of degree n and order m, M is the total mass, and

$$M = \sum_{i=1}^{N} \eta_i. \tag{A.6}$$

Using Equations A.4 and A.5, we define

$$G_{nm}(\mathbf{X}) = \begin{bmatrix} \bar{C}'_{nm}(\mathbf{X}) \\ \bar{S}'_{nm}(\mathbf{X}) \end{bmatrix}, \tag{A.7}$$

and constitute $G(\mathbf{X})$ using $G_{nm}(\mathbf{X})$ for all n and m such that $n \geq 2$, $n \leq n_{max}$, and $m \leq n$. When evaluating Equations A.4 and A.5, we convert from Cartesian to spherical coordinates using

$$r_i = \sqrt{x_i^2 + y_i^2 + z_i^2} \tag{A.8}$$

$$\phi_i = \sin^{-1} \frac{z_i}{r_i} \tag{A.9}$$

$$\lambda_i = \tan^{-1} \frac{y_i}{x_i}. \tag{A.10}$$

The state-to-observation sensitivity matrix for a given i-th point mass is

$$\tilde{H}_{i,nm} = \left[\frac{\partial G_{nm}(\mathbf{r}_i)}{\partial \mathbf{r}_i}\right]^* = \begin{bmatrix} \dfrac{\partial \bar{C}'_{nm}}{\partial x_i} & \dfrac{\partial \bar{C}'_{nm}}{\partial y_i} & \dfrac{\partial \bar{C}'_{nm}}{\partial z_i} \\ \dfrac{\partial \bar{S}'_{nm}}{\partial x_i} & \dfrac{\partial \bar{S}'_{nm}}{\partial y_i} & \dfrac{\partial \bar{S}'_{nm}}{\partial z_i} \end{bmatrix}^* = \begin{bmatrix} \dfrac{\bar{C}'_{nm}}{\partial \mathbf{r}_i} \\ \dfrac{\bar{S}'_{nm}}{\partial \mathbf{r}_i} \end{bmatrix}^* \tag{A.11}$$

for coefficients of degree n and order m. Differentiating Equations A.4 and A.5, we have

$$\frac{\partial \bar{C}'_{nm}}{\partial r_i} = \frac{n\eta_i}{R_p M(2n+1)} \left(\frac{r_i}{R_p}\right)^{n-1} \bar{P}_{nm}[\sin(\phi_i)]\cos(m\lambda_i) \tag{A.12}$$

$$\frac{\partial \bar{C}'_{nm}}{\partial \phi_i} = \frac{\eta_i}{M(2n+1)} \left(\frac{r_i}{R_p}\right)^{n} \frac{\partial \bar{P}_{nm}[\alpha]}{\partial \alpha}\cos(\phi_i)\cos(m\lambda_i) \tag{A.13}$$

$$\frac{\partial \bar{C}'_{nm}}{\partial \lambda_i} = -\frac{m\eta_i}{M(2n+1)} \left(\frac{r_i}{R_p}\right)^{n} \bar{P}_{nm}[\sin(\phi_i)]\sin(m\lambda_i) \tag{A.14}$$

and

$$\frac{\partial \bar{S}'_{nm}}{\partial r_i} = \frac{n\eta_i}{R_p M(2n+1)} \left(\frac{r_i}{R_p}\right)^{n-1} \bar{P}_{nm}[\sin(\phi_i)]\sin(m\lambda_i) \tag{A.15}$$

$$\frac{\partial \bar{S}'_{nm}}{\partial \phi_i} = \frac{\eta_i}{M(2n+1)} \left(\frac{r_i}{R_p}\right)^{n} \frac{\partial \bar{P}_{nm}[\alpha]}{\partial \alpha}\cos(\phi_i)\sin(m\lambda_i) \tag{A.16}$$

$$\frac{\partial \bar{S}'_{nm}}{\partial \lambda_i} = \frac{m\eta_i}{M(2n+1)} \left(\frac{r_i}{R_p}\right)^{n} \bar{P}_{nm}[\sin(\phi_i)]\cos(m\lambda_i). \tag{A.17}$$

Finally, we write

$$\frac{\partial \bar{C}'_{nm}}{\partial \mathbf{r}_i} = \left[\frac{\partial \bar{C}'_{nm}}{\partial r_i}\left(\frac{\partial r_i}{\partial \mathbf{r}_i}\right) + \frac{\partial \bar{C}'_{nm}}{\partial \phi_i}\left(\frac{\partial \phi_i}{\partial \mathbf{r}_i}\right) + \frac{\partial \bar{C}'_{nm}}{\partial \lambda_i}\left(\frac{\partial \lambda_i}{\partial \mathbf{r}_i}\right)\right] \tag{A.18}$$

$$\frac{\partial \bar{S}'_{nm}}{\partial \mathbf{r}_i} = \left[\frac{\partial \bar{S}'_{nm}}{\partial r_i}\left(\frac{\partial r_i}{\partial \mathbf{r}_i}\right) + \frac{\partial \bar{S}'_{nm}}{\partial \phi_i}\left(\frac{\partial \phi_i}{\partial \mathbf{r}_i}\right) + \frac{\partial \bar{S}'_{nm}}{\partial \lambda_i}\left(\frac{\partial \lambda_i}{\partial \mathbf{r}_i}\right)\right]. \tag{A.19}$$

We provided the equations for the partials of the spherical coordinates with respect to the Cartesian coordinates in Equation 2.13. The more complete state-to-observation mapping matrix is then $\tilde{H}'$, which is comprised of

$$\tilde{H}'_{n,m} = \left[\tilde{H}_{1,n,m} \quad \tilde{H}_{2,n,m} \quad \ldots \quad \tilde{H}_{N,n,m}\right] \tag{A.20}$$

for each degree n and order m term included in $\mathbf{Y}$.

In the spherical harmonic model, the degree $n=1$ terms are zero when the center of mass of the primary body is at the origin of the body centered coordinate system. That is the case for the GGM02C model. However, the current formulation of this least squares approximation does not necessarily satisfy this constraint. Thus, we add an additional 'observation' to constrain the center of mass to the origin. We write the distance of the center of mass from the origin

$$r_\circ = |\mathbf{r}_\circ| = \sqrt{x_\circ^2 + y_\circ^2 + z_\circ^2} \tag{A.21}$$

where

$$\mathbf{r}_\circ = \frac{\sum_{j=1}^{k} \eta_i \mathbf{r}_i}{M}. \tag{A.22}$$

Upon augmenting the $\tilde{H}'$ matrix

$$\tilde{H} = \begin{bmatrix} \tilde{H}' \\ \dfrac{\partial r_\circ}{\partial \mathbf{X}} \end{bmatrix}, \tag{A.23}$$

we write the partial derivatives

$$\frac{\partial r_\circ}{\partial \mathbf{r}_i} = \begin{bmatrix} \dfrac{\partial r_\circ}{\partial x_i} & \dfrac{\partial r_\circ}{\partial y_i} & \dfrac{\partial r_\circ}{\partial z_i} \end{bmatrix}, \tag{A.24}$$

where

$$\frac{\partial r_\circ}{\partial x_i} = \frac{x_\circ \eta_i}{r_\circ M} \tag{A.25}$$

$$\frac{\partial r_\circ}{\partial y_i} = \frac{y_\circ \eta_i}{r_\circ M} \tag{A.26}$$

$$\frac{\partial r_\circ}{\partial z_i} = \frac{z_\circ \eta_i}{r_\circ M}. \tag{A.27}$$

A.2   Solution

We estimate $\mathbf{X}$ using the least squares algorithm described in Chapter 3. We note that, since the positions of the point masses are constant in the planet fixed frame, $\Phi(t_i, t_\circ) = \mathbb{I}$; thus, $H = \tilde{H}$. We set the observation variance-covariance matrix

$$R = \begin{bmatrix} P_{\bar{C}S} & 0 \\ 0 & \sigma_{r_\circ}^2 \end{bmatrix} \tag{A.28}$$

where $P_{\bar{C}S}$ is a diagonal matrix of the variances associated with the GGM02C model, and $\sigma_{r_\circ} = 10^5$ km. We initially place 25 larger masses near the center of the coordinate system, and distribute 25 smaller masses randomly on the surface of the Earth. We then solve for the position of the 50 point masses and approximate the GGM02C model to degree 7. Estimation of any higher degree terms fails to converge on a solution for this implementation.

We illustrate the resulting spherical harmonics coefficients in Figure A.1, with differences between the point-mass solution and the GGM02C values provided in Figure A.2. The values of the points masses may be found in Tables A.1 and A.2.
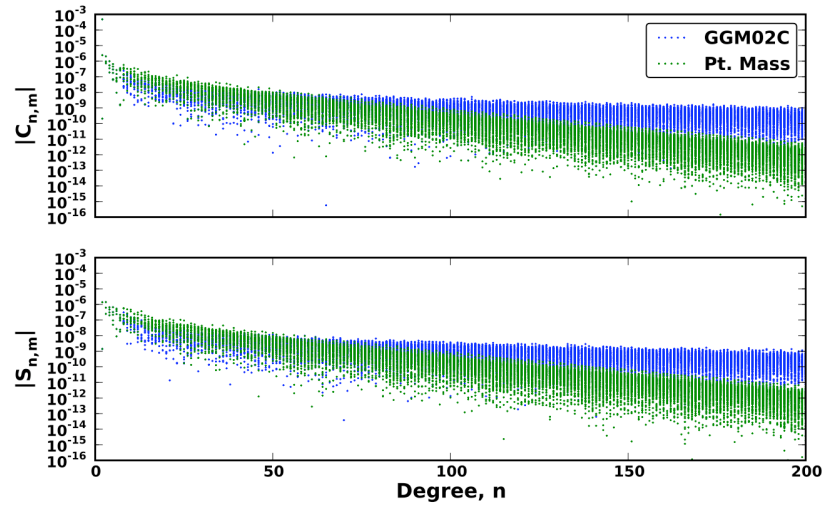
Figure A.1: Absolute values of the GGM02C and point-mass model determined spherical-harmonic-model coefficients.
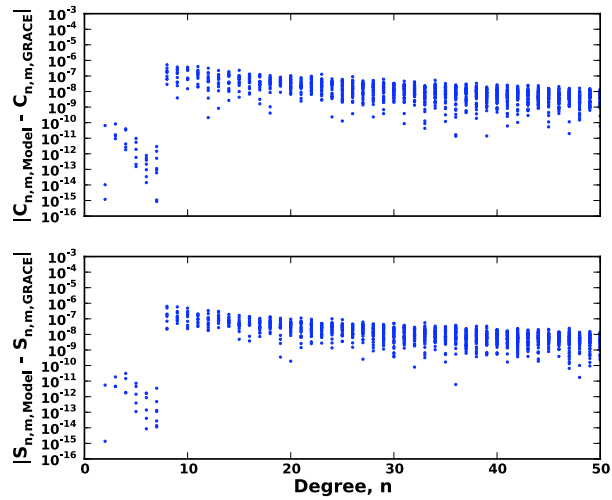

Figure A.2: Difference between the Stokes coefficients determined using a collection of masses and the GGM02C model.

Table A.1: 25 of 50 point masses used to define the reference model for characterizing the spherical harmonics formulations, which was designed with $GM = \mu = 398600.4415$ km^3/s^2.

Mass	Radius (km)	Latitude (deg)	Longitude (deg)
.039996	1153.92372750503	6.43173112711670	-18.1550206202232
.039996	860.720628046090	-41.2092043927566	-31.7268065330912
.039996	1013.56725204395	-29.9234575672558	72.0926838647558
.039996	811.062605873362	-54.8466224074458	-58.1857803960244
.039996	672.530541847089	7.13897532117478	153.347910434484
.039996	850.198325569758	61.1067412779413	141.502833973025
.039996	675.546074058148	-46.3622171176600	125.168971691340
.039996	801.873833806594	45.7570854020121	-112.391271168268
.039996	433.731110872869	10.6933343621237	-165.718659103055
.039996	1093.14438016795	3.61883605011266	-71.9140091101436
.039996	306.855252301518	-24.8604823451530	-161.095029397592
.039996	997.139177386362	53.8777439277858	-32.9197960330570
.039996	315.817633075392	-12.6067491584611	-153.539643434976
.039996	490.246943437380	-7.92374784384371	140.556366586796
.039996	629.960761637284	-6.64664992096353	132.887431456942
.039996	316.344017381063	-12.4577513153309	-144.584093912332
.039996	430.759718998166	-46.6960283495022	144.040417410937
.039996	1121.21313537526	15.1011043375355	36.6857600726105
.039996	875.667619580378	55.5683985563732	33.8939278219740
.039996	680.927238345851	14.7188887646595	-128.259875649750
.039996	540.808278127778	22.5585202559987	-155.530935124254
.039996	1020.69903885308	-30.6470489444354	20.2568448788601
.039996	1034.27477603497	20.2354013005163	91.4886280869801
.039996	515.946764430866	-56.9455200666397	-154.156034494238
.039996	740.792997846867	-27.4907867963254	-117.747669891304

Table A.2: 25 of 50 point masses used to define the reference model for characterizing the spherical harmonics formulations, which was designed with $GM = \mu = 398600.4415$ km^3/s^2.

Mass (units of M)	Radius (km)	Latitude (deg)	Longitude (deg)
4×10^{-6}	5828.78809276127	5.82218716513003	147.414584023154
4×10^{-6}	4387.05609962843	-71.0540639180324	86.4012102435706
4×10^{-6}	5309.27543794979	40.3926537386017	-39.8315906510258
4×10^{-6}	4572.54589559061	35.9855986958989	145.267050355714
4×10^{-6}	4726.93906337121	-59.3193607308720	-149.852565370887
4×10^{-6}	6098.60553490051	3.24531118581967	117.411722064867
4×10^{-6}	5362.15538685248	36.7402507705754	-79.4424363488290
4×10^{-6}	5133.31699750134	4.09768321837324	-165.004484079539
4×10^{-6}	4139.95853535821	30.0058272105687	-111.220538347931
4×10^{-6}	4722.93716655481	39.9414193847231	-33.4029118176349
4×10^{-6}	5220.40417759491	-74.6164823047343	128.433756598078
4×10^{-6}	5289.36463390104	-68.9492496448170	75.1260031000578
4×10^{-6}	4348.69876521043	-68.7010675321301	43.7259673114938
4×10^{-6}	4652.28118512938	-5.78673650687255	-53.7472768813786
4×10^{-6}	3677.80870225334	45.1159304045092	100.447317621847
4×10^{-6}	4111.84902706709	74.7972999900462	7.17705076195400
4×10^{-6}	4412.99506732648	26.0766658123727	-92.3039682830442
4×10^{-6}	3940.83197004955	38.7143633398815	-35.1244256768768
4×10^{-6}	5057.67609428604	-83.8335056459668	-21.2571989800688
4×10^{-6}	5437.83872303049	40.0024983599406	135.099606483756
4×10^{-6}	4204.84101297012	45.3430000180872	27.6946840376581
4×10^{-6}	5100.47275493532	-8.96277899110691	-127.328068420352
4×10^{-6}	4096.88520241790	30.6696084032430	-99.2175830376057
4×10^{-6}	3872.69140166276	-20.0285253948458	-124.856591228904
4×10^{-6}	4545.90423574725	32.0918203654867	171.781131737086